2013

Impact of IUdR in rat 9L glioma cell survival for 25-35 keV photo-activated Auger electron therapy

Diane Alvarez
Louisiana State University and Agricultural and Mechanical College

IMPACT OF IUDR IN RAT 9L GLIOMA CELL SURVIVAL FOR 25-35 KEV PHOTO-ACTIVATED AUGER ELECTRON THERAPY

A Thesis

Submitted to the Graduate Faculty of the
Louisiana State University and
Agricultural and Mechanical College
in partial fulfillment of the
requirements for the Degree of
Master of Science

in

The Department of Physics and Astronomy

By
Diane Alvarez
B.S. Physics, Florida International University, 2007
December 2013

ACKNOWLEDGMENT

My sincerest gratitude goes to Dr. Kenneth Hogstrom for supervising this project, as well as my four other committee members, Drs. Kip Matthews, Joseph Dugas, Marie Varnes, and Richard Kurtz for their insight into the course of my thesis.

This project would not have been possible without the availability of a wide array of equipment and staff from multiple institutions. As such, I thank members of the CAMD staff, especially Dr. Kyungmin Ham for the general assistance with the radiobiological beamline and beam-time scheduling. I thank David Perrin, Dr. Monica Moldovan, and Connel Chu of Mary Bird Perkins Cancer Center for help with megavoltage cell irradiations. Cell laboratory facilities were provided by LSU Pennington Biomedical Research Facility. I am particularly grateful to Dr. Thomas Brown with whom I worked and whom provided daily supervision to me.

I thank Yvonne Thomas and Arnell Nelson of the LSU Physics Department and Susan Hammond of Mary Bird Perkins Cancer Center for their assistance in the administrative aspects of my graduate studies.

Finally, I thank mom and dad, and my boyfriend Daniel, for their love and support throughout this endeavor. Without their unwavering belief in me, I would have not had the strength to endure the endless trials and tribulations I have encountered along the way.

I acknowledge funding support for this project, including my National Science Foundation Graduate Research Fellowship Program (NSF GRFP). This project was also supported in part by Contract No. W81XWH-10-1-0005 awarded by the U.S. Army Research Acquisition Activity. This paper does not necessarily reflect the position or policy of the Government, and no official endorsement should be inferred.

Words cannot describe my deep gratitude. Thank you all from the bottom of my heart!

TABLE OF CONTENTS

LIST OF TABLES

LIST OF FIGURES

ABSTRACT

Introduction: Photo-activated Auger electron therapy is a potential technique that could preferentially target cancer cells. This binary therapy uses a drug containing a high-Z element like iododeoxyuridine (IUdR), which serves as a radiosensitizer and molecular carrier of high-Z iodine into cancer cell DNA. Iodine becomes the Auger electron source when activated by photons with an appropriate energy. This work studied the survival of rat 9L glioma cells with IUdR replacing thymidine in the DNA. Irradiations at monochromatic energies above and below the iodine K-edge (33.2 keV) are part of a larger study from 25-70 keV. It was hypothesized that SER_{10} values for 9% and 18% IUdR-laden 9L glioma cells irradiated by 25-35 keV photons would be greatest at 35 keV due to the Auger effect.

Methods: Rat 9L glioma cells survival versus dose curves with 0%, 9%, and 18% IUdR were measured using four irradiation energies (4 MV x-rays; 35, 30, and 25 keV synchrotron photons). For each of 11 conditions (Energy, %IUdR) survival curves were fit to the data (826 cell cultures) using the linear quadratic model. The ratio of doses resulting in 10% survival gave sensitization enhancement ratios (SER_{10}) from which contributions due to linear-energy transfer (LET), radiosensitization (RS), and Auger effect (AE) were determined.

Results: At 35, 30, and 25 keV, $SER_{10,LET}$ values were 1.08±0.03, 1.22±0.02, and 1.37±0.02, respectively. At 4 MV $SER_{10,RS}$ values for 9% and 18% IUdR were 1.28±0.02 and 1.40±0.02, respectively. Assuming LET effects are independent of %IUdR and radiosensitization effects are independent of energy, $SER_{10,AE}$ values for 18% IUdR at 35, 30, and 25 keV were 1.35±0.05, 1.06±0.03, and 0.98±0.03, respectively; values for 9% IUdR at 35 and 25 keV were 1.01±0.04 and 0.82±0.02, respectively. Contrastingly, a different, more traditional analysis gave $SER_{10,AE}$ values of 1.27±0.06 and 1.25±0.06 at 35 keV for 18% and 9% IUdR, respectively.

Conclusions: Results of this research proved the hypothesis correct; at 35 keV $SER_{10,AE}$ was significantly greater than values at 25 and 30 keV for 18% IUdR and at 25 keV for 9% IUdR. Additional data and radiobiological modeling is required to better explain these results.

CHAPTER 1: INTRODUCTION

The goal of this project is to elucidate some aspects of photo-activated Auger electron therapy, a potential new therapy technique that could preferentially target cancer cells. This is a binary therapy that uses a drug containing a high atomic number (Z) element, like iodine in iododeoxyuridine (IUdR), for two purposes: (1) as a radiosensitizer and (2) as a molecular carrier of a high-Z atom into the DNA of cancer cells. The latter becomes the source of Auger electrons when activated by monochromatic photons with an appropriate energy. The current thesis describes the survival of rat 9L glioma cells with IUdR incorporated into the DNA (0%, 9%, and 18% IUdR) irradiated at energies above (35 keV) and below (25, 30 keV) the iodine K-edge. This project is part of a larger study intended to span the energy range of 25-70 keV.

1.1 Current State of the Art in Radiotherapy

In current radiotherapy practice, dose is prescribed and delivered to a specified volume of tissue called the planning treatment volume (PTV), which includes a mixture of healthy and cancerous tissue. The PTV can be accurately irradiated while avoiding nearby normal tissues and critical structures by using modern radiation therapy technology such as (1) intensity modulated radiotherapy (IMRT), (2) proton and heavy ion therapy, (3) image guided radiotherapy (IGRT), (4) motion management (e.g. respiratory gated radiotherapy), and (5) adaptive radiotherapy (Zelefsky *et al.* 2000, Jensen *et al.* 2011, Verellen *et al.* 2007, Keall *et al.* 2002, Keall *et al.* 2001). To further improve today's radiotherapy technology and paradigm, healthy tissue inside (and outside) the PTV could be further spared by targeting cancer at the cellular level. One potential method for targeting cancer at the cellular level is photo-activated Auger electron therapy, a form of chemo-irradiation (combining radiation therapy with drugs that preferentially target cancer cells).

1.2 Photo-Activated Auger Electron Therapy

The basis of photo-activated Auger electron therapy utilizes a monochromatic photon (i.e., x-ray) with an energy (E_γ) slightly greater than the binding energy (E_K) of the K-edge electrons of a high-Z atom that is part of the drug attached to the DNA. When a photon interacts via the photoelectric effect, a K-shell electron is ejected. Subsequently, orbital electrons cascade to fill the vacancy emitting fluorescence photons and Auger electrons (see Figure 1.1). Note that fluorescence photons and Auger electrons are competing processes.

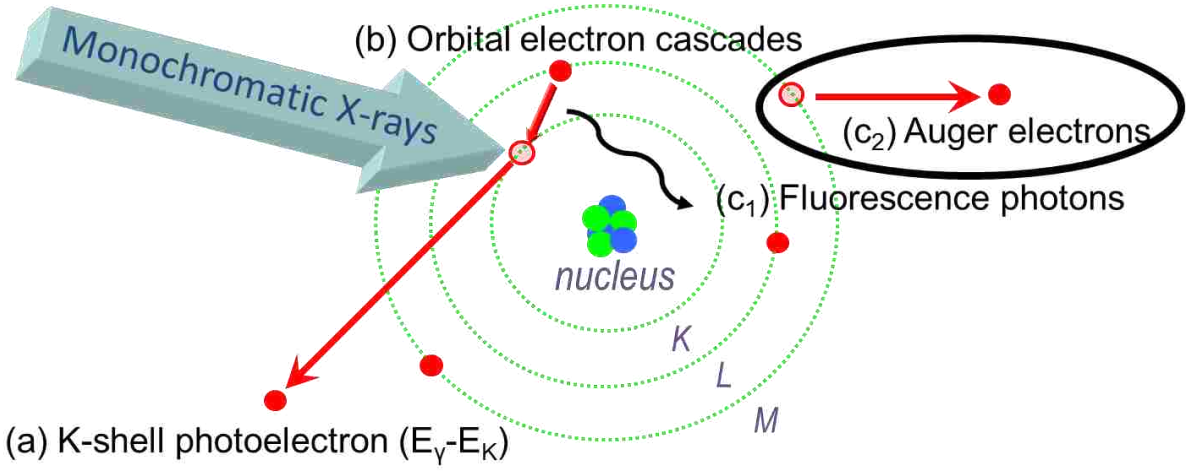

Figure 1.1: Illustration of the Auger effect. A monochromatic photon with $E_\gamma > E_K$ of the atom interacts via the photoelectric effect, ejecting a K-shell electron (a). Orbital electrons cascade (b) to fill the vacancy emitting fluorescence photons (c_1) or Auger electrons (c_2).

Auger electrons, which have a range of approximately 1-400 nm in water (Kassis 2004, Kereiakes *et al.* 1993), deposit a tremendous amount of dose to the surrounding local areas. This is illustrated in Figure 1.2(a), where Kassis & Adelstein (2005) used Monte Carlo to simulate the emission of Auger electrons from ^{125}I decay inside a double-helix DNA. Represented by the lines, the Auger electron tracks create multiple nearby ionizations, represented by the "stars." The density of these ionizations is much like that from high-LET α particles, which have a high probability for double strand breaks (DSBs) that are difficult to repair (Kassis & Adelstein

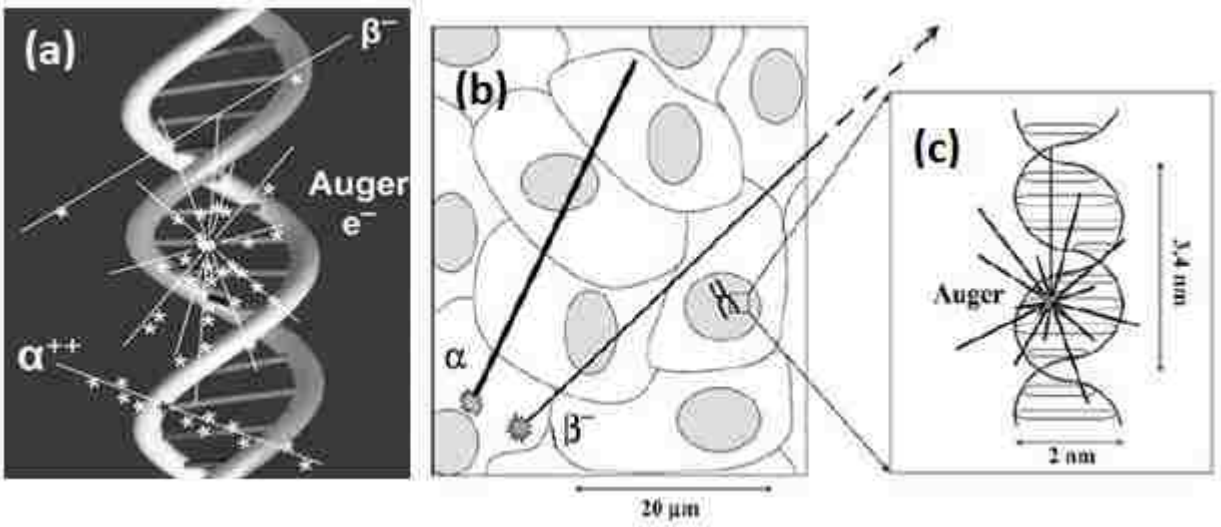

Figure 1.2: Simplified illustrations of α, β^-, and Auger electron radiation deposition. (a) Ionization events (represented by "stars") in double-stranded DNA by α, β^-, and Auger electron radiation. Lines represent particle tracks (Kassis & Adelstein 2005). (b) The range of α and β^- radiation in cellular environment. (c) The range of Auger electrons in subcellular environment. Note that the major energy deposition of Auger electrons occurs in the close vicinity of a few nm, while that of α and β^- radiation occur on tracks of 40-80 μm and 0.1-10 mm, respectively (Buchegger *et al.* 2006).

2005). Figure 1.2(b) and (c) are schematic presentations of α, β^-, and Auger radiation path lengths in a cellular and subcellular environment using arbitrary scaling (Buchegger *et al*. 2006). Note that in Figure 1.2(b) the major energy deposition of α and β^- radiation occur on tracks of 40-80 μm and 0.1-10 mm, respectively, while that of Auger electrons (see Figure 1.2(c)) occur in the close vicinity of a few nanometers (Buchegger *et al*. 2006).

The scenario depicted in Figure 1.2(a) (caused by radioisotope ^{125}I) can also be activated by many other Auger emitters. Radioisotopes of clinical interest are ^{125}I, ^{123}I and ^{201}Tl (Buchegger *et al*. 2006). However, the use of radioisotopes for the purpose of triggering Auger electrons is outside the scope of this project. Auger electrons can also be triggered by an external x-ray beam via photo-activation, interacting with a high-Z atom located in DNA. If a sufficient number of high-Z atoms can be incorporated into the DNA of a cancer cell, they can create enough Auger events that the damage to the cell due to Auger electrons would be significant.

The number of Auger events depends on the high-Z atom, the number of these atoms incorporated into the DNA (discussed in Section 1.3.3.1), and the cross section (σ) for the photoelectric interaction. Cross section is related to the mass attenuation coefficient $\left(\frac{\mu}{\rho}\right)$, by $\frac{\mu}{\rho} = \frac{\sigma}{A} * N_A$ (cm^2*g^{-1}), where σ is the cross section (or probability) per unit path length of photon interaction, A is the atomic mass of the material, and N_A is Avogadro's number. The cross section depends strongly on the Z of the atoms of the absorbing medium and varies strongly with photon energy E_γ.

1.3 Requirements for High-Z Materials in Photo-Activated Auger Electron Therapy

In order for photo-activated Auger electron therapy to be clinically feasible, the high-Z material (i.e., drug) must meet four conditions:

1. It must be close to, attached to, or intercalated with the DNA of the cell;
2. It should have preferential uptake by cancer cells and in sufficient quantities to elicit a therapeutic gain;
3. The high-Z component of the drug should be equal to or greater than that of iodine ($Z \geq 53$) to allow sufficient penetration in tissue by photons with $E_\gamma > E_K$; and
4. Dose should be delivered using the optimal monochromatic x-ray beam energy to cause as many Auger events as possible.

1.3.1 Cellular Location of IUdR

The combining size (i.e., the van der Waals radius) of an atom of iodine is very similar to that of a methyl group CH_3 (215 pm versus 200 pm, respectively) (Prusoff *et al.* 1979). The halogenated pyrimidine IUdR is a drug that is consequently very similar to the normal DNA precursor thymidine, having a halogen substituted in place of the methyl group (Hall & Giaccia

2006). Since IUdR mimics the van der Waals radius of thymidine, it incorporates into DNA during its synthesis (see Figure 1.3). This substitution "weakens" or destabilizes the DNA in the cell, making it more susceptible to damage by x-rays (Iliakis & Kurtzman 1989, Hall & Giaccia 2006), and decreasing the reparability of double strand breaks (Wang & Iliakis 1992).

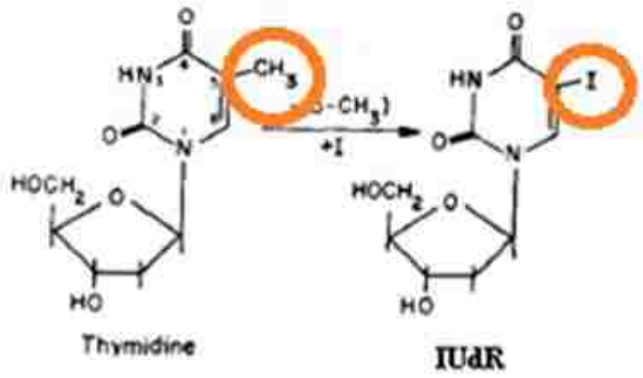

Figure 1.3: Comparison of molecular structure of IUdR and thymidine. The circled CH_3 of thymidine (left) is replaced by I forming the IUdR (right). Otherwise, the two molecules are the same (Prusoff *et al.* 1979).

1.3.2 Selectivity & Quantity of IUdR Uptake

IUdR will incorporate preferentially in cells that are proliferating more quickly and thus may be expected to sensitize rapidly-growing tumors rather than slowly proliferating normal tissue (Karnas *et al.* 1999). Some examples of rapidly-growing cancer cells are glioblastoma multiforme (which arise from astrocytes) and lymphoma (which arise from lymphocytes). Mature human brain astrocytes are generally accepted as non-proliferating (Guizzetti *et al.* 2011). In contrast, glioblastoma multiforme cells have a doubling time of about 43 hours (Coleman *et al.* 1980). In the case of normal B-cell lymphocytes, they have an estimated cell doubling time of 14-21 days, whereas high-grade lymphoma has an estimated doubling time of 2-3 days (Hong *et al.* 2009).

The quantity of IUdR uptake by the DNA of a cell (thymidine replacement or %IUdR) varies with the concentration of IUdR, the amount of time IUdR is exposed to the cells, and the type of cells. Since IUdR is taken up by cells only during the S-phase of the cell cycle, IUdR must be made available to cells for more than one cell generation (at minimum 1 to 2 population doubling times, where 1 doubling time = 1 generation) so that an appreciable quantity of the analog may be incorporated into the DNA (Kinsella 1996, Hall & Giaccia 2006). Furthermore, since IUdR is rapidly metabolized in both rodent and human cells, continuous exposure, such as a prolonged continuous intravenous (c.i.v.) or intra-arterial infusion, is necessary to maximize the proportion of tumor cells that incorporate IUdR during S-phase (McGinn & Kinsella 1993).

The amount of IUdR uptake can be considerable for certain cell lines *in vitro* before it becomes toxic to the cells (39% thymidine replacement in Chinese hamster lung cells after 24 hr. incubation period (Nath *et al.* 1987); 24% for human D98/AG cells exposed for 5 days (Erikson & Szybalski 1963); and 30% for human colon carcinoma cells (HT29) after 4 days of exposure (Lawrence *et al.* 1990)). *In vivo*, however, IUdR uptake has been considerably less in humans, e.g., a maximum of 4.9% after 28 days of c.i.v. infusion (Schulz *et al.* 2004). The patients that achieved 4.9% IUdR (IUdR dose = 781 $mg*m^{-2}*d^{-1}$, the highest IUdR dosage in the study), however, experienced the most significant toxicities of all patients in this trial. This led the authors to report that the maximal tolerated dose (MTD) was 625 $mg*m^{-2}*d^{-1}$, which only achieved 3% IUdR *in vivo.*

Progress has been made in decreasing the toxicity to *in vivo* normal tissues by improving the drug's pharmacokinetics. An oral prodrug of IUdR, 5-iodo-2-pyrimidinone-2'-deoxyribose (IPdR), efficiently converts to IUdR by the liver enzyme aldehyde oxidase (Chang *et al.* 1992). Other normal tissues, including intestine, bone marrow, lung and kidney, show > 10-fold less

activity of IPdR aldehyde oxidase (Chang *et al.* 1992). This study resulted in extensive pre-clinical testing where oral administration of IPdR has been shown to improve the therapeutic index (i.e., lessen toxicity) when compared with c.i.v. IUdR using several different human tumor xenograft models (Kinsella *et al.* 1994, Kinsella *et al.* 1998, Kinsella *et al.* 2000a, Seo *et al.* 2004, Seo *et al.* 2005). In addition, systemic toxicology and pharmacokinetics studies on rodent and non-rodent animals demonstrated that the MTD of oral IPdR is considerably greater than the MTD of IUdR, with little to no significant toxicity (Kinsella *et al.* 1994, Kinsella *et al.* 2000a, Kinsella *et al.* 2000b, Kinsella *et al.* 2008). The first in-human phase 0 trial of IPdR in patients with various advanced malignancies resulted in no drug-related adverse events (Kummar *et al.* 2013).

1.3.3 Optimal Monochromatic Energy & High-Z Atom for Production of Auger Events

1.3.3.1 K-Edge Energy of Iodine & the Production of Photoelectric Events

As mentioned in Section 1.2, the high Z-atom, the number of these atoms incorporated into the DNA, and the cross section (σ) for the photoelectric interaction of the high-Z atom dictates the possible number of Auger events that can occur. Figure 1.4 plots the photoelectric mass attenuation coefficients for iodine as a function of photon energy. The sharp rise in $\frac{\mu}{\rho}$ at 33.2 keV (E_K, the binding energy for the iodine K-shell) is due to the photoelectric contribution of the innermost, K-shell electrons. Below this energy, these electrons do not contribute to photoelectric absorption because there is insufficient energy to eject them from the atom. The discontinuity in the energy dependence of $\frac{\mu}{\rho}$ is known as the K-edge; its energy is approximately proportional to Z^2. At lower photon energies, the photoelectric absorption edge due to L-edge electrons with lower binding energies (see Figure 1.4) are evident (Lilley 2001).

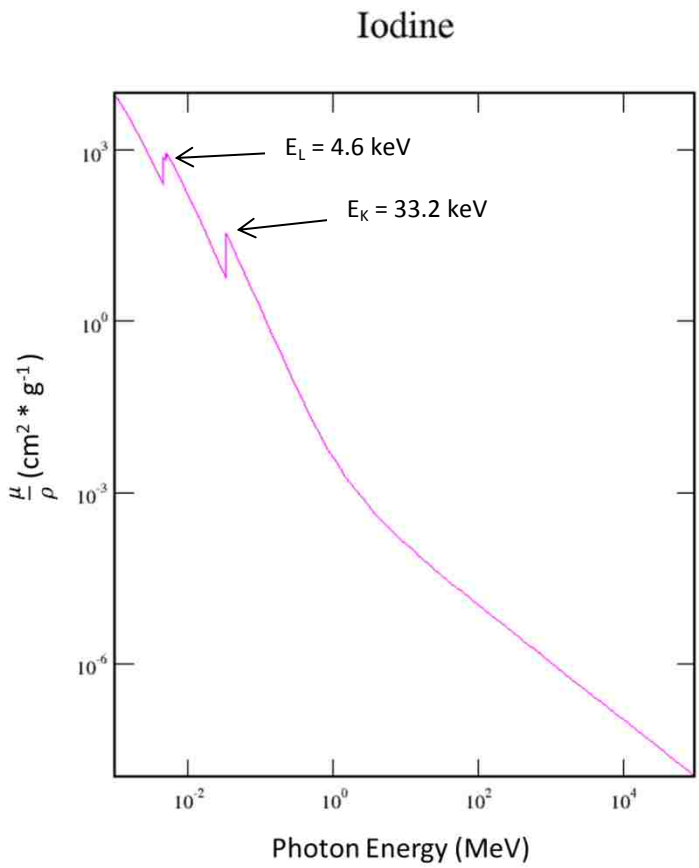

Figure 1.4: Plot of photoelectric mass attenuation coefficients (μ/ρ) for iodine (Z=53) versus photon energy for narrow beam geometry. The L- and K-edge energies are indicated (Hubbell & Seltzer 2004).

In regards to clinical applications, the half-value layer (HVL) in tissue of the activating photon beam is of therapeutic consequence, as low values might impede access to cancer cells at depth (Fairchild *et al.* 1982). For Z = 53-79 (iodine to gold), K-shell energies range from E_K = 33.2-80.7 keV (Kaye & Laby 1995), which result in HVL in water (approximately tissue) values (HVL_{water}) of ≈ 3.4-6.3 cm (note that HVL_{water} ≈ 3.6 cm for 35 keV) for broad beam geometry (NCRP 2005) and 2.1-3.8 cm for narrow beam geometry (Hubbell & Seltzer 2004). In the case of L-edge electrons, energies are so low for Z = 53-79 (E_L = 4.6-11.9 keV (Kaye & Laby 1995) result in HVL_{water} ≈ 0.77-1.4 cm for broad beam geometry (NCRP 2005) and 0.013-0.23 cm for

narrow beam geometry (Hubbell & Seltzer 2004)) that the activating photon cannot penetrate to any useful depth in the body.

Corde *et al.* (2004) argued that an irradiation energy of 50 keV would achieve the maximum therapeutic effect of IUdR. They used the concept of "dose enhancement ratio" (DER), defined as the ratio of the mass energy-absorption coefficient of water in the presence of iodine to that in the absence of iodine, i.e.,:

$$DER\ (E) = \frac{\left(\frac{\mu_{en}}{\rho}\right)_E^{water+iodine}}{\left(\frac{\mu_{en}}{\rho}\right)_E^{water}} = \frac{w_I * \left(\frac{\mu_{en}}{\rho}\right)_E^{iodine} + (1 - w_I) * \left(\frac{\mu_{en}}{\rho}\right)_E^{water}}{\left(\frac{\mu_{en}}{\rho}\right)_E^{water}}. \quad (1.1)$$

where $\left(\frac{\mu_{en}}{\rho}\right)_E$ is the mass energy absorption coefficient for water, iodine, and a mixture of water and iodine irradiated with monochromatic x-ray beam energy, E, and w_I is the fraction by weight of iodine in the mixture. Figure 1.5 illustrates the energy dependence of the theoretical DER of aqueous iodine as a curve having its maximum around 50 keV. The range of energies yielding

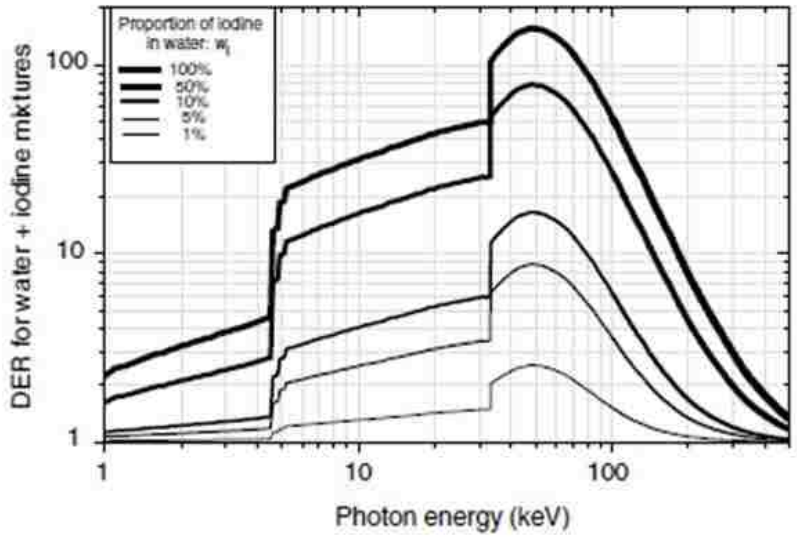

Figure 1.5: Energy dependence of the theoretical DER for several iodine aqueous mixtures. From bottom to top, the mass proportion of iodine in water, w_I, ranges from 0.01 to 1 (Corde *et al.* 2004).

such a sharp variation is relatively narrow, from the K-edge of iodine (33.2 keV) up to about 80 keV.

1.3.3.2 Toxicity of High-Z Drugs Containing Platinum versus Iodine

The toxicity of the high-Z drug chosen for a study of this nature limits the amount of the drug that can be incorporated into the cells, thus, influencing the number of Auger events possible. Corde *et al.* (2002) studied the incorporation of cis-diamminedichloroplatinum molecules (CDDP) into cells. CDDP, a platinum-containing compound, is a DNA alkylating-like molecule (Reed 1992) that, once inside cells, becomes intracellularly activated via the aquation process (i.e., a chloride group is displaced by water). CDDP covalently bonds to DNA, preferentially binding to guanine-rich portions of DNA (Reed 1992), and forms DNA adducts that causes cytotoxicity by way of apoptosis (Ferri *et al.* 2013). Figure 1.6 summarizes Corde's *et al.* (2002) findings, which illustrates the survival curves for SQ20B cells exposed to 1 μM CDDP for 12 hours prior to being irradiated with photon energies above (78.8 keV; closed triangle) or below (78.0 keV; open triangle) the K-shell absorption edge of platinum (78.4 keV). Control cells (closed circles) were incubated in platinum-free medium. No difference was found in the survival fraction versus dose when the cells were irradiated with beams above and below the platinum K-edge, as shown in Figure 1.6. However, the higher cell death resulting from drug toxicity limited the uptake (e.g., 1 μM CDDP exposure for 12 hours resulted in 17% cell survival (83% cell killing) as shown in Table 1.1).

Conversely, Figure 1.7 demonstrates the radiobiological response of V79 cells containing 16% IUdR irradiated with photons just below (32.9 keV; diamonds) or above (33.4 keV; triangles) the K-edge of IUdR (Laster *et al.* 1993). It is evident that there is enhanced cell killing

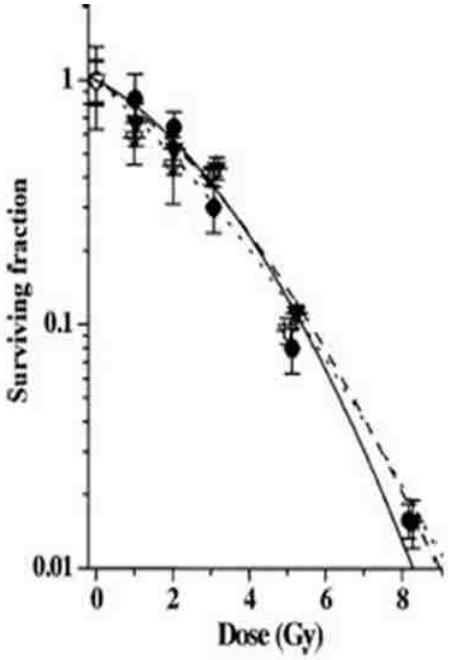

Figure 1.6: Survival curves for SQ20B cells with CDDP. Cells were exposed to 1 μM CDDP for 12 h and irradiated above (closed triangle) or below (open triangle) the K-shell absorption edge of platinum (78.4 keV). Control cells (closed circles) were incubated in platinum-free medium (Corde *et al.* 2002).

Table 1.1: Correlation between the toxicity of several CDDP exposures to SQ20B cells and the intracellular platinum content (Corde *et al.* 2002).

CDDP exposure	Survival (%)	Platinum content (atoms/cells)
0.1 μM for 48 h	66	7.0×10^4
3 μM for 6 h	25	4.0×10^6
1 μM for 12 h	17	4.5×10^6
10 μM for 6 h	0.8	7.5×10^6
3 μM for 12 h	0.4	9.0×10^6

at both 32.9 keV and 33.4 keV for cells containing 16% IUdR. Unlike CDDP-loaded cells, which suffered a decrease in cell survival from 100% for control cells to 17% for cells treated with 1

μM due to drug toxicity (Corde *et al.* 2002), Laster *et al.* (1993) reported a cell survival of 69% ± 8% for 6 μM IUdR-treated cells (corresponding to 16% IUdR) before cell irradiations.

The difference in the survival of cells containing either CDDP or IUdR can be explained simply by the fact that insufficient CDDP was incorporated into the DNA of cells before toxicity occurred to elicit a therapeutic gain in cell death due to the Auger effect. Despite Corde and colleagues (2002) confirming the nuclear localization of platinum, higher levels (> 1 μM) of platinum atoms in the DNA were strongly limited by the toxicity of the CDDP. Consequently, higher intranuclear platinum contents could not be achieved under their experimental conditions.

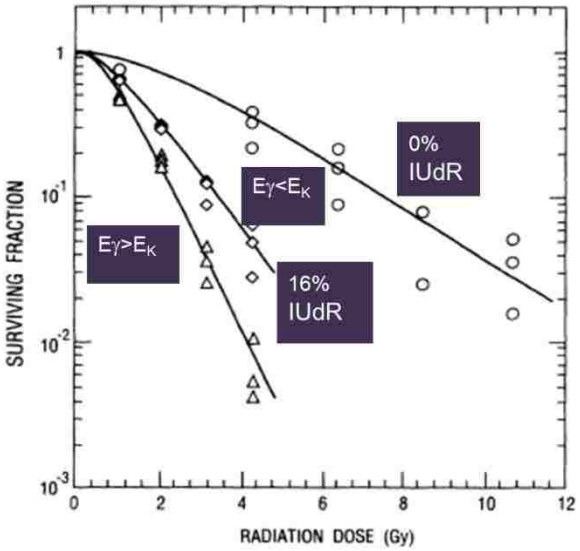

Figure 1.7: Irradiated Chinese hamster V79 cells with and without IUdR (16.3% thymidine replacement). Cells were irradiated with energies just above (33.4 keV; triangles; D_{10} = 2.7 Gy) and below (32.9 keV; diamonds; D_{10} = 3.4 Gy) the iodine K-edge to see if any additional biological damage would accrue from Auger events. Circles represent control cells (D_{10} = 7.5 Gy). A therapeutic gain of about 3 was achieved for cells irradiated above the K-edge, i.e., including both sensitization and the Auger effect (Laster *et al*. 1993).

Despite Corde's *et al*. (2002) findings, Rosseau *et al.* (2007) further investigated platinum-containing drugs by using carboplatin in the treatment of tumors. Not surprisingly, the average survival time of glioma-bearing rats following intracerebral delivery of carboplatin and photon irradiations was the same as photon irradiation alone, i.e., there was no therapeutic gain from photo-activation evident.

1.3.3.3 Number of Auger Events in DNA per Dose in Water

The high-Z drug chosen for a study of this nature, the amount incorporated into the DNA, and the irradiating photon energy determine the average number of photoelectric events per cell nucleus per dose in water. A theoretical estimate (based on the photoelectric cross section) of the number of photoelectric events per cell per 2 Gy dose for cells containing 1 μM CDDP (83% toxicity) is 0.1 (Corde *et al.* 2002) as opposed to 13.0 for cells containing 20% IUdR (30% toxicity; see Table 1.2). The derivation of this estimate can be found in Appendix A.

Similar theoretical calculations by Humm and Charlton (1989) for IUdR showed the number of K-shell photoelectric events in iodine atoms per 2 Gy dose in the DNA of a single cell assuming a 20% IUdR substitution in DNA (see Table 1.3). They calculated 11.8 and 5.2 photoelectric events per 2 Gy for 33.2 keV and 60 keV, respectively.

Table 1.2: The number of Auger events per 2 Gy dose to water. Cells contained either CDDP (4.5×10^6 atoms/cell) or IUdR (6.0×10^8 atoms/cell; 20% thymidine replacement) in the DNA. Note that only K-edge interactions were considered.

Drug & Quantity	High-Z Atom	Eγ (keV)	σ_{PE} (barns)	# Atoms per cell in DNA	Toxicity (%)	# Auger events per cell per 2 Gy dose to water
1 μM CDDP	Platinum	78.4	2,909	4.5×10^6	83	0.1
3μM IUdR	Iodine	33.2	7,374	6.0×10^8	30	13

Table 1.3: The number of photoelectric interactions in iodine per 2 Gy for different photon energies with 20% IUdR incorporation into the DNA (Humm & Charlton 1989).

Photon Energy	Photons/ $cm^2 * Gy$	Cross Section $cm^2/atom$	# Auger events per 2 Gy
33.2 keV	1.49×10^{12}	7.41×10^{-21}	11.8
60 keV	3.30×10^{12}	1.51×10^{-21}	5.2
1 MeV	2.02×10^{11}	8.62×10^{-25}	1.84×10^{-4}

According to theoretical calculations by Karnas *et al.* (2001), photoelectric event predictions are higher at these energies when interactions from all orbital shells (K-, L-, M-,..) are considered. According to their results, there would be 20.76 and 8.92 photoelectric events (67.6% from K-shell, 21.1% from L-shell, and 11.3% from M-, N-, and O-shell interactions), in iodine atoms per 2 Gy dose for cells containing 20% IUdR irradiated at 33.2 and 60 keV, respectively (see Table 1.4). The number of photoelectric interactions within iodine is largest at the K-edge energy of iodine.

1.3.3.4 Number of DSBs in DNA per Dose in Water

Of the number of photoelectric interactions (Auger events) possible, a proportion produces DSBs in the DNA of the cell. There is an estimated occurrence of 60-72 DSBs per 2 Gy delivered to water for cells with no IUdR (Karnas *et al.* 2001, Heilmann *et al.* 1995, Humm & Charlton 1989). An additional amount of DSBs would occur if the cells were IUdR-loaded. Karnas *et al.* (2001) predicted and experimentally measured the number of DSBs formed per Gy for cells containing 20% IUdR. Through Monte Carlo techniques, of the estimated 11.82 photoelectric events per 2 Gy that can occur for IUdR-laden cells irradiated with tungsten-filtered 100 kVp x-rays, 3.30 DSBs were predicted to occur (see Table 1.4). By comparison, they

Table 1.4: The production of electron orbital vacancies from photoelectric events in iodine. Assuming a 20% IUdR substitution in DNA, the corresponding calculated DSB production from Auger events as a function of energy are also listed (Karnas *et al.* 2001).

Energy (keV)	# of photoelectric events in any shell of iodine per 2 Gy	Predicted # of DSBs formed per 2 Gy
10	7.64	1.76
20	5.16	1.18
30	3.90	0.90
33.2	20.76	5.82
40	18.32	5.12
50	13.30	3.72
60	8.92	2.50
80	3.70	1.04
30 kVp	7.48	1.72
100 kVp	7.34	1.94
W-filtered 100 kVp	11.82	3.30

found that 7.2 ± 3.2 DSBs per 2 Gy occurred when measured using comet assays. They attribute the higher measured levels of DSBs to be a result of DNA damage from Auger electrons spanning across giant loop structures of DNA, something that the Monte Carlo simulation did not account for. Because these theoretical calculations are based on macro-dosimetry, Karnas and colleagues believe that DSBs from Auger events may be more complex due to the unaccounted micro-dosimetry.

Both the number of photoelectric events and number of DSBs at 33.2 keV are approximately double of that at 100 kVp (tungsten-filtered). The largest number of photoelectric events predicted by Karnas *et al.* (2001) was 20.76 per 2 Gy at 33.2 keV, of which 5.82 were predicted to form DSBs.

1.4 Suitability of IUdR in Photo-Activated Auger Electron Therapy

IUdR has been recognized as a radiosensitizer (using ionizing radiation) to mammalian cells since the 1960's (Djordjevic & Szybalski 1960, Miller *et al.* 1987, Kinsella 2008). The mechanism for radiosensitivity by IUdR is believed to be the release of the halogen by free radical attack resulting in a free uracil radical. Instability in the DNA backbone is then induced through abstraction of a hydrogen atom from the deoxyribose of DNA (Prusoff *et al.* 1979). In addition to being a radiosensitizer, IUdR is the vehicle in which iodine is incorporated into DNA, where it becomes the activator of Auger electrons when irradiated with photons of an appropriate energy (Laster *et al.* 1993).

IUdR is suitable for photo-activated Auger electron therapy because (1) of its ability to incorporate into DNA by substituting the base pair thymidine during S-phase of the cell cycle (see Section 1.3.1), (2) the selectivity of rapidly dividing cells and sufficient quantity that incorporates into DNA makes it possible for IUdR to target fast growing tumors, (3) iodine produces photoelectric events when irradiated with the optimal photon energy that translate to Auger electrons and ultimately DSBs (with acceptable toxicity) (see Sections 1.3.2 and 1.3.3), and (4) for the high-Z atom iodine, the energy at which photo-activated Auger electrons are released (E_K = 33.2 keV) is just sufficiently high to penetrate a useful depth in the body ($HVL_{water} \approx 3.4$ cm for broad beam geometry) (see Section 1.3.3.1). Utilizing IUdR in photo-activated Auger electron therapy on patients with high-grade brain tumors could potentially minimize problems associated with radiosensitization of normal tissues since these rapidly proliferating (potential tumor doubling times of 5 to 15 days) radioresistant tumors are surrounded by non-proliferating normal brain tissues that show little to no DNA incorporation of IUdR (Fairchild & Bond 1984, Kinsella 1996, Saif *et al.* 2007).

1.5 Pre-Clinical & Clinical Studies with IUdR

1.5.1 Conventional X-Ray Energy Irradiations with IUdR

X-rays from sources such as ^{137}Cs (662 keV), ^{60}Co (1.17 and 1.33 MeV), and clinical linear accelerator energies of 4-15 MV induce a response in tissue that is primarily from Compton scattering (i.e., no photoelectric interactions releasing Auger electrons), so the effects of radiosensitization alone in IUdR can be studied. In this energy range (low linear-energy transfer (LET)), IUdR has been shown as an effective *in vitro* radiosensitizer with sensitization enhancement ratios at the 10% survival level (SER_{10}; discussed in Section 4.2.4) that are dependent on cell line, ranging from 1.8-2.6 (Fairchild *et al.* 1985, Miller *et al.* 1987, Nath *et al.* 1987, Shinohara *et al.* 1996, Dugas *et al.* 2011) (see Table 1.5).

Results from small animal investigations using various IUdR infusion schemes have been promising. Deutsch *et al.* (1990) showed improved median survival of rats with brain gliosarcoma after receiving 24 Gy in three fractions with IUdR + 4 MV x-rays (30.5 days), as compared to IUdR (21.5 days) or 4 MV x-rays (19.5 days) alone. Harrington *et al.* (2004) showed improvement in the volume tripling time of KB xenographs in mice receiving 15 Gy in five fractions using an encapsulated IUdR called pegylated liposomal IUdR (PLIUdR) + ^{137}Cs x-

Table 1.5: SER_{10} values for CHO, V79, and HeLa cells containing similar amounts of IUdR. Cells were irradiated with either ^{137}Cs (662 keV), ^{60}Co (1.17 and 1.33 MeV), 4 MV, or 15 MV x-rays. Irradiations at these energies induce primarily Compton interactions (i.e., no photon activation), so the effects of radiosensitization alone in IUdR can be studied.

Energy	%IUdR	IUdR Exposure Time	SER_{10}	Cell Line	Reference
Cs-137	20%	12 hrs	2.0	V79	Fairchild *et al.* 1985
Co-60	20%	18 hrs	1.8	HeLa	Shinohara *et al.* 1996
4 MV	18.1%	3 days	2.2	CHO	Nath *et al.* 1987
4 MV	16.6 ± 1.9%	27 hrs	2.6	CHO	Dugas *et al.* 2011
15 MV	16%	17 hrs	2.0	V79	Miller *et al.* 1987

rays (34 days), as compared to PLIUdR (9 days) or ^{137}Cs x-rays (19 days) alone. Combinations of conventional radiation with the less toxic prodrug IPdR have been found to significantly inhibit growth of human colorectal and glioblastoma xenografts over inhibition due to radiation alone (Kinsella *et al.* 2000a, Kinsella *et al.* 2007).

In clinical trials, however, IUdR failed to exhibit significant radiosensitization in early studies because normal tissue toxicity limited uptake into the tumor. For example, Schulz *et al.* (2004) showed maximum uptakes of 4.9% IUdR in granulocytes of human malignant glioma patients, but also exhibited significant toxicities (see Section 1.3.2). In other clinical trials, such as that reported by Epstein *et al.* (1992), tumor responses were mixed. Recently, though, there is promising research with the oral prodrug IPdR due to more favorable pharmacokinetics leading to the first human phase 0 trial (Kummar *et al.* 2013) (discussed in Section 1.3.2). It is likely that human clinical trials with radiation therapy will follow in the near future.

1.5.2 Monochromatic X-Ray Energy Irradiations with IUdR

Knowing how to best use monochromatic x-rays to increase the local dose to DNA from Auger electrons (see Section 1.3.3) is important for the clinical success of photo-activated Auger electron therapy with IUdR. Work done by Laster *et al.* (1993) (discussed in Section 1.3.3.2) studied the use of IUdR and the biologic efficacy of Auger electrons when monochromatic photons were used to photo-activate IUdR *in vitro.* Using V79 cells with 16% IUdR, they reported that IUdR had a SER_{10} value of 3.0 ± 0.2 for 33.4 keV photons. Also, 33.4 keV photons were found to be a factor of 1.4 more effective than 32.9 keV photons in damaging iodinated cells (see Figure 1.7 in Section 1.3.3.2). They also reported a SER_{10} value of 2.0 for ^{137}Cs irradiation (see Table 1.5). Hence, the therapeutic gain in SER_{10} from Auger electrons was approximately 1.5 (3.0/2.0). Nath *et al.* (1987) studied the survival of CHO cells with and

without IUdR (18% IUdR) for 250 kVp and 4 MV x-rays, and the results showed SER_{10} values of 3.2 and 2.2, respectively. This indicates a therapeutic gain in SER_{10} as a result of Auger electrons to be 1.5 (3.2/2.2). Karnas *et al.* (1999) studied the survival of CHO cells with and without IUdR (18% IUdR) for three different polychromatic x-ray beams, and their data showed SER_{10} to be greatest (3.0) for their tungsten-filtered 100 kVp x-ray beam.

Dugas *et al.* (2011) investigated *in vitro* the dependence of CHO cell survival on thymidine replacement levels of 9.2%, 12.0%, and 16.6% using 35 keV monochromatic photons. Figure 1.8(a) plots surviving fraction ($\pm 1\sigma$) versus dose to water, with the upper curve showing data for CHO cells without IUdR irradiated by either 4 MV x-rays or 35 keV photon beams, for which there was no significant difference in the survival curve, and the lower curve showing data for CHO cells with IUdR replacing 16.6% thymidine irradiated by the 4 MV x-ray beam. The solid line represents the fit to the linear quadratic (survival) model. Based on fits to the linear quadratic model, the SER_{10} value was 2.6. This demonstrates the temporary ability of IUdR to compromise DNA repair (i.e., radiosensitization effect). Figure 1.8(b) compares the results from Figure 1.8(a) to data for CHO cells irradiated at 35 keV. Based on the fit to the linear quadratic model, the SER_{10} value for the (4 MV & 35 keV, 0% IUdR) versus (35 keV, 16.6% IUdR) data was 4.1. This is due to the combined effects of radiosensitization and Auger events. Compared to a SER_{10} value of 2.6 for the (4 MV & 35 keV, 0% IUdR) versus (4 MV, 16.6% IUdR) data, the Auger effect resulted in a therapeutic gain of 1.6 (4.1/2.6).

Looking at lower IUdR concentrations, Figure 1.9(a) and (b) show results for CHO cells with or without 12.0% and 9.2% IUdR and irradiated at 4 MV or 35 keV. Comparing Figure 1.8(b) to Figure 1.9(a), the SER_{10} values are reduced from 4.1 to 3.0 for 35 keV and from 2.6 to 2.2 for 4 MV. This corresponds to a decrease in the SER_{10} as a result of the Auger effect from 1.6

to 1.4. Comparing Figure 1.8(b) to Figure 1.9(b), the SER_{10} value is reduced to 2.0 for 35 keV and to 1.5 for 4 MV x-rays. This corresponds to a decrease in the SER_{10} to 1.3 for 9.2% IUdR as a result of the Auger effect.

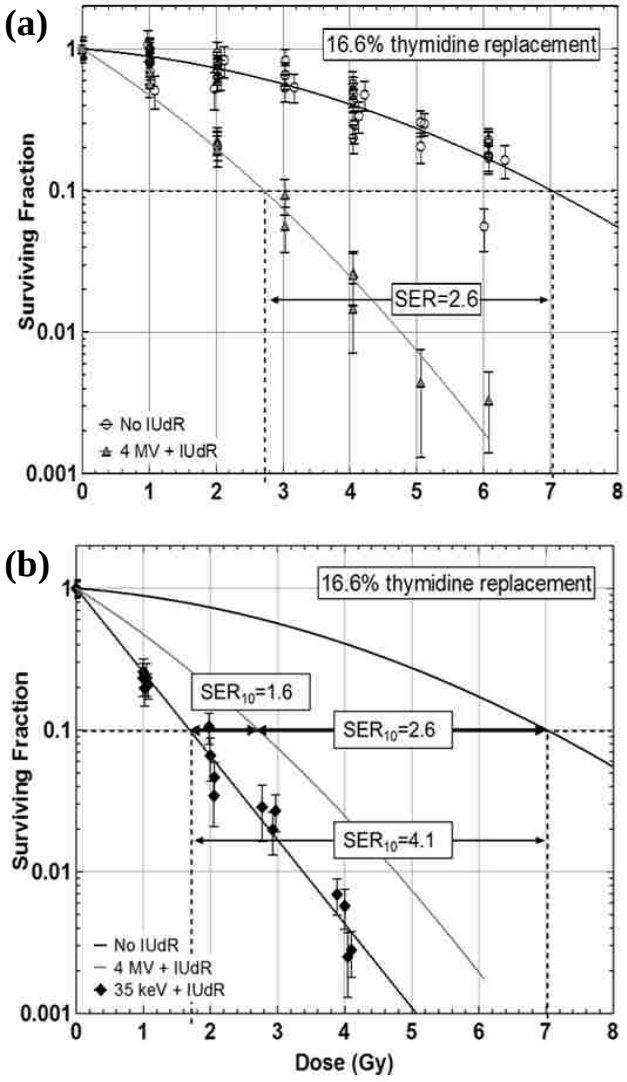

Figure 1.8: CHO cells with 16.6% IUdR irradiated at 4 MV or 35 keV. (a) Cells with IUdR irradiated at 4 MV compared to cells without IUdR irradiated at either 4 MV or 35 keV. A SER_{10} value of 2.6 is observed for cells irradiated at 4 MV due to the radiosensitization effect of IUdR. (b) Cells irradiated at 35 keV. A SER_{10} of 4.1 is observed due to the radiosensitizing effect of IUdR and the Auger effect (Dugas *et al.* 2011).

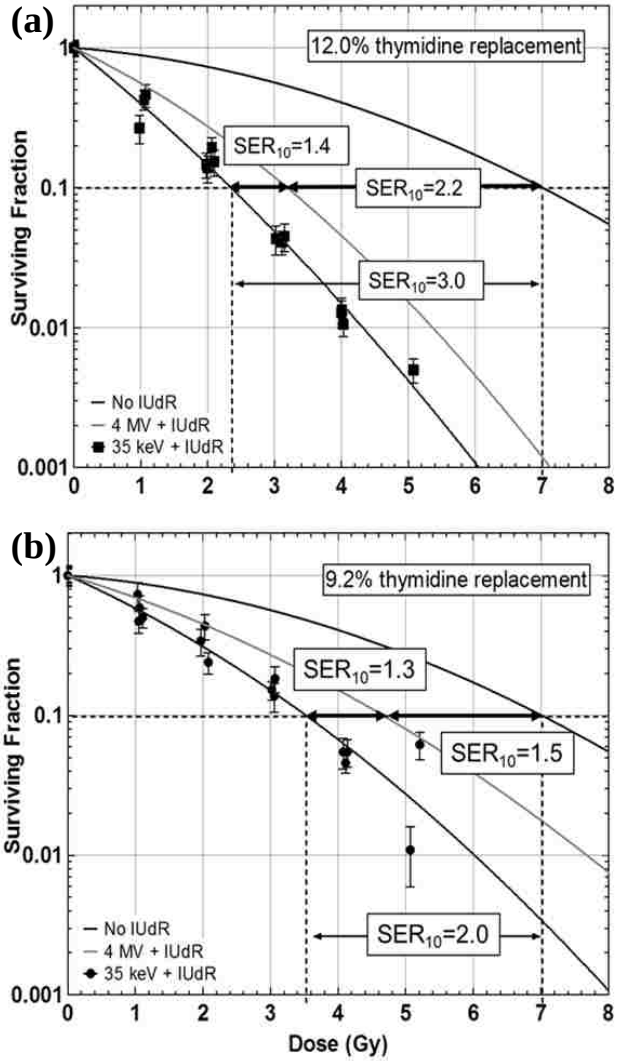

Figure 1.9: CHO cells with 12.0% and 9.2% IUdR irradiated at 4 MV and 35 keV. (a) Cells with or without 12.0% IUdR irradiated at 4 MV and 35 keV. A SER_{10} of 3.0 is observed due to the radiosensitizing effect of IUdR and Auger effect. (b) Cells with or without 9.2% IUdR irradiated at 4 MV and 35 keV. A SER_{10} of 2.0 is observed due to the radiosensitizing effect of IUdR and Auger effect (Dugas *et al.* 2011).

From these results, Dugas and colleagues concluded that SER_{10} values for both 4 MV and 35 keV x-rays increased monotonically with increasing %IUdR from 9.2% to 16.6%. At each %IUdR level, the therapeutic gain was greater for 35 keV than for 4 MV, although the benefit

from radiosensitization due to IUdR was greater than that from Auger electrons contributing additional dose to the DNA using 35 keV. Even though the Auger effectiveness was less than the radiosensitization factor of IUdR, the authors believed that both effects could be important for the clinical efficacy of IUdR radiotherapy.

For *in vitro* SQ20B human cells (estimated 10-20% IUdR) Corde *et al.* (2004) showed survival curves with SER_{10} values of 1.25, 1.64, 2.60, and 1.45 at photon beam energies of 32.8, 33.5, 50, and 70 keV, respectively, (see Figure 1.10). Their greatest SER_{10} value (2.60) occurred at 50 keV, consistent with the theoretical DER peak (see Figure 1.5 in Section 1.3.3.1). In contrast to the optimal energy reported by Corde *et al.*(2004), Rousseau *et al.* (2009) showed no significant differences in median survival of rats with F98 glioma that received 15 Gy in one fraction when using IUdR + 50 keV photons (46 days) and 50 keV photons alone (44 days).

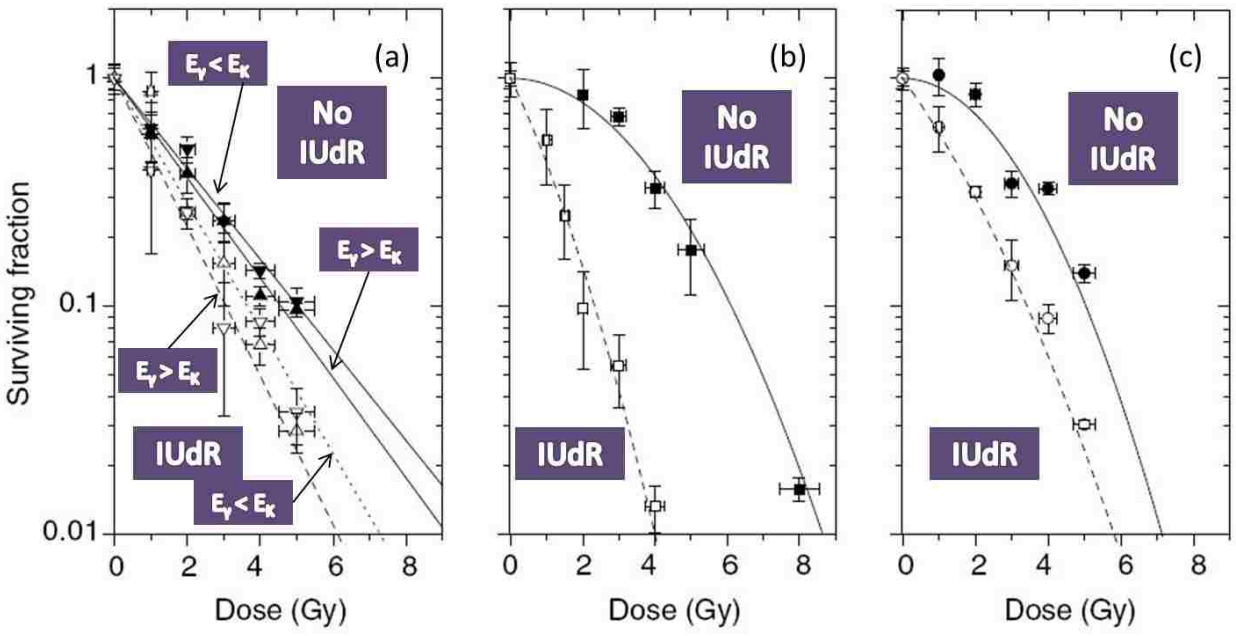

Figure 1.10: Survival curves for SQ20B cells. Cell were irradiated with (open symbols) or without (closed symbols) 10 μM IUdR for the energies (a) below the iodine K-edge (32.8 keV; triangles) and above the iodine K-edge (33.5 keV; reversed triangles), (b) 50 keV (squares), and (c) 70 keV (circles) (Corde *et al.* 2004).

Corde's *et al.* (2004) data for E_γ (= 32.8 keV) < E_K in Figure 1.10(a) is unusual. First, there is no shoulder in the survival curves for cells irradiated without IUdR, a prominent feature in survival curves of cells with no radiosensitizing agent. Second, the ratio of SER_{10} values above and below the K-edge was 1.33, somewhat lower than values ranging from 1.4-1.6 reported by others in this section. Third, the data presented in Corde *et al.* (2004) is also limited in that only two energies above 33.5 keV were explored. As of this writing, however, it is the only published data with energies well above the K- edge of iodine.

Recent studies by the LSU-MBPCC research group have aimed at understanding the dependence of the Auger effect on cell survival as a fraction of % thymidine replacement by IUdR (%IUdR) and photon energy, E_γ. The former has been studied at 35 keV by Dugas *et al.* (2011), and current studies by this group are investigating the latter over the energy range 25-70 keV, as the Corde *et al.* (2004) data has too many inconsistencies and too few energy data points to discern between observed SER_{10} values being related to the DER or the number of Auger events per unit dose. The present study has looked at data in the range of 25-35 keV.

1.6 Purpose, Hypothesis, & Aims

Because the potential for photo-activated Auger electron therapy cannot be realized until there is a better understanding of basic mechanisms, this project aims to understand the biological effect of 9% and 18% IUdR incorporated into rat 9L glioma cells as a function of photon energy (25-35 keV).

- Hypothesis: It was postulated that the SER_{10} value for 9% and 18% IUdR-laden rat 9L glioma cells irradiated by 25-35 keV photons will be greatest at 35 keV due to the Auger effect.

  This hypothesis will be tested by completing three aims:

- Aim 1, IUdR Incorporation: Rat 9L glioma cells will be grown with IUdR replacing 9% and 18% thymidine in the DNA.
- Aim 2, Cell Survival Measurements: Survival curves for 9L glioma cells with 0%, 9%, and 18% thymidine replacement will be measured with 4 MV x-rays and 25-35 keV photon beams.
- Aim 3, Data Analysis: A survival curve will be fit to data for each combination of % thymidine replacement and photon beam energy using a linear quadratic model for surviving fraction, from which SER_{10} values will be determined.

CHAPTER 2: AIM 1, IUDR INCORPORATION

Aim 1: Rat 9L glioma cells will be grown with IUdR replacing 9% and 18% of thymidine in the DNA.

2.1 Goal

The goal of this aim is to determine the appropriate concentration of IUdR required in growth medium such that 9% or 18% of thymidine is replaced by IUdR in the DNA of 9L glioma cells during cell synthesis. This will allow cell survival measurements of 9L cells with 0%, 9%, and 18% IUdR thymidine replacement using 25 keV, 30 keV, 35 keV, and 4 MV x-rays.

2.2 Materials & Methods

2.2.1 Cell Line

Rat 9L glioma cells, supplied by C. J. Koch, Ph.D. (Evans *et al.* 1995), of the University of Pennsylvania, were chosen for this study from other available cell lines because 9L cells are radioresistant and will grow both *in vitro* and *in vivo* (Leith *et al.* 1975, Weizsaecker *et al.* 1981) (the possibility of implantation into syngeneic rats for *in vivo* animal studies is important for future work). 9L cells reflect the situation encountered clinically with human gliomas where radiotherapy has been ineffective in producing cures.

Two additional characteristics make 9L cells a good cell line for the present study. First, the number of cells that survive plating from generation to generation (i.e., the plating efficiency) is 45% ± 15%, making it easy to count the number of cells required to be plated for maintenance of cells and experiments. Second, they have a doubling time of approximately 16 hours, as preliminary measurements in this study indicated, which keeps the time required to wait for cells to proliferate within a manageable range.

Cells were maintained in log-phase growth and were grown in Debulcco's Modified Eagle Medium (Gibco®, Life Technologies Corp., Grand Island, NY) supplemented with 10% fetal bovine serum (Hyclone®, Thermo Fisher Scientific, Inc., Logan, UT), 20 mM Hepes (N-(2-hydroxyethyl)piperazine-N'-2-ethanesulfonic acid) buffer, and approximately 0.5% V/V penicillin/streptomycin (Sigma-Aldrich, St. Louis, MO). The cells were maintained at 37^{o}C inside a water-jacketed incubator with humidified air containing 5% CO_2 (i.e., standard conditions) in the tissue culture facility at the LSU Pennington Biomedical Research Center (PBRC). Cells were tested and confirmed free of mycoplasmal contamination using a kit purchased from Bionique® Testing Laboratories, Inc. (Saranac Lake, NY).

2.2.2 IUdR Uptake Studies

A modified method from Miller *et al.* (1987), as described in Dugas *et al.* (2011), was used to determine the percentage of IUdR incorporated into the DNA of 9L cells. Cell culture flasks containing approximately 2 x 10^5 cells were prepared. Radiolabeled IUdR was added the next day. Medium containing a mixture of 0.004 μCi*mL^{-1} of ^{125}I-IUdR (Perkin-Elmer, Inc., Billerica, MA) and either 1 or 3 μM non-radiolabeled IUdR was added to the cell culture flasks. Two 200 μL aliquots were immediately removed from each cell culture flask, before any DNA incorporation could occur, and stored in a refrigerator for determining the activity of the medium overlay. The activity of the medium was used to correct for radioactive decay occurring between the times of radiolabeling of the cells and reading the activity levels of all the cell cultures.

The cell cultures were allowed to incubate for 27 hours at standard conditions to allow at least one doubling time (i.e., one generation of daughter cells) for uptake and incorporation of the radiolabeled IUdR into their DNA. After the incubation period, the overlay medium was removed from each cell culture flask and discarded. The cell cultures were then washed with

Hank's balanced salt solution to eliminate any remaining residual medium. The DNA of each cell culture was then extracted, purified, precipitated, and rehydrated using a Wizard Genomic DNA Purification Kit (Promega Corp., Madison, WI) using the protocol outlined in Appendix B.

The extracted DNA of each cell culture was rehydrated using 250 µL of rehydration solution. A 200 µL aliquot of the resulting DNA solution was used for assaying radioactivity in the form of counts per minute (*cpm*). The counts per minute for each 200 µL aliquot of rehydrated DNA solution (cpm_{DNA}), and both reserved 200 µL aliquots of the medium overlay ($cpm_{overlay}$), were read twice consecutively using a Cobra II Auto-Gamma Counter (Packard Instrument Co., Inc., Meriden, CT). Each reading was corrected for background by subtracting the background counts per minute (i.e., counter reading with sample removed). The multiple readings per aliquot were averaged to get a single cpm reading.

The following equation, derived from the equations used to calculate % thymidine replacement in Dugas *et al.* (2011), was used to calculate the %IUdR for each rehydrated DNA solution:

$$\%\, IUdR = \frac{cpm_{DNA} * MW_{DNA} * C_{IUdR} * V_{overlay}}{cpm_{overlay} * C_{DNA} * V_{DNA}} * 100, \qquad (2.1)$$

where:

cpm_{DNA} = Counts per minute for the 200 µL rehydrated DNA solution (cpm),

MW_{DNA} = Molecular weight of two base pairs (1 adenine + 1 thymidine + 1 cytosine + 1 guanine) = 1.29×10^3 g*mol^{-1},

C_{IUdR} = Molar concentration of IUdR initially added to medium overlay (M = mol*L^{-1}),

$V_{overlay}$ = Volume of medium overlay aliquot = 2×10^{-4} L,

$cpm_{overlay}$ = Counts per minute for the 200 µL medium overlay aliquot (cpm),

C_{DNA} = Concentration of rehydrated DNA solution = $\varepsilon * A_{260\,nm}$,

where ε = Extinction coefficient for DNA = 0.05 $g*L^{-1}$,

A_{260nm} = Measurement of absorbance of rehydrated DNA solution at 260 nm (unitless),

V_{DNA} = Volume of rehydrated DNA solution (200 µL) + 400 µL rehydration solution = 6×10^{-4} L.

To calculate the concentration of DNA in the solution, the 200 µL aliquots of rehydrated DNA solution used to measure cpm_{DNA} were diluted with an additional 400 µL of rehydration solution and transferred into a quartz cuvette for measurement of the absorbance at 260 nm (A_{260nm}) and 280 nm (A_{280nm}) using a Genesys 10 UV Spectrophotometer (Thermo Fisher Scientific, Inc., Waltham, MA). The spectrophotometer exposed each DNA solution to ultraviolet light (260 nm wavelength), and a photon detector measured the light that passed through the DNA solution. Using the Beer-Lambert law, the amount of light absorbed by the DNA solution was related to the concentration of the absorbing molecule. At a wavelength of 260 nm, the average extinction coefficient for double-stranded DNA is 50 $\mu g*mL^{-1}$.

The ratio of the absorbances at 260 nm and 280 nm ($A_{260/280}$) was used to assess the purity of the DNA solution for quality assurance. Pure DNA has an $A_{260/280} > 1.75$, and in practice, $A_{260/280}$ = 1.75-1.96. Therefore, samples with $A_{260/280} < 1.75$ were considered contaminated and were discarded.

For calculation purposes, one molecule of DNA was taken to be two base pairs (1 adenine + 1 thymidine + 1 cytosine + 1 guanine). By this definition, the molecular weight of one mole of DNA (i.e., 2 base pairs) is 1.29×10^3 g (Dugas *et al.* 2011). Following this logic, when calculating the %IUdR in a DNA solution, the number of molecules of thymidine equals the number of molecules of DNA.

2.2.3 Data Acquisition & Analysis

IUdR concentrations between 1 and 5 μM were selected for generating the relationship between IUdR and thymidine replacement. Three to four experiments were conducted for each concentration of 1, 2, 3, and 5 μM IUdR. For experiments at each concentration, 2-3 cell culture flasks were used with each cell culture flask resulting in one data point. All data points were aggregated for each concentration (9-12 data points per concentration), making up a data set for a particular concentration, and the mean % thymidine replacement was computed. Data points were tested for outliers using Chauvenet's criterion (Bevington 1992). If any data points for a particular IUdR concentration were considered outliers, they were removed from the data set, and the mean thymidine replacement was re-calculated. The mean thymidine replacement was then plotted against IUdR concentration and fitted using a weighted least squares fit from which reduced-chi squared was calculated. The standard error of the mean (SEM) was used as the uncertainty in the mean thymidine replacement data.

2.3 Results & Discussion

Based on previous CHO cell data from Dugas *et al.* (2011), initial IUdR uptake studies were done with various concentrations of IUdR (2-20 μM) in multiple trials to determine what concentration yielded the targeted 9% and 18% replacement. It was found, however, that rat 9L glioma cells take up IUdR more readily than CHO cells (see Table 2.1). For example, incubating cells with 5 μM IUdR for a 27-hour period resulted in 26.4% thymidine replacement in 9L cells as opposed to 9.2% in CHO cells.

There are two possible explanations for the differences in uptake efficiency between 9L cells and CHO cells shown in Table 2.1. The most likely explanation is the medium used to feed

Table 2.1: Percent thymidine replacement in CHO cells versus rat 9L glioma cells. CHO data reported by Dugas *et al.* (2011). Incubation period was 27 hours for the indicated concentrations of IUdR.

IUdR concentration (μM)	Percent thymidine replacement (mean +/- standard deviation)	
	CHO cells	9L glioma cells
1.65	-	11.5 % ± 1.1%
2	5.7% ± 0.1%	15.1% ± 1.2%
5	9.2% ± 1.3%	26.4% ± 0.85%
10	12.0% ± 1.4%	27.7% ± 2.95%
20	16.6% ± 1.9%	35.4% ± 5.62%

each cell line. The recommended medium for CHO cells is Ham's F-12 nutrient mix (Gibco®, Life Technologies Corp., Grand Island, NY), which contains 2.89 μM thymidine, as quoted from the company's website. The Dulbecco's Modified Minimal Essential Medium used for rat 9L glioma cells contained no thymidine. It is possible that in the chemical competition between thymidine in the Ham's F-12 medium and the IUdR in the medium overlay, that CHO cells preferentially incorporate thymidine from the Ham's F-12 medium before taking up IUdR via the salvage pathway. In the salvage pathway, nucleotide bases are recovered from the medium and reconnected to a ribose unit. In a different DNA synthesis pathway (*de novo*) the nucleotide bases are assembled using basic nutrients in the medium. Most animal cells can synthesize purine and pyrimidine nucleotides *de novo* from simpler carbon and nitrogen compounds, rather than from already formed purines and pyrimidines (Lodish *et al.* 1995). However, according to Kinsella (1996), IUdR is incorporated into DNA via the enzymes of the salvage pathway.

The other possibility is the differences in activities of mismatch repair (MMR) enzymes. Berry *et al.* (1999) demonstrated that human colon cancer cells deficient in mismatch repair incorporate and retain 2-3 times as much IUdR in their DNA as their normal counterparts. No studies have been found reporting MMR deficiency in 9L or other glioma cell lines.

Results for the mean thymidine replacement (MTR %) versus IUdR concentration (μM) in 9L cell cultures after a 27-hour exposure are plotted in Figure 2.1 and listed in Table 2.2. Results at 1 μM and 3 μM IUdR of 8.5% ± 0.1% and 17.6% ± 0.1% thymidine replacement (%MTR ± σ_{SEM}), respectively, were close to the goal of 9% and 18%, respectively. Figure 2.1 compares a plot of the measured data, mean thymidine replacement versus IUdR concentration, with a numerical curve-fit.

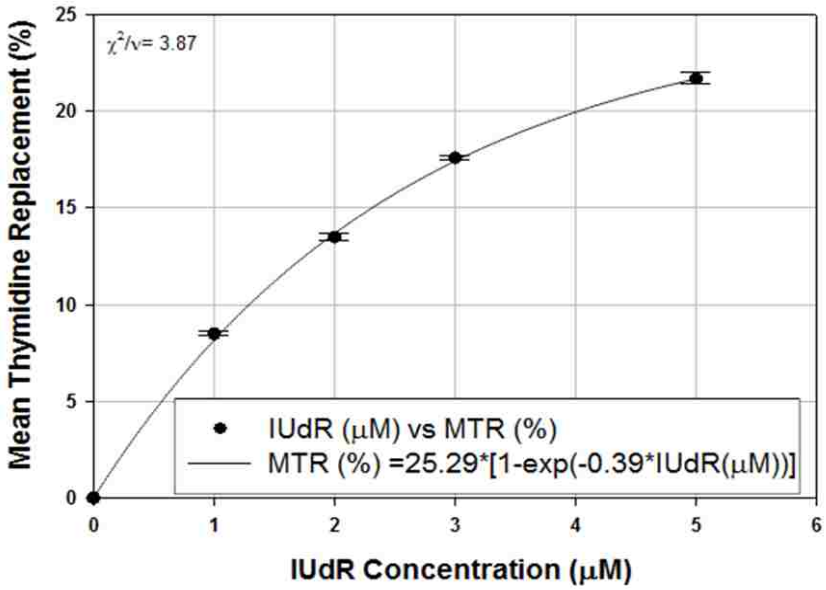

Figure 2.1: Plot of mean thymidine replacement (%) versus IUdR concentration (μM). 9L cells were incubated for 27 hours. Measured data points (±σ_{SEM}) compared with least squares fit to data.

Table 2.2: IUdR incorporation as a function of the IUdR concentration in the medium overlying rat 9L glioma cells during a 27-hour incubation period.

IUdR concentration in overlay (μM)	# of experiments	Total # of data points	Mean thymidine replacement (%) (mean ± SEM)	Standard deviation
1	4	12	8.5% ± 0.1%	0.4%
2	4	12	13.5% ± 0.2%	0.7%
3	4	11	17.6% ± 0.1%	0.5%
5	3	9	21.7% ± 0.3%	0.8%

CHAPTER 3: AIM 2, CELL SURVIVAL MEASUREMENTS

Aim 2: Survival curves for rat 9L glioma cells with 0%, 9%, and 18% IUdR will be measured with 4 MV x-rays and 25-35 keV monochromatic photon beams.

3.1 Goal

The goal of this aim was to measure the difference in survival curves (surviving fraction versus dose) for 9L glioma cells as a function of modality (i.e., 4 MV bremsstrahlung versus 25 keV, 30 keV, and 35 keV monochromatic x-rays) and %IUdR levels (0%, 9%, and 18% thymidine replacement in the DNA). To ensure reliable results, photon energies and dose must be measured and irradiation geometry must be verified. Also, methods to assess differences in survival curves and to determine measurement uncertainties in cell survival data must be utilized.

3.2 Methods of Measurement & Materials

3.2.1 4 MV X-Ray Irradiations

3.2.1.1 Properties of 4 MV Beam

4 MV bremsstrahlung x-rays were generated using a Clinac 21EX radiotherapy linear accelerator or "linac" (SN 1412, Varian Medical Systems, Inc., Palo Alto, CA). Properties of the beam, such as tissue-phantom ratios (*TPR*) and output factors, are given in Table 3.1. Because this is a clinically commissioned linac, the energy is checked during monthly quality assurance assessments by qualified medical physicists, as recommended in the American Association of Physicists in Medicine (AAPM) TG-40 (Kutcher *et al.* 1994). During a monthly QA, the dose output is measured at two points on the percent depth dose curve, at depths of 5 cm and 10 cm in Solid Water® (GAMMEX rmi, Middleton, WI). If the ratio of the two dose outputs are within 2% of the commissioned value, the energy is considered calibrated. The accelerator tolerances of the radiation field are not to exceed 2% non-uniformity and 3% asymmetry for photons.

Table 3.1**:** 4 MV central-axis dosimetry data for Clinac 21EX radiotherapy linac. (a) Tissue-phantom ratios, (b) output factors for collimator scatter (S_c), patient scatter (S_p), and the combined measured scatter for collimator and patient (S_c*S_p). Data are normalized for 10 x 10 cm^2 field size, 10 cm depth at isocenter, and 100 cm source to point distance (courtesy of Mary Bird Perkins Cancer Center).

MARY BIRD PERKINS CANCER CENTER

4 MV PHOTONS
VARIAN CLINAC-21EX SN: 1412
TISSUE PHANTOM RATIOS

TPR

(a)

Dosimetry normalized at 10cm. Field sizes and depths are in cm

Field Size	17x17	18x18	19x19	20x20	21x21	22x22	24x24	26x26	28x28	30x30	32x32	34x34	36x36	38x38	40x40
Depth															
0.0	0.842	0.847	0.851	0.856	0.861	0.867	0.878	0.889	0.900	0.909	0.918	0.924	0.928	0.929	0.927
0.5	1.206	1.202	1.199	1.197	1.195	1.194	1.194	1.195	1.197	1.198	1.199	1.197	1.192	1.184	1.172
1.0	1.276	1.269	1.264	1.260	1.256	1.253	1.249	1.247	1.246	1.245	1.243	1.240	1.235	1.226	1.214
1.2	1.304	1.295	1.291	1.285	1.278	1.273	1.265	1.258	1.253	1.248	1.243	1.237	1.231	1.226	1.220
1.5	1.296	1.287	1.282	1.276	1.269	1.265	1.258	1.252	1.247	1.241	1.236	1.231	1.226	1.222	1.217
2.0	1.284	1.275	1.272	1.267	1.260	1.255	1.248	1.242	1.237	1.232	1.227	1.222	1.217	1.212	1.207
2.5	1.274	1.265	1.262	1.257	1.250	1.244	1.236	1.229	1.226	1.222	1.219	1.214	1.210	1.205	1.200
3.0	1.257	1.249	1.247	1.243	1.238	1.232	1.226	1.220	1.216	1.212	1.209	1.204	1.200	1.195	1.190
3.5	1.242	1.234	1.231	1.226	1.222	1.217	1.211	1.206	1.201	1.197	1.193	1.189	1.185	1.181	1.178
4.0	1.225	1.217	1.215	1.210	1.206	1.201	1.196	1.191	1.187	1.183	1.179	1.176	1.173	1.170	1.168
4.5	1.209	1.201	1.199	1.195	1.191	1.187	1.183	1.179	1.175	1.170	1.166	1.163	1.160	1.157	1.154
5.0	1.191	1.184	1.183	1.180	1.177	1.172	1.168	1.163	1.160	1.156	1.154	1.151	1.148	1.145	1.142
5.5	1.174	1.168	1.167	1.163	1.159	1.155	1.151	1.146	1.143	1.141	1.139	1.136	1.133	1.131	1.128
6.0	1.156	1.152	1.153	1.151	1.149	1.145	1.138	1.131	1.127	1.125	1.124	1.122	1.119	1.117	1.114
6.5	1.133	1.127	1.126	1.124	1.121	1.117	1.115	1.112	1.111	1.109	1.108	1.106	1.105	1.103	1.102
7.0	1.114	1.110	1.110	1.108	1.107	1.104	1.101	1.098	1.096	1.094	1.093	1.091	1.090	1.088	1.087
7.5	1.094	1.092	1.091	1.089	1.088	1.085	1.084	1.081	1.080	1.079	1.079	1.078	1.077	1.075	1.074
8.0	1.076	1.075	1.074	1.073	1.072	1.071	1.068	1.066	1.064	1.063	1.062	1.062	1.061	1.060	1.059
8.5	1.058	1.058	1.057	1.056	1.056	1.055	1.052	1.049	1.047	1.046	1.046	1.045	1.045	1.045	1.044
9.0	1.040	1.039	1.039	1.038	1.038	1.037	1.035	1.033	1.032	1.031	1.030	1.030	1.030	1.029	1.029
9.5	1.019	1.019	1.019	1.019	1.019	1.019	1.018	1.017	1.016	1.016	1.016	1.016	1.016	1.015	1.015
10.0	1.000	1.000	1.000	1.000	1.000	1.000	1.000	1.000	1.000	1.000	1.000	1.000	1.000	1.000	1.000
10.5	0.982	0.982	0.982	0.981	0.981	0.980	0.981	0.981	0.982	0.982	0.982	0.983	0.983	0.984	0.984
11.0	0.960	0.961	0.961	0.961	0.962	0.962	0.961	0.961	0.961	0.963	0.965	0.967	0.968	0.969	0.970
11.5	0.941	0.941	0.942	0.943	0.944	0.944	0.947	0.949	0.951	0.951	0.952	0.952	0.952	0.953	0.953
12.0	0.922	0.923	0.924	0.925	0.926	0.927	0.928	0.930	0.931	0.933	0.934	0.936	0.937	0.938	0.939
12.5	0.905	0.907	0.908	0.909	0.911	0.912	0.913	0.914	0.915	0.916	0.918	0.920	0.922	0.923	0.925
13.0	0.884	0.886	0.889	0.889	0.891	0.893	0.894	0.896	0.897	0.900	0.903	0.907	0.909	0.911	0.912
13.5	0.868	0.870	0.873	0.873	0.875	0.876	0.879	0.882	0.884	0.887	0.889	0.892	0.894	0.896	0.898
14.0	0.853	0.856	0.859	0.859	0.861	0.862	0.864	0.867	0.869	0.872	0.874	0.877	0.879	0.881	0.882
14.5	0.834	0.836	0.840	0.841	0.843	0.844	0.847	0.850	0.853	0.856	0.859	0.862	0.865	0.867	0.869
15.0	0.817	0.819	0.823	0.824	0.825	0.827	0.831	0.834	0.838	0.840	0.843	0.845	0.848	0.850	0.853
15.5	0.796	0.800	0.805	0.806	0.808	0.811	0.815	0.818	0.821	0.824	0.827	0.830	0.832	0.835	0.837
16.0	0.782	0.785	0.789	0.790	0.792	0.794	0.798	0.802	0.806	0.809	0.813	0.816	0.819	0.821	0.824
16.5	0.764	0.768	0.773	0.774	0.777	0.779	0.783	0.787	0.791	0.793	0.796	0.798	0.801	0.803	0.806
17.0	0.750	0.754	0.758	0.759	0.761	0.763	0.767	0.771	0.775	0.778	0.780	0.782	0.784	0.787	0.790
17.5	0.733	0.737	0.742	0.743	0.746	0.748	0.753	0.756	0.759	0.762	0.767	0.771	0.774	0.778	0.781
18.0	0.715	0.721	0.726	0.728	0.731	0.734	0.740	0.743	0.747	0.750	0.754	0.757	0.760	0.763	0.766
18.5	0.700	0.705	0.710	0.712	0.715	0.718	0.724	0.728	0.732	0.736	0.740	0.743	0.746	0.750	0.753
19.0	0.686	0.690	0.695	0.699	0.700	0.703	0.709	0.711	0.714	0.717	0.722	0.727	0.732	0.736	0.740
19.5	0.666	0.671	0.676	0.679	0.681	0.685	0.691	0.696	0.702	0.707	0.711	0.716	0.720	0.724	0.727
20.0	0.654	0.659	0.664	0.667	0.669	0.673	0.679	0.683	0.688	0.692	0.696	0.700	0.704	0.708	0.712
21.0	0.624	0.630	0.635	0.638	0.640	0.642	0.648	0.652	0.657	0.662	0.667	0.673	0.677	0.682	0.686
22.0	0.597	0.602	0.608	0.612	0.614	0.617	0.623	0.627	0.632	0.636	0.642	0.647	0.652	0.657	0.661
23.0	0.569	0.574	0.580	0.584	0.587	0.591	0.598	0.603	0.608	0.612	0.617	0.622	0.626	0.631	0.635
24.0	0.548	0.554	0.561	0.564	0.566	0.569	0.575	0.579	0.584	0.589	0.594	0.598	0.602	0.606	0.610
25.0	0.519	0.524	0.529	0.533	0.537	0.540	0.547	0.553	0.560	0.565	0.571	0.575	0.579	0.582	0.586
26.0	0.495	0.501	0.507	0.511	0.516	0.519	0.527	0.533	0.537	0.541	0.545	0.550	0.555	0.560	0.564
27.0	0.474	0.479	0.483	0.487	0.491	0.494	0.501	0.506	0.512	0.517	0.523	0.528	0.533	0.537	0.542
28.0	0.449	0.454	0.460	0.464	0.468	0.471	0.480	0.487	0.493	0.498	0.504	0.508	0.512	0.515	0.519
29.0	0.430	0.436	0.442	0.447	0.451	0.453	0.461	0.466	0.471	0.475	0.480	0.485	0.490	0.495	0.499
30.0	0.410	0.415	0.421	0.425	0.428	0.431	0.439	0.445	0.452	0.459	0.466	0.470	0.473	0.476	0.478

Table 3.1 (continued)

MARY BIRD PERKINS CANCER CENTER

4 MV PHOTONS
VARIAN CLINAC 21EX SN: 1412

S_{cp} / TF

(b)

Output Factors

Dosimetry normalized at 10cm. Field sizes and depths are in cm.

Field Size	S_c	S_p	$S_c \cdot S_p$
4x4	0.966	0.873	0.843
5x5	0.974	0.907	0.883
6x6	0.982	0.930	0.913
8x8	0.990	0.971	0.961
10x10	1.000	1.000	1.000
12x12	1.006	1.027	1.033
15x15	1.011	1.066	1.078
18x18	1.015	1.094	1.111
20x20	1.018	1.106	1.126
25x25	1.023	1.134	1.160
30x30	1.031	1.159	1.195
35x35	1.037	1.177	1.221
40x40	1.041	1.188	1.237

3.2.1.2 Geometry for Cell Irradiations

The geometry for 4 MV cell irradiations has been described by Dugas *et al.* (2011). Flat bottomed 25 cm^2 cell culture flasks (MIDSCI, Valley Park, MO) were placed on top of a slab of Solid Water® (to provide sufficient backscatter) 5 cm thick and irradiated at a source-to-surface distance (SSD) of 150 cm with respect to the base of the flask with a 45 x 45 cm^2 field size (30 x 30 cm^2 at isocenter), at a depth of 0.5 cm in medium (Figure 3.1). The large field size was chosen to accommodate the irradiating of up to four flasks at once, and the extended SSD was chosen so that the dose rate was similar to that used for the previous study of CHO cells (≈ 0.24 $Gy*min^{-1}$).

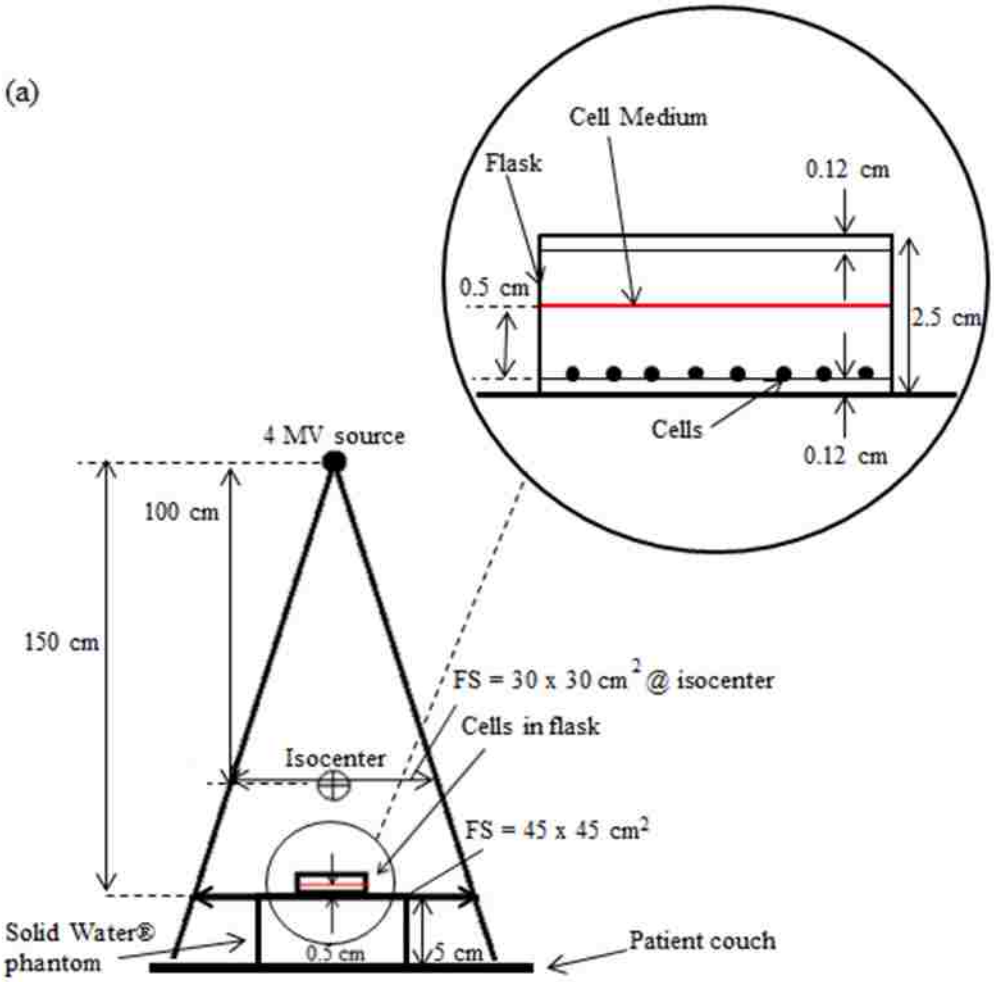

Figure 3.1: Geometry for 4 MV cell irradiations. (a) Schematic of setup (side view) and (b) photo of cell flasks resting on top of a 5 cm thick Solid Water® phantom.

The dose output at the linac's calibration point (10 x 10 cm^2 field size and 10 cm depth at isocenter) was 0.758 cGy per monitor unit (MU) for water, and the machine dose rate (dose output per unit time) of 250 MU*min^{-1} at isocenter (10 x 10 cm^2 field) resulted in a dose rate of 1.2 Gy*min^{-1}.

3.2.1.3 Determination of Cell Dose

Dose delivered to the cells were determined by:

$$D = D' * MU * f_{cal}, \tag{3.1}$$

where D is dose delivered, D' is the dose per MU, and MU is monitor units. f_{cal} is the ratio of the dose output in water for calibration conditions measured for the month when cells were irradiated to the standard value. D' was derived (see Appendix A) as:

$$D' = D'_o * S_c(r_c) * S_p(r_c) * TPR(r_c, d_m) * \frac{PSF(r)}{PSF(r_{dm})} * ISF * \frac{TPR(r,\ d)}{TPR(r, d_m)}, \tag{3.2}$$

where D_o' = Standard dose output in water for calibration conditions,

r_c = Collimator field size (isocenter),

$S_c(r_c)$*$S_p(r_c)$ = Output factors (scatter collimator factor and scatter phantom factor),

r = Effective field size at cell irradiation SPD,

d = Cell irradiation depth,

d_m = Depth of maximum dose for 4 MV in water,

$PSF(FS)$ = Peak scatter factor (PSF) at a certain field size,

ISF = Inverse square factor = $(SPD_o * SPD^{-1})^2$,

where SPD = Source to point of calculation distance (source to surface of cells),

SPD_o = Calibration distance (source to isocenter distance),

TPR(depth, FS) = Tissue-phantom ratio for a certain depth and field size.

Table 3.2 shows the values used for each parameter in Equation (3.2), where D' = 0.486 cGy*MU^{-1}. MU is a measure of beam output of a linac, in which 1 MU corresponds to a set amount of charge in a transmission ion chamber, which has been amplified to correspond to a particular dose. Linacs are calibrated to give a particular absorbed dose under specific conditions (i.e., a machine can be calibrated to deliver 1 Gy per 100 MU for a certain depth, field size and SSD), where the dose output is calibrated using TG-51 protocol (Almond *et al.* 1999). An initial amount of MUs were estimated using standard monitor unit calculations (Khan 2010) for the prescribed doses of 0 cGy, 200 cGy, 400 cGy, 600 cGy, 800 cGy, 1000 cGy, and 1200 cGy. The actual dose delivered to the cells was then calculated using Equation (3.2).

Each time a 4 MV cell irradiation was done, f_{cal} (i.e., the ratio of the measured dose output to standard dose output for a given monthly output QA) of the machine was recorded from the official data log book kept at the clinic, which is verified and updated on a monthly basis (see Section 3.2.1.1). The purpose of the monthly measurement was to verify that the

Table 3.2: Parameter values for Equation (3.2).

Parameters in Equation (3.2)	Values
$D_o'(d_o, FS = 10 \times 10\ cm^2, SSD_o)$	0.758 cGy*MU^{-1} (dose to water)
r_c	30 x 30 cm^2
$S_c(r_c)*S_p(r_c)$	1.195 (from Table 3.1(b))
d_m	1.2 cm
d	0.62 cm [(0.5 + 0.12)cm]
r	44.96 x 44.96 cm^2 [45 cm*(149.88/150)]
r_{dm}	29.6 x 29.6 cm^2 [30 cm*(98.8/100)]
$TPR(r_c, d_m)$	1.248 (interpolated from Table 3.1(a))
$TPR(r, d)$	1.152 (interpolated from Table 3.1(a))
$TPR(r, d_m)$	1.205 (interpolated from Table 3.1(a))
$PSF(r)*[PSF(r_{dm})]^{-1}$	1.010 (interpolated from Aird *et al.* 1996)
SPD	149.88 cm [(150-0.12)cm]
SSD_o	100 cm (isocenter)
ISF	0.4452
D'	**0.486 cGy*MU^{-1}**

calibrated dose output was within the clinic's tolerance of ± 2% of the commissioned value. f_{cal}, obtained from the clinic's logbook, was included in Equation (3.1) to account for monthly output fluctuations, which are within the ± 2% tolerance of the standard dose output in water for calibration conditions (see Table 3.3 for f_{cal} values for all 4 MV cell irradiations).

Table 3.3: Values of f_{cal} for 4 MV cell irradiations.

Logbook (i.e., Monthly Measurement) Date	f_{cal}	Irradiation Date	Data Set	% IUdR
06/20/10	1.001	07/07/10	(001)	0
07/16/10	0.995	07/22/10	(003)	0
07/16/10	0.995	08/25/10	(005)	0
10/27/10	1.007	11/04/10	(010)	0
10/27/10	1.007	11/11/10	(011)	0
01/19/11	1.001	02/09/11	(015)	9
01/19/11	1.001	02/16/11	(016)	0
03/16/11	0.994	04/14/11	(022)	0, 9, 18
04/25/11	1.003	05/11/11	(024)	0, 18
05/20/11	1.011	06/15/11	(027A)	0
05/20/11	1.011	06/16/11	(027B)	0, 18
06/20/11	1.011	06/30/11	(030)	0, 18
06/20/11	1.011	07/07/11	(031)	0, 18
06/20/11	1.011	07/14/11	(032)	0, 9
09/20/11	1.008	09/23/11	(043QA)	0
01/23/12	1.008	01/23/12	(061QA)	0
01/23/12	1.008	02/09/12	(065QA)	18
07/20/12	0.996	07/19/12	(072QA)	0, 18

3.2.1.4 Film Verification of Cell Dose

Radiochromic film was chosen for this project because of its inherent ease in irradiation and analysis. Gafchromic® EBT film (ISP, Wayne, NJ) was obtained from lot #48022-05. To verify the dose delivered to cells, 3 x 6 cm^2 pieces of EBT film were placed at the inner bottom of the 25 cm^2 flasks (location of growth surface area for cells) with a 0.5 cm thick layer of Super Flab® over the film to simulate the medium that overlay the cells. Then, the flask with film was placed in the field along with three cell-bearing flasks.

Following film exposures, film doses were determined using the mean pixel value of a region of interest (~1.0 x 1.0 cm^2) located at the center of the film (film readout and analysis protocol was discussed in Brown *et al.* (2012a) and summarized in Appendix C). The mean pixel value, which was proportional to the mean dose delivered to the cell flask, was then converted to net optical density (NOD). The NOD was converted to dose using the calibration curve described in Brown *et al.* (2012a) (see Appendix C). This mean dose was then compared to the calculated dose. This verification process was performed for two separate days of the 18 days in which 4 MV cell irradiations were performed.

3.2.2 Monochromatic keV X-Ray Irradiations

3.2.2.1 Production of Monochromatic X-Rays (25-35 KeV)

Monochromatic x-rays were produced by a synchrotron (LSU Center for Advanced Microstructures and Devices (CAMD)). CAMD uses an electron storage ring to produce broad spectrum electromagnetic radiation. A linac injects 200 MeV electrons into the synchrotron ring, which are then accelerated to 1.3 GeV. The target value for ring current after injection is 200 mA. Synchrotron radiation is emitted when charged particles are accelerated at relativistic speeds. The ring's bending magnets produce light from UV wavelengths to x-rays of about 1 keV energy (http://www.camd.lsu.edu/).

Producing higher energy x-rays requires stronger acceleration of the electron beam. This is achieved with an "insertion device" that laterally accelerates the electrons, oscillating them through sharp bends in the plane of the ring. These insertion devices are often called "wigglers" because of the motion of the electron beam. Insertion devices are located on straight sections of the storage ring, between the bending magnets. The current insertion device, a wavelength shifter (WLS), at CAMD consists of a 3-pole superconducting magnet with a maximum field of 7 T at

the central pole and 1.55 T at the side poles (see Figure 3.2(b)). This insertion device produces x-rays up to a few tens of keV. The broadband synchrotron radiation travels in the direction of the axis of the WLS (tangential to the ring) and feeds into the experimental beamlines (Figure 3.2(a)). One of four beamlines fed by the WLS is the tomography beamline (from herein referred to as the radiobiological beamline) (see Figure 3.2(c)).

A monochromator is used in the beamline to select a particular narrow x-ray energy beam (see Figure 3.2(d)). X-rays refract from the crystal structure of the monochromator, transmitting only those x-rays with a wavelength satisfying Bragg's Law ($n*\lambda=2*d*sin\theta$). The crystal spacing (d) and the Bragg scattering angle (θ), (how much the monochromator crystal must be tilted relative to the photon beam) determines the selected a specific energy. The crystal spacing also determines the bandwidth (degree of monochromaticity) of the selected energy. The current monochromator (Oxford, Danfysik, UK) in the radiobiological beamline is a double-crystal, multi-layer (W-B_4C) monochromator, used in a grazing incidence geometry. The monochromator can transmit 6-35 keV x-rays with a bandwidth of 1-3%. The beam must hit at a very shallow grazing angle to produce the higher energies so that small changes in the crystal tilt (i.e., incidence angle) produce big changes to the energy. The second crystal redirects the monochromatic beam to a path parallel to the original white light. Monochromatic photons enter the experimental area (i.e., hutch) through a Kapton® window and pass through tungsten collimators to shape the beam.

In the present study, monochromatic x-ray beams of 25 keV, 30 keV and 35 keV were used. The beam energy was set through calibrations of the monochromator, which were done using a K-edge absorption technique where the beam intensity was measured after passing through a known target material as a function of monochromator setting. The sharp

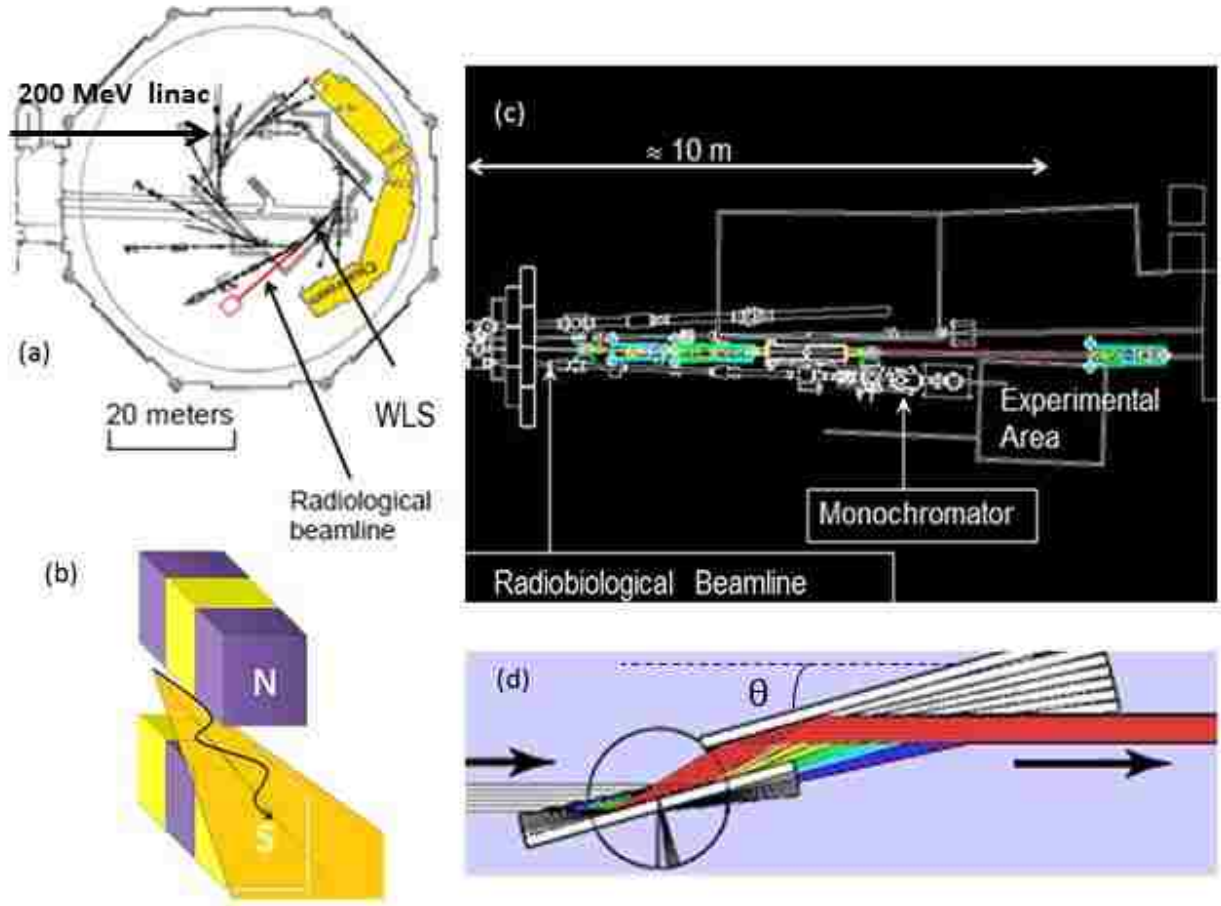

Figure 3.2: Production of monochromatic x-rays for radiobiological beamline at CAMD. (a) Schematic overhead view of CAMD synchrotron and beamlines. (b) Illustration of photons traversing a 3-pole WLS. (c) Expanded view showing the radiobiological beamline utilized in this project. (d) Simple schematic of incident white light selecting a small bandwidth of the light after traversing a double-crystal, multi-layer monochromator.

discontinuities in absorption as the monochromator passed through the K-edge energy identifies the monochromator setting for that energy. By sweeping across a range of beam energies for a series of materials with different well-known K-edge energies (i.e., 25.5 keV for Ag, 29.2 keV for Sn, etc.), the monochromator was calibrated (Oves 2008).

The WLS and monochromator limited the range of energy this project could study. As can be seen in Figure 3.3, the dose rate decreased rapidly as the energy increased. At about 40 keV, the dose rate dropped down to 0.1 Gy*min^{-1} at 100 mA. At energies > 40 keV, the dose rate would be too low for cell irradiations to be feasible.

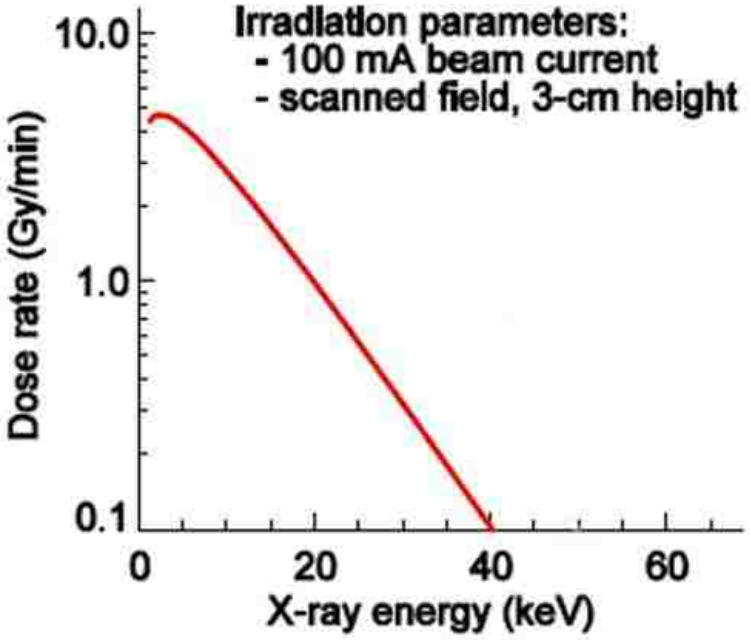

Figure 3.3: Estimated dose rate at 100 mA based on measured dose rate and calculated beam fluence as a function of energy (private communication with Kenneth L. Matthews).

3.2.2.2 Time Variation of Beam Current

As part of normal operations at CAMD, the number of electrons cycling the storage ring decreases exponentially with time after initial injection. Therefore, the photon intensity produced by these electrons passing through the wiggler simultaneously decreases. As a result of the decreasing fluence from the decaying storage ring current of the beam, the dose rate was dependent on the beam current at the time of measurement. To compensate, beam current was recorded at each measurement. Figure 3.4(a) shows a typical plot of ring current decaying as a function of time over one day at CAMD. Usually, electron injection occurred around 8:15 AM; a beam dump and re-injection occurred around 2:30 PM. At the beginning of a completed injection, the current was ≤ 200 mA. Re-injection was done to keep the beam current from getting too low (below ~80 mA). Figure 3.4(b) shows an example of a day with three electron injections (one morning injection followed by two afternoon re-injections).

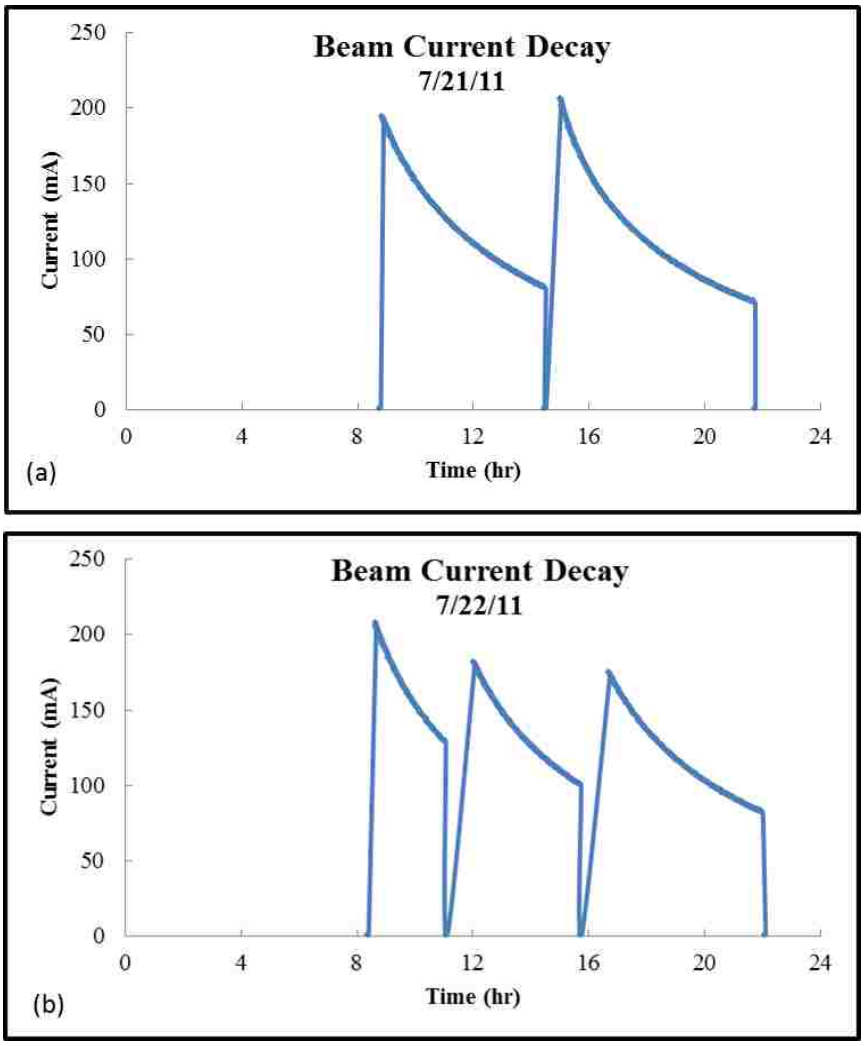

Figure 3.4: Beam current decay at CAMD. (a) Typical day with a morning electron injection followed by one in the afternoon. (b) A day with three injections (data provided by CAMD staff Paul D. Jines).

3.2.2.3 Energy Verification

Prior to dose measurements and cell irradiations, the energy of the beam was verified using a powder diffraction measurement (described in Oves (2008) and Dugas *et al.* (2008)). The beam, which was horizontally collimated using tungsten plates to approximately 0.2 × 0.1 cm^2, was incident upon a Si640c powder sample (0.8 cm in diameter) contained within a 45° cone milled into a 3 mm thick polymethylmethacrylate (PMMA) holder. The sample was aligned at beam height, perpendicular to the incident beam. Photons passing through the Si640c sample

were diffracted according to Bragg's Law, producing concentric Debye-Scherrer rings (see Figure 3.5). A flat panel XRD 0820 CN3 amorphous silicon detector (Perkin-Elmer, Waltham, MA) was used to capture the Debye-Scherrer rings. Each measurement required an exposure time of 2 s and allowed determination of the energy to within ± 0.1 keV (Brown *et al.* 2012b).

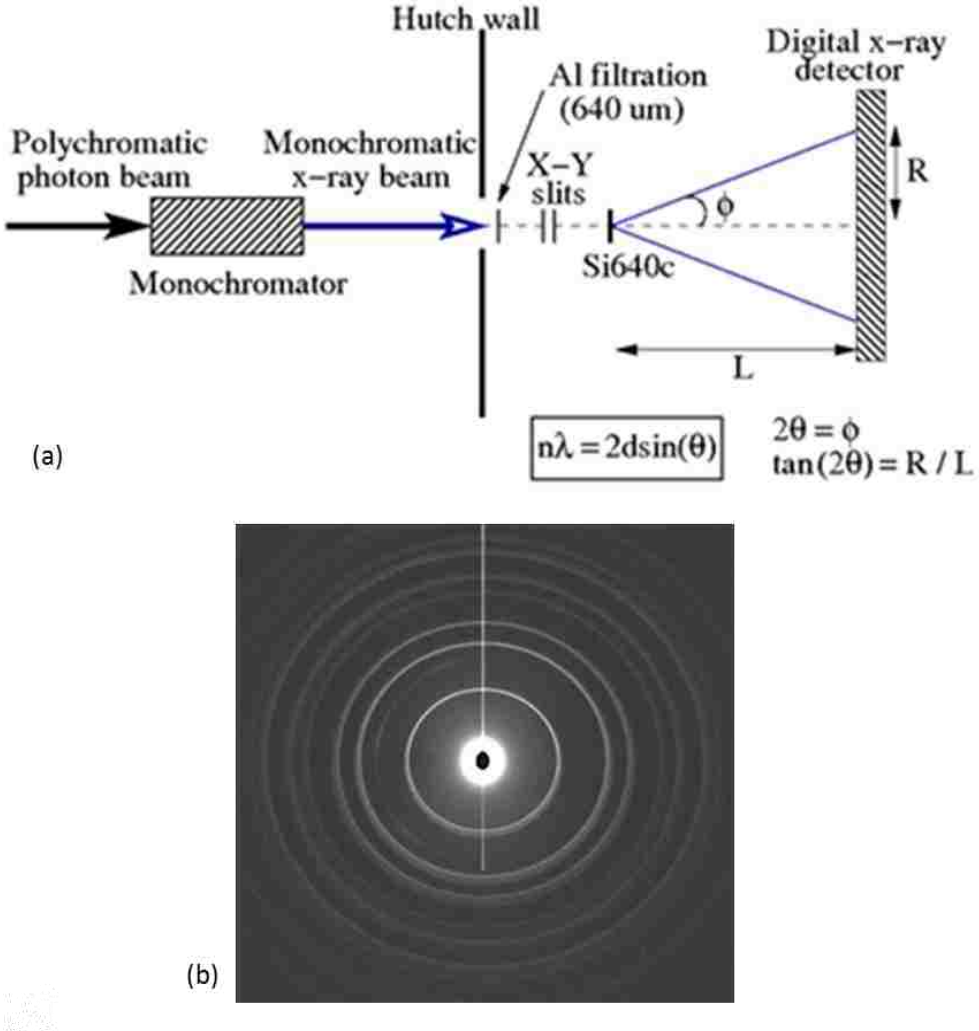

Figure 3.5: Schematic for energy determination. (a) Schematic showing the incident monochromatic, "point" beam being diffracted by Si640c crystal powder producing Debye-Scherrer diffraction cones (courtesy of Dr. Thomas A.D. Brown). (b) Typical image of Debye-Scherrer diffraction rings intersecting and being recorded by the flat panel, digital x-ray detector. X-ray wavelength, determined by the cone angle [$n*\lambda = 2*d*sin(0.5*arctan(R/L))$] allow determination of energy ($E=h*c/\lambda$).

3.2.2.4 Production of Broad Beam Monochromatic X-Rays

Due to physical restrictions imposed by synchrotron emission, the monochromator, and the beamline slits, the monochromatic beam in the hutch measured approximately 3.0 cm horizontally (plane of synchrotron ring) by 0.1 cm vertically. This "strip" beam was filtered using 640 μm aluminum to remove low-energy x-ray contamination (see Figure 3.6). An

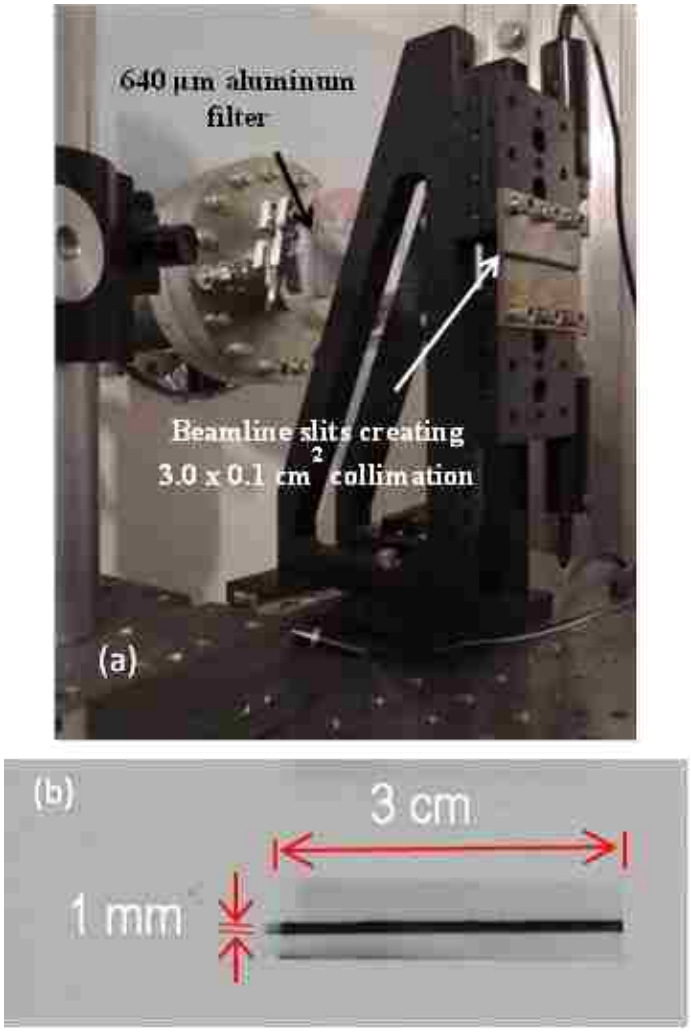

Figure 3.6: Synchrotron "strip" x-ray beam. (a) Monochromatic beam filtered by aluminum foil (640 μm thick) and collimated with tungsten beamline slits to 3.0 x 0.1 cm^2 dimensions. (b) Resulting monochromatic x-ray beam on radiochromic film (Gafchromic® EBT).

effective broad beam approximately 3.0 x 2.5 cm^2 was achieved by vertically oscillating the irradiation target through a triangular waveform through the path of the narrow beam to uniformly distribute dose to the cells (see Figure 3.7). A screw-drive motion stage (Velmex, Inc., Bloomfield, NY) controlled by an in-house LabVIEW (National Instruments Corporation, Austin, TX) interface was used to achieve the target oscillation (Dugas *et al.* 2008, Oves *et al.*

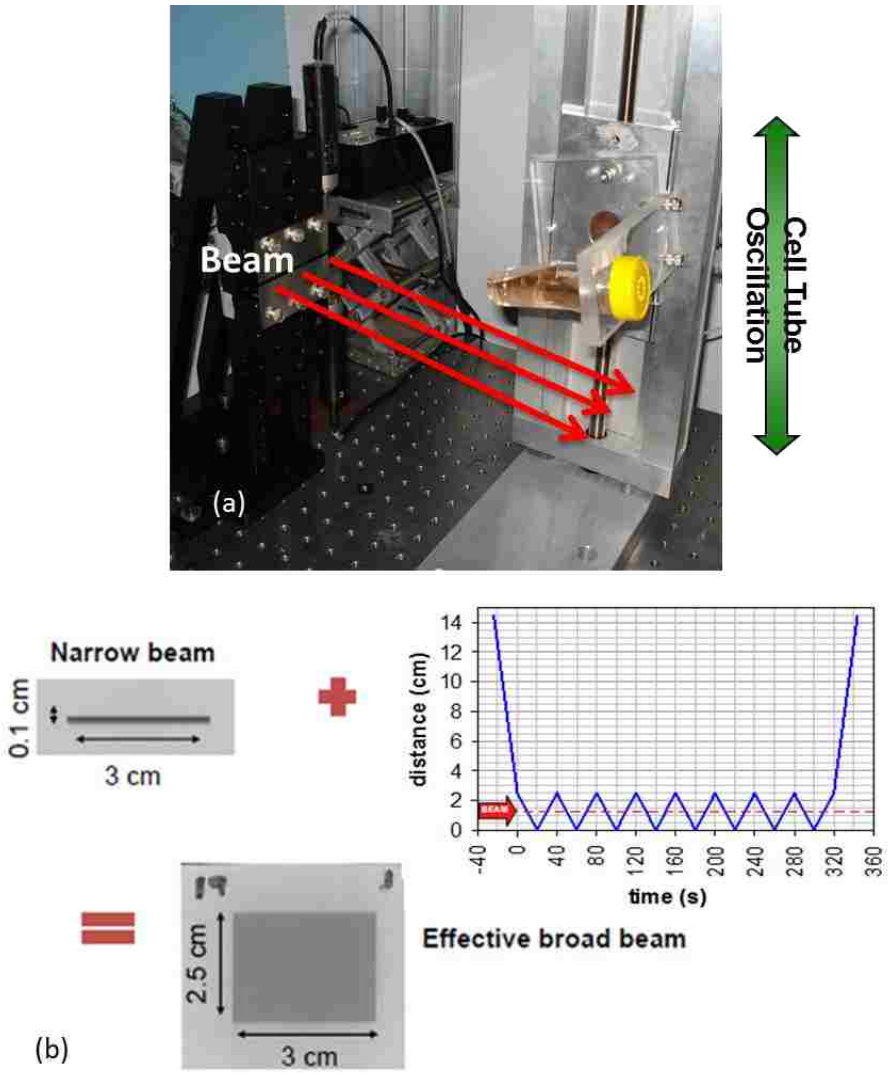

Figure 3.7: Broad beam production. (a) A screw-drive motion stage, with a cell culture test tube attached, oscillates through the monochromatic x-ray beam producing a broad beam in the reference frame of the cell culture test tube. (b) An effective broad beam approximately 3.0 x 2.5 cm^2 was achieved by vertically oscillating the stage through the path of the "strip" beam at 0.125 $cm*s^{-1}$ using a triangular function (courtesy of Dr. Joseph Dugas).

2008). Previous measurements showed that the effective broad beam can be considered a parallel beam (Dugas *et al.* 2008).

3.2.2.5 Geometry for Cell Irradiations

Cell culture test tubes (3 cm wide x 10 cm long) were filled with ~35 mL of medium and attached to the motion stage using a PMMA holder. The holder was oriented (17^{o} from horizontal) so that the cell growing surface, located on the inner flat side of the tube, was at an angle of 26^{o} to the incident beam for uniform dose coverage (see Figure 3.8). Upon activating the scanning operation, the motion stage moved rapidly downward until the beam was incident on the bottom edge of the tube. At this point, the stage slowly moved (0.125 $cm*s^{-1}$) downward through the 2.5 cm amplitude of the beam and then upward 2.5 cm in multiple stage oscillations (one oscillation = ± 2.5 cm), sweeping the tube and uniformly irradiating the growing surface

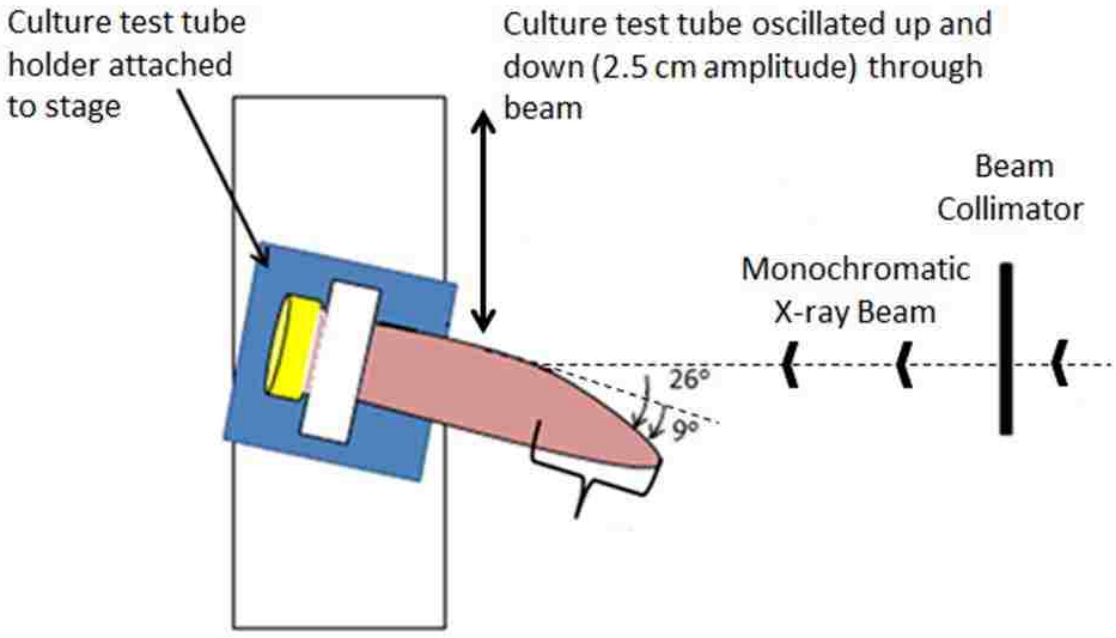

Figure 3.8: Geometry of monochromatic x-ray cell irradiations. Schematic showing relationship between oscillating stage, cell culture test tube mount, cell culture test tube, and horizontal beam slit.

completely (described in Dugas *et al.* 2011). The speed of the movement was set sufficiently low to minimize the change in exposure time due to the change in acceleration at the stage's lowest and highest position. The transit time of a complete stage oscillation (i.e., one stage cycle) was 40 s. The number of cycles was rounded to the nearest whole number that would approximately achieve the prescribed dose. Upon completion, the stage rapidly moved upward and out of the beam to its original position.

3.2.2.6 Determination of Cell Dose

Two independent methods were utilized to determine the monochromatic x-ray beam dose delivered to the cells, ion chamber and radiochromic film dosimetry. The former was used to determine the cell irradiation times at the beginning of an experiment. Because this was often shortly after beam injection, it is believed that the dose rate ($Gy*min^{-1}$ per 100 mA) settled to a different value. Hence, radiochromic film dosimetry, typically done just before irradiating multiple cell culture test tubes, was used as the primary measured cell dose.

3.2.2.6.1 Ion Chamber Dosimetry

The first step to determine the doses delivered to the cell cultures was to take ion chamber measurements at a depth of 0.58 cm in a PMMA phantom to estimate the dose rate at 100 mA (see Figure 3.9). The estimated dose rate was used to determine the required number of cycles for each cell irradiation. Three measurements were taken, each lasting 320 s, corresponding to eight cycles. Using the average ring current for each irradiation, the measured ionization was normalized to a ring current of 100 mA, converted to a dose using AAPM TG-61 (Ma *et al.* 2001) protocol as described below, and then divided by 320 s to get a normalized dose rate. The average dose rates at 100 mA were 0.2 $Gy*min^{-1}$ at 35 keV, 0.8 $Gy*min^{-1}$ at 30 keV, and 1.5 $Gy*min^{-1}$ at 25 keV.

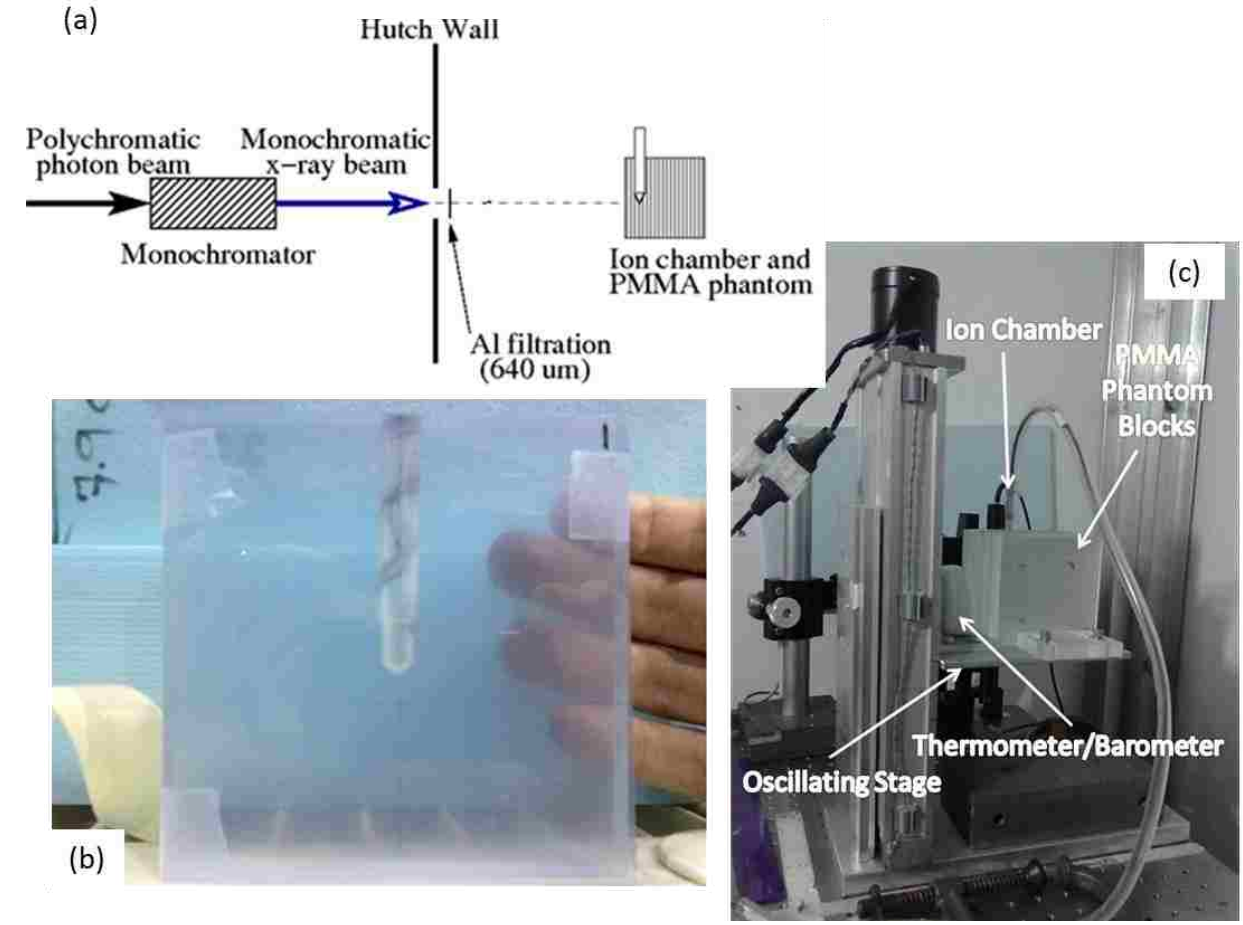

Figure 3.9: Ion chamber measurements. (a) Schematic showing dose calibration beam geometry (courtesy of Dr. Thomas A.D. Brown). (b) Phantom slab that contains insertion for ion chamber. (c) Dose calibration measurement setup.

The TG-61 protocol for determining dose to water (D_w) for medium-energy x-rays (100-300 kV) at a depth of 2 cm, was applied to convert the ion chamber readings (normalized to 100 mA) into dose:

$$D_w = M_{norm} * P_{elec} * P_{TP} * P_{ion} * P_{pol} * P_{Q,cham} * N_k * \left(\frac{\mu_{en}}{\rho}\right)_{AIR}^{WATER}, \qquad (3.3)$$

where:

M_{norm} = Electrometer reading (C),

P_{elec} = Electrometer calibration factor,

P_{TP} = Ambient temperature and pressure correction factor (corrected to T = 22^{o}C, P = 101.33 kPa),

P_{ion} = Ion recombination correction factor,

P_{pol} = Polarity effect correction factor,

N_k = Air-kerma calibration factor (Gy*C^{-1}) of the 0.23 cm^3, air-equivalent cylindrical ion chamber (Scanditronix Wellhofer GmbH model FC23-C, Schwarzenbruck, Germany),

$P_{Q,\ cham}$ = Overall correction factor to account for the effects due to the change in beam quality between calibration and measurement and to the perturbation of the photon fluence at the point of measurement by the chamber,

$\left(\frac{\mu_{en}}{\rho}\right)_{AIR}^{WATER}$ = Ratio of the water-to-air mass-energy absorption coefficients.

Because the studied energies (25-35 keV) were at or slightly below the range specified for the TG-61 protocol (the effective energy of 100 kV is approximately 33 keV), its use was validated by Brown *et al.* (2012b) performing fluence measurements (see Appendix C).

The factors in Equation (3.3) were obtained in the same manner as described in Brown *et al.* (2012b), and are listed for all energies studied in Table 3.4. P_{elec} was determined by an Accredited Dosimetry Calibration Laboratory (ADCL). The temperature and pressure were recorded before and after each ion chamber measurement using a NIST-traceable digital thermometer/barometer placed on the oscillating stage and averaged for each measurement. P_{TP} was determined by:

$$P_{TP} = \frac{273.2 + T[℃]}{295.2} * \frac{101.33}{P[kPa]}. \quad (3.4)$$

where:

T = Temperature (°C),

P = Absolute Pressure (kPa).

Table 3.4: TG-61 ion chamber calibration and correction factors for dose calculations using Equation (3.3) at 25, 30, and 35 keV (Brown *et. al* 2012b). Measurements of P_{TP}, P_{ion}, and P_{pol} were repeated for each set of depth-dose measurements, and the range of values obtained are shown here (only one set of P_{ion} and P_{pol} measurements were made at 30 keV).

P_{elec}	0.987	0.987	0.987
P_{TP}	1.000–1.021	1.001–1.002	1.003–1.011
P_{ion}	1.000–1.002	1.000	1.000–1.008
P_{pol}	0.994–0.999	0.995	0.990–1.003
$P_{Q,cham}$	1.000	1.000	1.000
N_k	1.221×10^8 Gy C^{-1}	1.220×10^8 Gy C^{-1}	1.219×10^8 Gy C^{-1}
$\left(\frac{\mu_{en}}{\rho}\right)_{AIR}^{WATER}$	1.019	1.013	1.015

The ion chamber measurements used to calculate P_{ion} and P_{pol} were conducted at a PMMA depth of 0.58 cm. The application of the TG-61 protocol to determine the ion chamber depth-dose curve was validated by intercomparison with MCNP5 Monte Carlo calculations of dose per fluence and measured fluence at beam energies of 25 and 35 keV as done by Oves *et al*. (2008) and briefly discussed in Appendix C.

Ion chamber readings (M_{raw}) for P_{ion} and P_{pol} lasted 160 s (i.e., four cycles) and were normalized to a ring current of 100 mA. P_{ion} was determined for the case of a continuous beam using high and low electrometer bias voltages of -300 V (V_H) and -150 V (V_L) , respectively (see Equation (3.5) below). P_{pol} was determined for the case of electrometer bias voltages of +300 V (M^+_{raw}) and -300 V (M^-_{raw}):

$$P_{ion} = \frac{1 - \left(\frac{V_H}{V_L}\right)^2}{\frac{M^H_{raw}}{M^L_{raw}} - \left(\frac{V_H}{V_L}\right)^2}, \tag{3.5}$$

$$P_{pol} = \left| \frac{M_{raw}^{+} - M_{raw}^{-}}{2 * M_{raw}} \right|. \quad (3.6)$$

Values for $P_{Q,cham}$ were difficult to determine because the energies and field size used for these measurements lay outside the range of data available for this correction factor in TG-61. Estimates of $P_{Q,cham}$ were obtained by using $P_{Q,cham}$ = 0.995 for the similar NE2611/NE2561 ion chambers and for a 0.1 mm Cu half-value layer (HVL) beam (equivalent monochromatic beam = 33 keV) in TG-61 Table VIII, and then applying a field size correction factor of 1.005 by extrapolating data in TG-61 Figure 4 for the broad beam size (7.5 cm^2) used. N_k was determined using a linear fit to ADCL-calibrated values measured for a 120 kVp beam (HVL = 6.96 mm Al) and an 80 kVp beam (HVL = 2.96 mm Al), which were $1.215*10^8$ $Gy*C^{-1}$ and $1.219*10^8$ $Gy*C^{-1}$, respectively. The HVL values were used to interpolate or extrapolate N_k values at 35 keV (HVL = 3.33 mm Al), 30 keV (HVL = 2.28 mm Al), and 25 keV (HVL = 1.12 mm Al). Mass-energy absorption coefficients for water and air were interpolated for each energy using NIST tables (Hubbell & Seltzer 2004) and used to calculate values for $\left(\frac{\mu_{en}}{\rho}\right)_{AIR}^{WATER}$.

Ion chamber dose rates were considered an estimate for two reasons: (1) differences in depth of measurement and (2) attenuation due to different materials. During ion chamber readings, the ionization was collected at a depth of 0.58 cm through PMMA, whereas cell dose was delivered at a depth of 0.31 cm in polystyrene:

$$\frac{Thickness\ of\ Cell\ Culture\ Test\ Tube\ Wall + (0.5 * Film\ Thickness)}{\sin 26^o} = \frac{0.12\ cm + (0.5 * 0.028\ cm)}{\sin 26^o} = 0.31\ cm. \quad (3.7)$$

Oves *et al.* (2008) reported that at depths of less than 1.5 cm in the PMMA phantom, the depth dose curve may be > 3.0% from the Monte Carlo MCNP5 curve, thus making it necessary to

measure the dose rate for each electron injection of the beam. Despite the measurement difference with respect to the in-phantom depth of 0.58 cm and TG-61's reference depth of 2 cm, the dose rate estimate was acceptable for the purpose of determining the number of stage cycles necessary for cell irradiations.

The ion chamber depth-dose measurements in PMMA were compared with MCNP5 Monte Carlo calculations of dose per fluence and measured incident fluence to verify the validity of using TG-61 ion chamber dosimetry to calibrate dose output (dose per unit time per 100 mA) for cell irradiations, as described in Brown *et al.* (2012b). The methods are briefly described in Appendix C. Results showed that TG-61 ion chamber dosimetry agreed with fluence-normalized MCNP5 calculations to within 7% at 25 keV and 3% at 35 keV.

3.2.2.6.2 Radiochromic Film Dosimetry

Gafchromic® EBT2 film (ISP, Wayne, NJ) obtained from lot # A02181103 (EBT2) was used for monochromatic x-ray film dosimetry. After the dose rate per 100 mA was estimated and before a set of cell irradiations, two pieces of film were irradiated to later determine more accurately the dose to the cells. A 1.5 x 3.0 cm^2 piece of film was taped to the cell growing surface inside a cell culture test tube which was then filled with water to simulate the effect of the medium (Figure 3.10). The tube was then irradiated with the number of stage cycles required to acquire ~2 Gy dose. The amount of time taken to deliver this dose and the ring current during this time interval were recorded. This measurement was repeated with a second piece of film. It was assumed that the average dose delivered to these pieces of film more closely represented the actual dose rate during a cell irradiation than did the ion chamber measurement, and hence was used to determine the dose delivered to the cells. These film irradiations were repeated for each storage ring injection period.

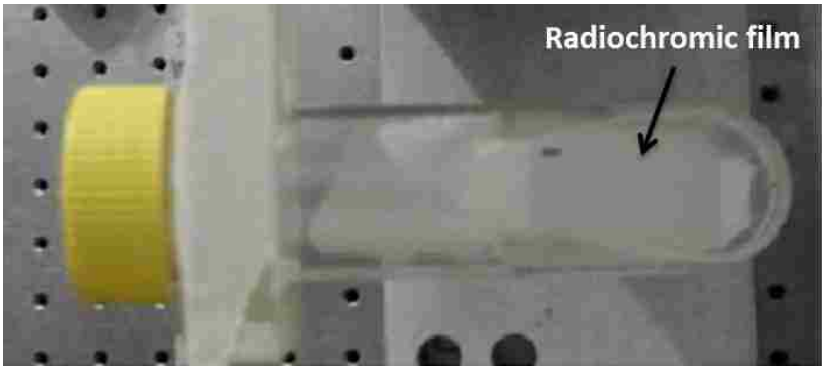

Figure 3.10: Bird's-eye-view of radiochromic film attached to cell culture test tube. The film was attached to the inside wall of a cell culture test tube, where cells would attach and grow.

Next, the pieces of film were scanned and analyzed by a medical physicist at least 24 hours after the irradiations in the manner described in Brown *et al.* (2012a) (see Appendix C). Briefly, the mean pixel value of an approximately 0.5 x 0.5 cm^2 region of interest located in the center of the film was determined for each piece of film and converted to NOD. Using the calibration curve at that particular monochromatic energy, the dose to each piece of film was determined and then normalized to 100 mA using the average ring current during each film's irradiation. Each film's dose at 100 mA was then divided by the amount of time it took to irradiate it to compute the dose rate at 100 mA. The two dose rates were averaged and the average dose rate ($Gy*min^{-1}$) at 100 mA was used to calculate dose to each cell culture test tube. Because the film was placed inside the test tube where the cells would normally be located, no correction due to the attenuation of polystyrene was applied to the dose rate calculation.

To calculate the total dose to each cell culture test tube, a summation of the dose per five-minute interval was calculated to account for the beam current decay. Each of these "interval doses" was calculated by multiplying the dose rate at 100 mA by the average ring current during the five-minute interval, dividing by 100 mA, and multiplying by the time interval (i.e., five minutes).

3.2.2.7 Comparison of Ion Chamber & Radiochromic Film Dosimetry

For each measurement session, film and ion chamber measurements were taken. Ideally, the two methods would agree within a few percent. Upon comparison, however, film and ion chamber measurements differed greatly (i.e., by as much as ~ 28% for 35 keV on average). It is believed that these discrepancies were due to the timing between the ion chamber and film measurements. To investigate this discrepancy, measurements were done to more closely compare the two dosimetry methods. Ion chamber measurements were made on four different days, approximately one hour after re-injection and followed by film irradiations. On a different day, ion chamber measurements were taken during the time interval 3-7 hours post-injection as a function of ring current in order to check the stability of the synchrotron beam.

The estimated cell dose rates calculated using the ion chamber ionization measurements in a PMMA phantom were compared to the film dose rate calculated from the pieces of film placed inside a test tube and irradiated to ~ 2 Gy (methods described in Section 3.2.2.6).

3.2.3 Cell Irradiations

Cells were irradiated by exposing the cell culture test tube to x-rays for the number of stage cycles determined from ion chamber measurements for the prescribed dose. The ring current was recorded at five-minute intervals during the irradiation. Although the beam current decayed exponentially over the course of the day, this was approximated as a linear decay during these short five-minute intervals.

3.2.3.1 Timeline for Production of a Cell Irradiation Data Set

Multiple steps were required to produce a cell irradiation data set and construct a survival curve. Table 3.5 outlines the steps and timing of each action performed. Cell preparations pre-irradiation and processing post-irradiation were performed in the tissue culture lab at PBRC. Key

steps were growing cells (Day 1), exposing cells to IUdR (Day 2), irradiating cells (Day 3), incubating cells (Days 3-12), and fixing/staining/counting cell colonies (Days 12-13).

Table 3.5: Timeline of steps/actions performed for each cell irradiation data set.

STEP	ACTION	TIMELINE
1	Plate Cells	Day 1
2	Expose Cells to IUdR	Day 2
3	Re-plate Cells	Day 3
4	Irradiate Cells	Day 3
5	Re-feed Cells	Day 3
6	Incubate Cells	Day 3
7	Re-feed Cells	Day 7
8	Fix & Stain Cell Colonies	Day 12
9	Count Colonies of Cells	Day 13

The standard protocol outlined in Hall and Giaccia (2006) to produce an *in vitro* cell survival curve was followed (see Figure 3.11). Cells from a stock culture were prepared on Day 1 into a single-cell suspension by trypsinization, and the cell concentration was counted using a hemocytometer (Hausser Scientific, Horsham, PA). Based on hemocytometer counts, approximately 2×10^4 cells were plated into each of three cell culture flasks (this number of cells were chosen so that, if the cells were to contain IUdR, the cell density was low enough to avoid overcrowding but large enough to have good statistics in the number of cells that took up the IUdR). These flasks were plated 12-24 hours before the addition of IUdR in order to allow cells to recover from the arrest caused by trypsinization.

On Day 2, if the cells were to contain IUdR, they were fed with 7 mL of medium containing either 1 μM or 3 μM of 5'-iodo-2'-deoxyuridine, i.e., IUdR (Sigma-Aldrich, St. Louis, MO). After 27 hours of incubation (Day 3), the cells were re-plated following the same process used on Day 1. For 4 MV irradiations, cells were cultured in 25 cm^2 (plating area) flasks

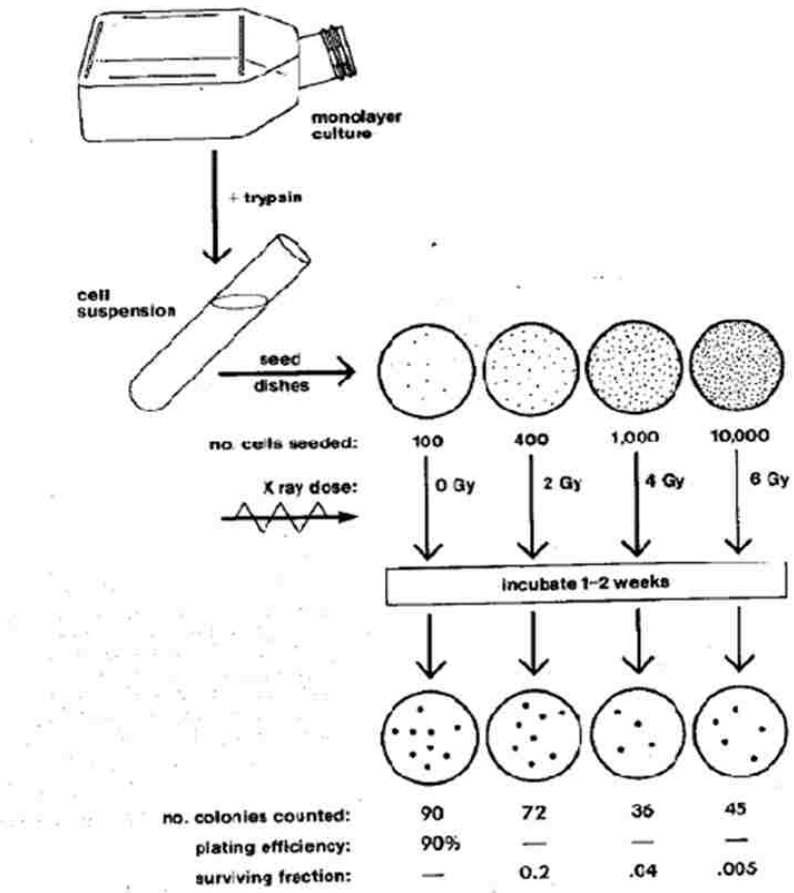

Figure 3.11: Cell culture technique used to measure an *in vitro* cell survival curve (Hall & Giaccia 2006).

while for 25-35 keV x-rays, cells were cultured in 10 cm^2 tube flasks. Known numbers of cells were plated into cell culture flasks. The number of cells plated per cell culture flask varied with dose so that ideally 30-60 cell colonies would survive. This amount of cell colonies should not overlap each other nor be too sparse to produce good statistics. Table 3.6 illustrates the cells plated and surviving cell colonies for a sample data set. The cells were incubated for 1.5-2 hours before transporting to the irradiation site to allow cells to attach to the surface of the cell culture flasks. Because irradiations took several hours at CAMD, irradiated cell culture test tubes were kept in an incubator on site except while being irradiated. After irradiation, the cells were transported back to PBRC where they were re-fed with fresh medium to eliminate radiation-induced oxygen species that were produced in the medium during irradiations.

Table 3.6: Number of cells plated per cell culture flask for data set (065). The number of cells plated varied with dose to ensure produce good statistics.

Prescribed Dose (Gy)	Estimated # Cells Plated	# Surviving Colonies
0	80	36
2	110	47
4	330	47
6	548	39
8	656	19
10	1193	14

During the nine days of incubation (Days 3-12), the cells were allowed to grow until they produced macroscopic colonies that can be seen by eye. To replenish nutrients, the cells were re-fed approximately midway through the incubation period (Day 4). On Day 12, colonies were fixed and stained with 2% W/V crystal violet and allowed to air-dry overnight. Figure 3.12 shows pictures of stained cells and cell colonies.

Cell colonies were counted on Day 13 with the aid of a light box, and if needed, a magnifier. Cell colonies of ~ 50 cells or more were scored as survivors. The counting of cell colonies can be subjective; however, so long as the counter is consistent with what he or she

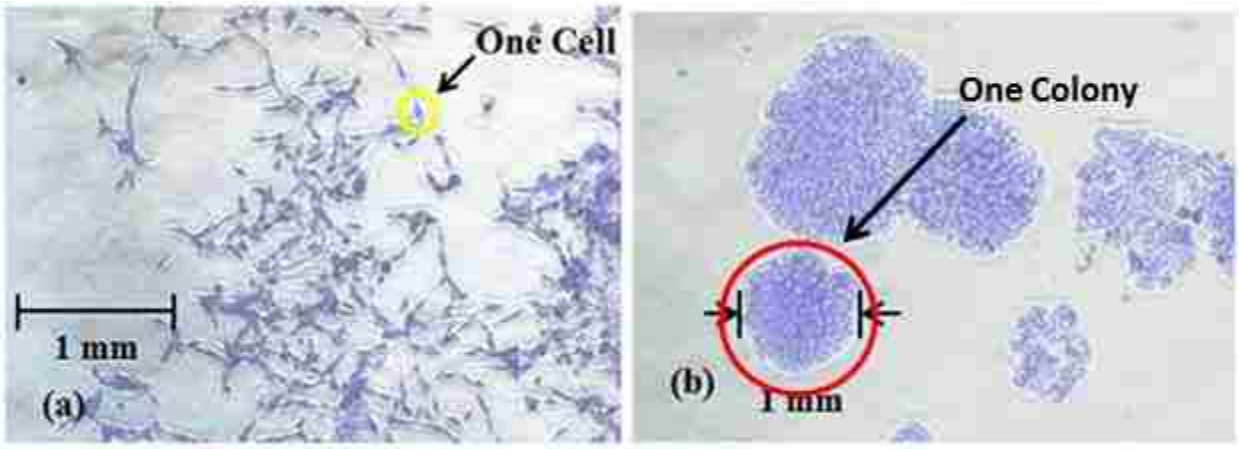

Figure 3.12: Rat 9L glioma cells after fixing and staining with crystal violet. (a) A 4 x 3 mm^2 picture of single cells. (b) A 4.75 x 3.75 mm^2 picture of cell colonies taken using a phase-contrast microscope at PBRC.

considers a surviving colony, the plating efficiency correction minimizes subjectivity. General criteria used to judge whether or not a cell colony was a survivor (personal communication with Dr. Marie Varnes) were:

1. Size: The most important factor considered was the size of the cell colony compared to others on the cell culture flask. Although most cell colonies that were visible to the naked eye were often counted as survivors, small, barely visible cell colonies were not considered survivors (see Figure 3.13).
2. Cell Density of Colony: If a cell colony was too sparse (i.e., a lot of space was visible between the stained cells), then the colony will most likely not continue to be clonogenic, thus, not be a survivor. Usually the crystal violet stain facilitated the interpretation of how dense the colony was (the relatively deeper the purple, the more cells were in the colony).
3. Well Defined Borders: Healthy colonies had well defined borders, while non-clonogenic cell colonies oftentimes had fuzzy borders with what appeared to be "fragments" and "giants" around the periphery. Giants are radiation-induced lethally damaged cells; giants are unable to divide, hence are not survivors (see Figure 3.14). Figure 3.13 and Figure 3.14 demonstrate several examples of cell colonies considered survivors and non-survivors.

For each data set, multiple cell culture flasks at a particular %IUdR were irradiated at different doses to create a survival curve. Each survival curve was repeated a minimum of three times on different days. Cell survival curves were determined at 6-7 dose levels between 0 and 12 Gy. Each dose point consisted of one irradiated flask of cells.

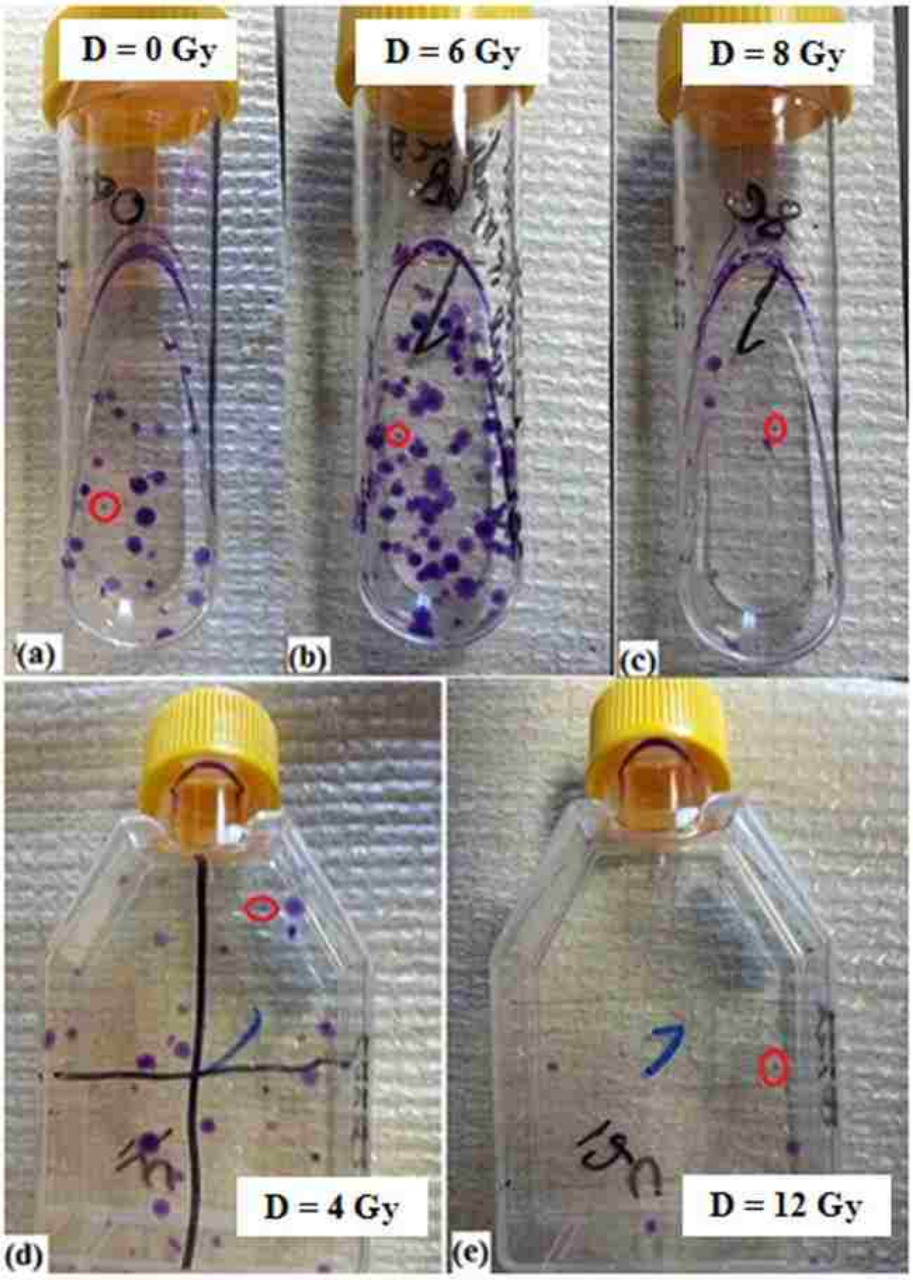

Figure 3.13: Cell culture test tubes and flasks with stained surviving colonies. A red circle around a cell colony denotes the borderline size considered a survivor. (a-c) 25-35 keV x-ray exposed cells and (d-e) 4 MV x-ray exposed cells.

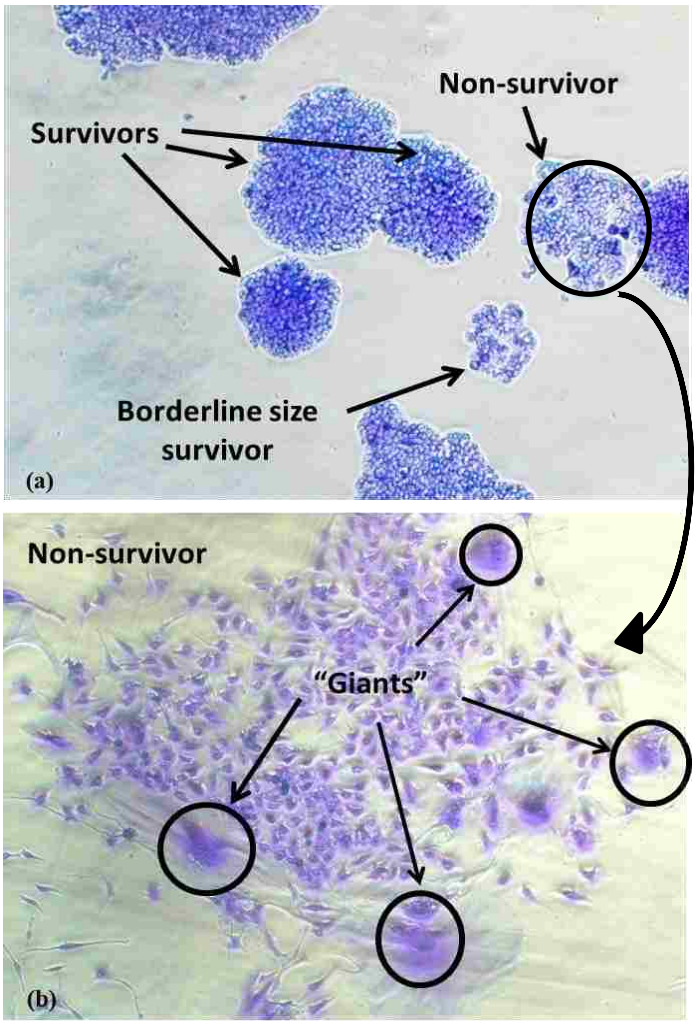

Figure 3.14: Examples of colonies that were survivors and non-survivors. (a) Surviving, non-surviving and borderline size surviving cell colonies, magnified by phase-contrast microscope. (b) Close-up of non-surviving colony. Note the "giants" (lethally radiation-damaged cells) around the periphery of the colony.

3.2.3.2 Determination of Survival Fractions (SF) & Uncertainties

A single data set (j) at one defined experimental condition (E, %IUdR) had N_j data points representing surviving fraction (SF_i) at each dose D_i. For a single data point "i" at D_i, the surviving fraction is given by:

$$SF_i(D_i) = \frac{N_{c,i}(D_i)/\overline{N}_{p,i}(D_i)}{PE}, \tag{3.8}$$

where:

$N_{c,i}(D_i)$ = Number of cell colonies counted for the i^{th} data point after exposure at dose D_i,

$\overline{N}_{p,i}(D_i)$ = Average number of cells plated for exposure at dose D_i,

PE = Plating efficiency.

Because the surviving fraction at $D = 0$ is unity, by definition, the plating efficiency theoretically is given by:

$$PE = \frac{\overline{N}_c(D = 0)}{\overline{N}_p(D = 0)}, \tag{3.9}$$

where $\overline{N}_c$ and $\overline{N}_p$ are the true mean values for the number of colonies counted and number of cells plated, respectively, at $D = 0$, which can only be estimated. The PE was determined as a free parameter in the curve-fitting process (see Section 4.2.2). Prior to the fit, Equation (3.9) was calculated using an initial estimate of PE given by:

$$PE_{est,init} = \frac{\sum_{\substack{i=1 \\ \ni D_i=0}}^{N_j} N_{c,i}(D_i = 0)/\overline{N}_{p,i}(D_i = 0)}{\sum_{\substack{i=1 \\ \ni D_i=0}}^{N_j} 1}. \tag{3.10}$$

The uncertainty in $SF_i(D_i)$ was estimated using Poisson statistics for the number of plated cells and the number of counted cells, i.e.,:

$$\sigma_{\overline{N}_{p,i}} = \sqrt{\overline{N}_{p,i}}, \tag{3.11}$$

and

$$\sigma_{N_{c,i}} = \sqrt{N_{c,i}}, \tag{3.12}$$

resulting in:

$$\sigma_{SF_i}^2 = \left(\frac{\partial SF_i}{\partial N_{c,i}}\right)^2 * \sigma_{N_{c,i}}^2 + \left(\frac{\partial SF_i}{\partial \bar{N}_{p,i}}\right)^2 * \sigma_{\bar{N}_{p,i}}^2, \tag{3.13}$$

$$= SF_i^2 \left[\frac{\sigma_{N_{c,i}}^2}{N_{c,i}^2} + \frac{\sigma_{\bar{N}_{p,i}}^2}{\bar{N}_{p,i}^2}\right], \tag{3.14}$$

or

$$\sigma_{SF_i} = SF_i \sqrt{\frac{1}{N_{c,i}} + \frac{1}{\bar{N}_{p,i}}}, \tag{3.15}$$

assuming $N_{c,i}$ and $\bar{N}_{p,i}$ are uncorrelated.

3.3 Results & Discussion

3.3.1 4 MV Film Verification of Dose

Doses calculated using Equation (3.1) were used as the doses received by the cells exposed to 4 MV x-rays. The doses were independently verified using radiochromic film on two exposure days. Table 3.7 compares the calculated doses used to determine cell doses, with those of two measured film doses. The percent differences (%) between film and calculated doses were determined, and the mean percent difference (± standard error) was 5.78 ± 0.58%.

Table 3.7: Percent differences (%) for MU dose calculations compared to measured film doses.

Date of Irradiation	MU	Calculated dose (cGy)	Film dose (cGy)	% diff
(MAY 28, 2010)	426	203.8	187.2	-8.16
	851	406.5	382.6	-5.90
	1277	610.3	585.7	-4.04
	1703	814.1	755.6	-7.19
(JULY 22, 2010)	426	203.0	188.9	-6.93
	851	404.9	389.0	-3.92
	1277	607.9	589.6	-3.00
	1703	810.8	762.6	-5.94
	2130	1014.8	944.8	-6.90
Average	-5.78			
Standard Error	0.58			

Why the film doses underestimated the calculated doses by 5.8% is not immediately apparent. The lack of phantom material lateral to the flasks could have a small but not likely significant impact to dose compared to 5.8%. Another possibility is that 0.62 cm depth is in the build-up region of central-axis depth dose. Another consideration is the erroneous assumption that non-uniform off-axis ratios near d_{max} were negligible. A fourth possibility is some unknown error in the film calibration.

A difference of this magnitude warrants further investigation. First, these measurements should be repeated, and if the difference remains, a third dosimeter, such as TLD-100 powder should be used as a second check. Second, a phantom housing the film with materials surrounding the flasks should be used so as to repeat the film measurement with a geometry more closely simulating that of the calculated.

Furthermore, future 4 MV cell exposures should be made at a depth just beyond d_{max} = 1.2 cm (e.g., 1.5 cm), so as to be out of the dose build-up region. This could be accomplished with an additional build-up plate or by adding more medium to the flasks. Finally, off-axis ratios (OAR) should be considered in the calculation of dose.

3.3.2 Monochromatic X-Ray Energy Measurements

Table 3.8 lists the monochromatic x-ray energy measurements made for each cell irradiation session at CAMD. For each day listed (data not shown) the average ± standard error of the mean was calculated from three measurements. The collective average (± standard deviation) for each energy were 36.03 ± 0.24 keV for a nominal setting of 35 keV, 30.53 ± 0.11 keV for 30 keV, and 25.42 ± 0.20 keV for 25 keV.

In the method of energy tuning at the radiobiological beamline, the beam passes through the double-crystal, multi-layer monochromator at a grazing incidence angle calibrated to produce

Table 3.8: Energy measurements with the average (± standard deviation) energy of these measurements.

E = 35 keV

Date	Energy (keV)	Standard Error
3-Dec-10	35.92	0.04
17-Dec-10	35.88	0.09
2-Mar-11	36.44	0.11
7-Apr-11	36.23	0.07
28-Apr-11	36.17	0.07
20-May-11	35.93	0.12
8-Jun-11	36.15	0.12
8-Jun-11	36.06	0.07
24-Jun-11	36.12	0.09
22-Jul-11	35.98	0.07
12-Aug-11	36.04	0.12
29-Sep-11	36.22	0.07
12-Oct-11	36.00	0.09
26-Oct-11	35.33	0.04
1-Mar-12	35.92	0.10

Average **36.03**
Standard Deviation **0.24**

E = 25 keV

Date	Energy (keV)	Standard Error
25-Aug-11	25.48	0.05
31-Aug-11	25.61	0.04
9-Sep-11	25.28	0.04
14-Sep-11	25.63	0.06
14-Sep-11	25.58	0.09
22-Sep-11	25.48	0.03
23-Sep-11	25.39	0.05
7-Oct-11	25.33	0.02
13-Oct-11	25.46	0.03
21-Oct-11	24.83	0.04
17-Nov-11	25.64	0.03
18-Nov-11	25.36	0.06
13-Dec-11	25.41	0.07
2-Feb-12	25.62	0.05
15-Feb-12	25.22	0.03
23-Feb-12	25.43	0.07

Average **25.42**
Standard Deviation **0.20**

E = 30 keV

Date	Energy (keV)	Standard Error
18-Nov-11	30.72	0.06
2-Dec-11	30.54	0.04
9-Dec-11	30.47	0.10
3-Feb-12	30.56	0.09
16-Feb-12	30.40	0.05
23-Feb-12	30.43	0.07
1-Mar-12	30.60	0.05

Average **30.53**
Standard Deviation **0.11**

a particular energy. These grazing incidence angles are small and get smaller at higher energies; as the energy gets higher, the acceptance angle decreases. Photon energies of 35 keV is at the high end of the energy range of the radiobiological beamline (tunable energy range is 6-40 keV), and to achieve 35 keV the grazing incidence angle is 0.5074° and 0.4933° for 36 keV (private communication with Dr. Kyungmin Ham). Therefore, the 0.24 keV sigma corresponds to a

sigma in the grazing angle of 0.004^{o} (22.2π μradians). This means that accurate energy selection at high energies is severely limited by the mechanical accuracy of the grazing angle adjustment. Although irradiations were not always at exactly the same energy, and had an average of 36 keV and were > E_K of iodine, this difference from the target value of 35 keV should have little impact on the results.

3.3.3 Dose Rate Intercomparison between Ion Chamber & Film Measurements

The dose rates per 100 mA calculated from ion chamber measurements were compared with those measured from the film irradiated immediately before cell irradiations. The ion chamber dose rates were normalized to the equivalent film depth in PMMA using fractional depth dose values derived from MCNP5 simulations (since the ion chamber was irradiated in PMMA and the film was irradiated in the polystyrene test tube, the irradiation depth for film measurements was converted to equivalent depth in PMMA). Table 3.9 compares the mean film dose rate (determined from averaging the measured dose rates of two pieces of film irradiated consecutively inside a cell culture test tube), and mean ion chamber dose rate (calculated by averaging the three ionization measurements made consecutively inside a PMMA phantom) for each monochromatic x-ray irradiation.

The mean percent difference ± standard deviation between ion chamber dose rate and film dose rate per 100 mA were 27.5 ± 14.1% for 35 keV, 24.7 ± 3.9% for 30 keV, and 13.3 ± 6.0% for 25 keV, with the ion chamber measurements always overestimating the dose rate compared to film. These discrepancies are mostly likely a function of the timing between ion chamber measurements and film irradiations. The ion chamber measurements were usually made immediately (within approximately 15 minutes) after re-injection, when the synchrotron beam

Table 3.9: Dose rate per 100 mA (± standard error of the mean) intercomparison between ion chamber and film measurements. Measurements made for beam energies of (a) 35 keV, (b) 30 keV, and (c) 25 keV. Note that earlier in this project (9-10-2010 through 4-8-2011) only one set of film irradiations were done per experiment, for any number of re-injection cycles that occurred. In these cases, the film dose rate was scaled by the ratio of the ion chamber dose rates to calculate the dose to the cells.

(a) Energy = 35 keV

Date of irradiation	Mean film dose rate ($Gy*min^{-1}*100mA^{-1}$)	SEM	Mean IC dose rate at IC depth ($Gy*min^{-1}*100mA^{-1}$)	SEM	Mean IC dose rate at film depth ($Gy*min^{-1}*100mA^{-1}$)	% difference
9/10/2010	0.246	1.52E-04	0.277	0.001	0.287	-16.7
10/7/2010	0.188	0.004	0.234	0.006	0.242	-28.8
3/2/2011	0.089	0.001	0.103	0.002	0.107	-19.8
3/4/2011	0.060	3.25E-04	0.071	0.001	0.074	-23.6
4/6/2011	0.123	0.001	0.160	0.002	0.165	-34.3
4/7/2011	0.104	0.002	0.166	0.004	0.171	-65.0
4/8/2011	0.086	0.001	0.089	0.002	0.092	-7.1
4/28/2011	0.113	0.001	0.160	0.002	0.166	-46.7
5/19/2011	0.094	0.002	0.138	0.001	0.143	-51.9
	0.106	0.002	0.137	0.002	0.141	-33.7
7/20/2011	0.118	0.003	0.160	0.002	0.165	-40.5
	0.126	0.001	0.156	0.002	0.162	-28.9
7/21/2011	0.127	0.001	0.169	0.004	0.175	-37.3
	0.139	0.004	0.169	0.003	0.175	-26.1
7/22/2011	0.141	0.001	0.169	0.003	0.175	-23.7
	0.143	-	0.178	0.004	0.184	-28.6
8/11/2011	0.149	0.004	0.185	0.003	0.192	-29.1
	0.143	0.002	0.174	0.004	0.181	-26.3
8/12/2011	0.134	3.46E-04	0.175	0.004	0.181	-35.7
	0.134	0.003	0.164	0.002	0.170	-26.8
8/17/2011	0.113	0.003	0.154	0.003	0.160	-41.3
9/28/2011	0.318	0.005	0.328	0.001	0.340	-6.8
9/29/2011	0.292	0.002	0.315	0.001	0.326	-11.6
	0.324	0.003	0.339	3.26E-04	0.351	-8.5
10/12/2011	0.278	0.001	0.310	0.001	0.321	-15.6
10/20/2011	0.308	0.001	0.333	0.001	0.345	-12.2
10/27/2011	0.297	1.18E-05	0.330	0.001	0.342	-14.9

Mean % difference	-27.5
Standard Deviation	14.1

Table 3.9 (continued)

(b) Energy = 30 keV

Date of irradiation	Mean film dose rate ($Gy*min^{-1}*100mA^{-1}$)	SEM	Mean IC dose rate at IC depth ($Gy*min^{-1}*100mA^{-1}$)	SEM	Mean IC dose rate at film depth ($Gy*min^{-1}*100mA^{-1}$)	% difference
11/18/2011	0.768	0.009	0.861	4.87E-04	0.901	-17.3
12/2/2011	0.661	0.003	0.823	0.003	0.860	-30.2
12/7/2011	0.659	0.002	0.783	0.001	0.819	-24.3
12/9/2011	0.682	0.002	0.783	0.001	0.819	-20.0
2/3/2012	0.689	0.026	0.861	0.009	0.900	-30.6
	0.709	0.005	0.840	0.010	0.879	-23.9
2/16/2012	0.698	0.005	0.822	0.004	0.860	-23.2
2/23/2012	0.706	0.005	0.848	4.84E-04	0.887	-25.6
2/24/2012	0.704	0.018	0.855	0.016	0.894	-26.9
	0.705	0.024	0.843	0.008	0.882	-25.1
2/29/2012	0.688	0.001	0.821	0.012	0.859	-24.8
	0.710	0.012	0.818	0.011	0.855	-20.4
3/1/2012	0.679	0.005	0.836	0.004	0.875	-28.7

Mean % difference	-24.7
Standard Deviation	3.9

(c) Energy = 25 keV

Date of irradiation	Mean film dose rate ($Gy*min^{-1}*100mA^{-1}$)	SEM	Mean IC dose rate ($Gy*min^{-1}*100mA^{-1}$)	SEM	Mean IC dose rate at film depth ($Gy*min^{-1}*100mA^{-1}$)	% difference
8/26/2011	1.455	3.54E-04	1.492	0.001	1.606	-10.4
8/31/2011	1.416	0.009	1.467	0.005	1.578	-11.5
9/1/2011	1.429	0.016	1.516	0.003	1.631	-14.2
9/8/2011	1.405	0.011	1.456	0.004	1.566	-11.5
9/9/2011	1.418	0.012	1.426	0.005	1.534	-8.2
9/14/2011	1.413	0.016	1.428	0.004	1.537	-8.8
	1.467	0.002	1.503	0.001	1.617	-10.2
9/15/2011	1.421	0.019	1.437	0.004	1.546	-8.8
11/16/2011	1.748	0.020	1.790	0.002	1.926	-10.2
12/13/2011	1.418	0.005	1.677	0.021	1.805	-27.2
2/15/2012	1.244	0.061	1.433	0.020	1.542	-24.0
	1.334	0.065	1.449	0.024	1.560	-16.9
10/21/2011	1.218	0.004	1.256	0.002	1.352	-11.0

Mean % difference	-13.3
Standard Deviation	6.0

was initially less stable, whereas the film irradiations were made at least 1 hour after re-injection, right before cell irradiations.

Within the first hour of re-injection there were variations (decreases) in the beam output (dose per unit time per 100 mA) that was independent of the ring current (mA) right after re-injection (Brown *et al.* 2012b). It is believed that these variations are due to thermal changes in the radiobiological beamline components (i.e., monochromator). Once the beamline components reached thermal equilibrium, the dose rate per mA stabilized. Figure 3.15 shows the decrease in dose rate per 100 mA for the 35 keV beam as a function of time. The decrease of 20.7 ± 3.2% compares well with the mean of the ion chamber doses overestimating those of the film by 27.5%.

Figure 3.16 demonstrates the stability of the synchrotron beam from 3 to 7 hours after injection by plotting dose (normalized to 100 mA), as a function of ring current during a period of four hours for a 35 keV beam. Ion chamber measurements started three hours after beam re-injection and lasted four hours during the period of a single beam injection. The mean dose at 100 mA (± standard deviation) was 4.83 ± 0.14 Gy and the mean dose rate per 100 mA was 0.181 ± 0.0051 $Gy*min^{-1}$. These data indicate the dose rate is stable after three hours.

The major reasons why ion chamber measurements were not done one hour after re-injection were to not waste beam time and to minimize the total amount of time the cell test tubes were away from the tissue culture facility PBRC. At 35 keV, a tube that was prescribed 10 Gy would take approximately 50 minutes to irradiate when the dose rate was 0.2 $Gy*min^{-1}$ at 100 mA. At this rate, irradiating enough cell culture test tubes to create a survival curve (multiple cell culture test tubes irradiated with 0-10 Gy for monochromatic x-rays) required several hours.

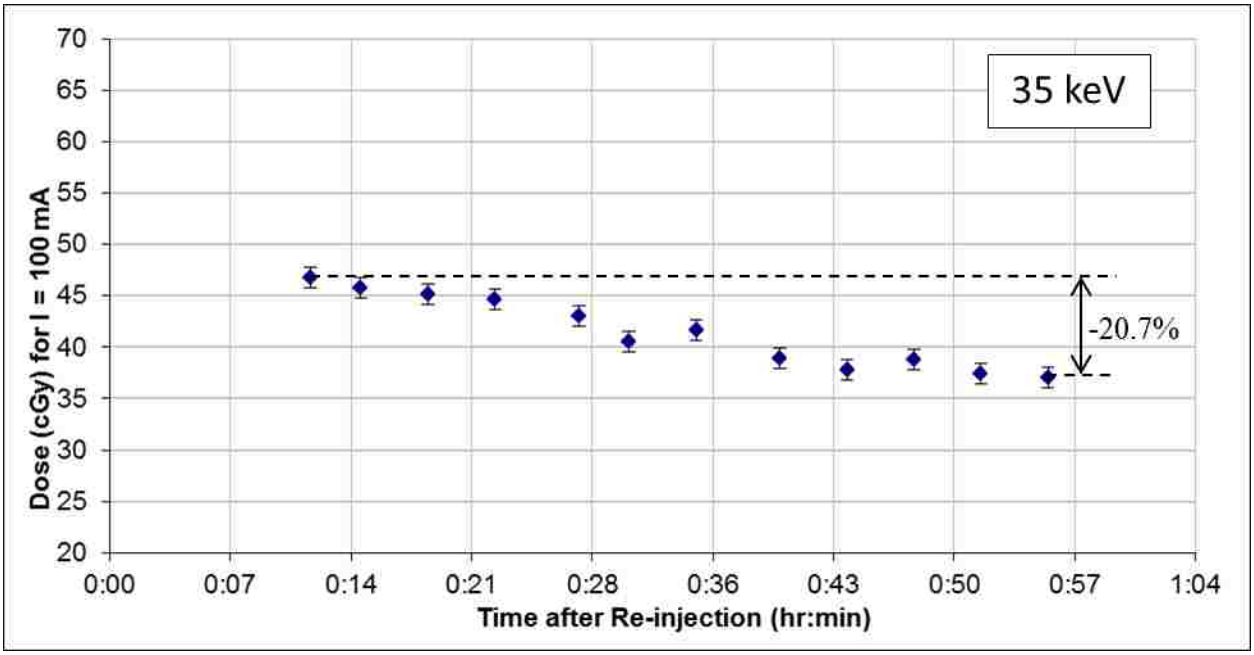

Figure 3.15: Fluctuation of dose (cGy) per 100 mA as a function of time after re-injection (hr:min) for 35 keV photons.

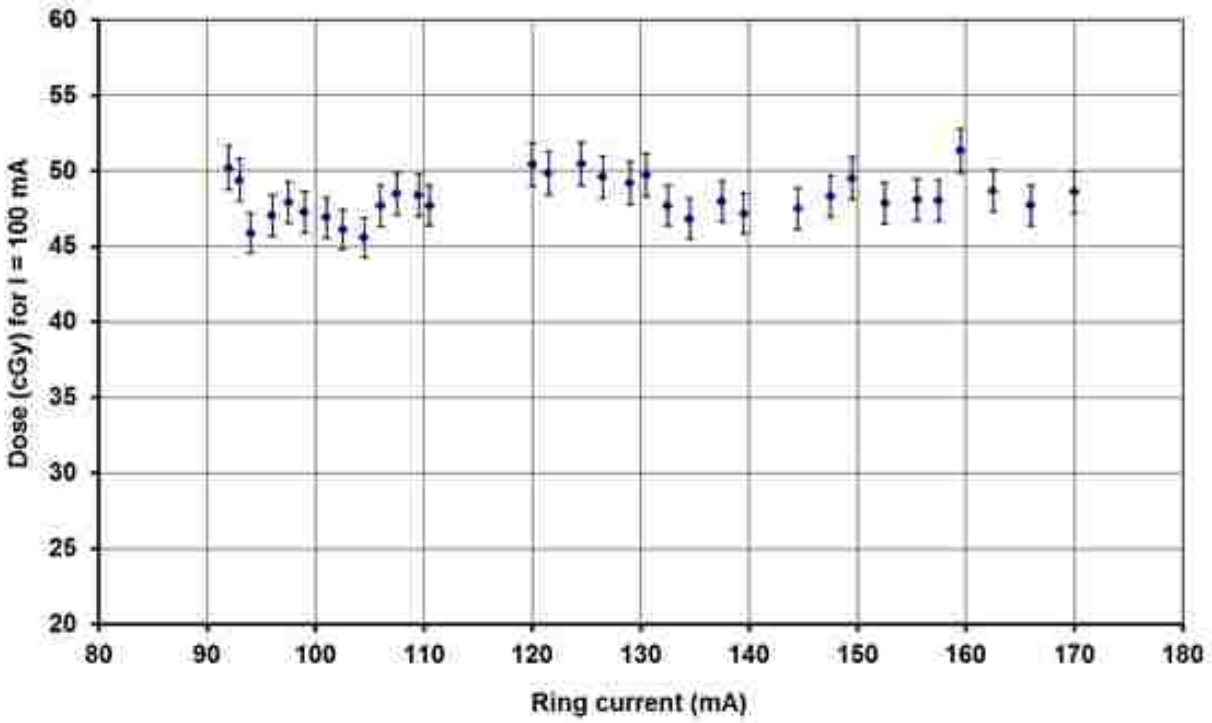

Figure 3.16: Dose (cGy) at 100 mA versus ring current (mA) for 35 keV during a time period of 3-7 hours after re-injection. Time period corresponded to 170−92 mA. Measurements using an ion chamber were made on 8/12/2010. The mean dose per 100 mA was 48.3 ± 1.4 cGy and the dose rate per 100 mA was 0.181 ± 0.0051 Gy*min^{-1}.

Although it would be possible to wait until the beam stabilizes to make ion chamber measurements, because the purpose of the ion chamber dose rate was solely to estimate the number of stage cycles the cell culture test tubes were required to undergo to receive the prescribed dose, it was not imperative to accurately determine the dose rate per 100 mA using the ion chamber (the film dose rate was used to determine the dose to the cells, not the ion chamber dose rate, as discussed in Section 3.2.2.6).

Thus, the comparison of film with ion chamber dosimetry was best tested for those cases in which the ion chamber dose was measured at least 1 hour after injection. Ion chamber measurements were made on four different days, approximately one hour post re-injection and followed by film irradiations. The mean of three ion chamber measurements were compared to the mean of two film dose rate measurements, as shown in Table 3.10. The mean percent differences ± standard deviation between the two methods were 13.5 ± 1.9% for 35 keV and 10.6 ± 0.6% for 25 keV (30 keV not measured). Why ion chamber measurements remained approximately 12% greater than film is not fully understood.

3.3.4 Summary of All Cell Irradiation Data

Table 3.11 shows the list of cell irradiation sessions required for this project. A total of 75 experimental sessions (75 days) were performed over the span of approximately two years, yielding 1,123 data points, of which 906 were usable. A data point was unused for any of the following reasons: (1) there was mold contamination in the cell culture tube; (2) the experimental session had a plating efficiency that was too low (< 20%); (3) zero dose flasks were unavailable for that experiment as a result of plating error or contamination, making it impossible to calculate a plating efficiency; (4) the irradiation source was down, preventing cell irradiations; or (5) the data point was considered a statistical outlier (explained in Section 4.2.3).

Table 3.10: Dose rate per 100 mA intercomparison between ion chamber and film measurements approximately one hour after re-injection. Measurements were done consecutively for 35 keV and 25 keV (no measurements were done at 30 keV).

Film depth in polystyrene tube (cm)	0.305
Film depth in polystyrene tube ($g*cm^{-2}$)	0.324
Equivalent film depth in PMMA (cm)	0.274
IC depth in PMMA (cm)	0.580

Date	10/20/2012	10/27/2012	10/21/2012	11/16/2012
Energy (keV)	35	35	25	25
MCNP5 FDD at IC depth	1.318	1.318	1.620	1.620
MCNP5 FDD at equivalent film depth	1.364	1.364	1.743	1.743
Mean IC dose rate ($Gy*min^{-1}*100$ mA)	0.333	0.330	1.256	1.790
Mean IC dose rate (corrected to film depth) ($Gy*min^{-1}*100$ mA)	0.345	0.342	1.352	1.926
Mean film dose rate ($Gy*min^{-1}*100$ mA)	0.308	0.297	1.218	1.748
Ratio (IC dose rate/Film dose rate)	1.122	1.149	1.110	1.102
Mean % difference ± standard deviation				
35 keV	13.5 ± 1.9			
25 keV	10.6 ±0.6			

Table 3.12 summarizes the usable data by combinations of energy and %IUdR, including quality assurance (QA) data (QA data were measured survival curves for the purpose of assessing whether 9L cell dose-response continued to be reproducible). Approximately 40% of the data were collected for 4 MV, which served as a baseline for this project. The remaining data points were distributed amongst the monochromatic energies, with 23% at 35 keV, 18% at 30 keV, and 19% at 25 keV. Several issues inhibited the collection of data evenly amongst the various %IUdR levels per energy. Irradiations at 4 MV were the easiest to collect because of several factors: (1) up to four flasks could be irradiated at a time; (2) minimal setup was required (3) no prior measurements were required before irradiations, once the EBT film calibration curve was established; and (4) the dose rate was constantly high (1.2 $Gy*min^{-1}$). In contrast, 35 keV was the most difficult energy for data collection. All monochromatic energies were limited to

Table 3.11: List of cell irradiation experimental sessions. A total of 75 experimental sessions (88 data sets) were done with 1,123 data points collected (1 flask per data point), of which 906 were usable and 217 unusable.

Data Set (DS)	Date	Energy	IUdR Conc. (μM)*	Doses (0-12 Gy)†	# of Flasks (Used data)	# of Flasks (Unused data)‡
1	7/7/2010	4 MV	0	0, 1, 2, 4, 6, 8	18	
3	7/22/2010	4 MV	0	0, 2, 4, 6, 8, 10, 12	20	2
5	8/25/2010	4 MV	0	0, 2, 4, 6	10	
DA002	9/10/2010	35 keV	0	0, 1, 2, 4, 5, 7	7	
DA003	10/7/2010	35 keV	0	0, 2, 4, 5, 7, 9, 10	9	
DA004	10/8/2010	35 keV	0	0, 2, 4, 6, 7, 9, 10	7	
10	11/4/2010	4 MV	0	0, 2, 6, 10	12	
11	11/11/2010	4 MV	0	0, 2, 6, 8, 10	16	
13	12/16/2010	35 keV	1	0, 1, 3		11
013B	12/17/2010	35 keV	3	0, 1, 2, 4		11
14	1/19/2011	4 MV	0	0, 4, 6, 10		9
			1	0, 2, 4, 6, 8, 10		18
15	2/9/2011	4 MV	1	0, 2, 4, 6	14	
16	2/16/2011	4 MV	0	0, 4, 8	7	
			1	0, 1, 2, 4, 6, 8, 10	15	
17	3/2/2011	35 keV	0	0, 2, 5, 6	7	
			1	0, 1, 2	7	
19	3/4/2011	35 keV	1	0, 1, 2, 3	9	
021A	4/6/2011	35 keV	1	0, 1, 2, 4	12	
021B	4/7/2011	35 keV	0	0, 2, 3, 4, 6, 7	11	1
021C	4/8/2012	35 keV	1	0, 1, 2, 3, 4, 5	16	
22	4/14/2011	4 MV	0	0, 4, 10	7	
			1	0, 2, 4, 6, 8, 10	12	1
			3	0, 2, 4, 6, 8, 10	13	
023A	4/27/2011	35 keV	0	0, 2, 4, 6, 7		11
023B	4/28/2011	35 keV	3	0, 1, 2, 3	9	
24	5/11/2011	4 MV	0	0, 4, 10	9	
			3	0, 2, 4, 6, 8, 10	18	
025A	5/18/2011	35 keV	0	0, 2, 4, 5		9
26	5/19/2011	35 keV	1	0, 3, 5, 7	9	
025B	5/20/2011	35 keV	0	0, 2, 7, 9		7
027A	6/15/2011	4 MV	0	0, 2, 4, 8, 10, 12	19	
027B	6/16/2011	4 MV	0	0, 8, 12	9	
			3	0, 2, 4, 6, 8, 10, 12	21	1
28	6/22/2011	35 keV	0	0, 2, 4, 5, 9, 10, 11		14
29	6/23/2011	35 keV	0	0, 2, 5, 7, 9, 12		9

Table 3.11 (continued)

Data Set (DS)	Date	Energy	IUdR Conc. (μM)*	Doses (0-12 Gy)†	# of Flasks (Used data)	# of Flasks (Unused data)‡
30	6/30/2011	4 MV	0	0, 8, 12	9	
			3	0, 2, 4, 6, 8, 10, 12	21	
31	7/7/2011	4 MV	0	0, 12	6	
			3	0, 2, 4, 6, 8, 10, 12	20	1
32	7/14/2011	4 MV	0	0, 12	6	
			1	0, 2, 4, 6, 8, 10, 12	21	
033A	7/20/2011	35 keV	1	0, 6, 7, 9, 11	9	
033B	7/21/2011	35 keV	1	0, 5, 6, 7, 10, 12	9	
34	7/22/2011	35 keV	3	0, 2, 4, 7	9	
035A	8/11/2011	35 keV	1	0, 9, 10	5	
035B	8/12/2011	35 keV	1	0, 9, 11	7	
036A	8/17/2011	35 keV	3	0, 2, 4, 6	6	
036B	8/18/2011	35 keV	3	0, 2, 4, 6		6
37	8/26/2011	25 keV	3	0, 3, 5, 8, 9, 11, 13, 14	9	4
38	8/31/2011	25 keV	3	0, 2, 4, 6, 8, 9, 10	17	1
39	9/1/2011	25 keV	1	0, 2, 3, 6, 7, 9, 10	17	1
040A	9/8/2011	25 keV	0	0, 2, 4, 5, 6, 8, 10	18	
040B	9/9/2011	25 keV	0	0, 2, 4, 6, 8, 10	18	
41	9/14/2011	25 keV	1	0, 2, 5, 6, 7, 8, 10	17	1
42	9/15/2011	25 keV	3	0, 2, 4, 6, 8, 10	17	1
043**	9/23/2011	4 MV	0	0, 2, 4, 6, 8, 10, 12	21	
044**	9/28/2011	35 keV	0	0, 3	9	
			3	0, 3	7	
45	9/29/2011	35 keV	0	0, 8	6	
			3	0, 8	6	
47	10/12/2011	35 keV	3	0, 5, 7	9	
48	10/20/2011	35 keV	3	0, 3, 4	11	
49	10/21/2011	25 keV	0	0, 2, 4, 5, 7, 9, 10	17	
50	10/27/2011	35 keV	3	0, 3, 5	12	
51	11/16/2011	25 keV	1	0, 2, 4, 6, 8, 9, 10	16	2
52	11/17/2011	25 keV	3	0, 6, 7, 8, 9, 10		13
53	11/18/2012	30 keV	0	0, 2, 4, 6, 8, 10	12	
54	12/1/2011	30 keV	0	0, 2, 4, 6, 8, 10		18
55	12/2/2011	30 keV	3	0, 1, 4, 5, 7, 9	14	
56	12/7/2011	30 keV	0	0, 2, 4, 5, 6, 9	11	1
57	12/8/2011	30 keV	3	0, 2, 4, 6, 8		15

Table 3.11 (continued)

Data Set (DS)	Date	Energy	IUdR Conc. (μM)*	Doses (0-12 Gy)†	# of Flasks (Used data)	# of Flasks (Unused data)‡
58	12/9/2011	30 keV	3	0, 2, 4, 6, 9, 10	13	
59	12/12/2011	30 keV	0	0, 2, 4, 6, 8, 9, 10		19
60	12/13/2011	25 keV	3	0, 4, 5, 7, 8, 9	12	1
061**	1/23/2012	4 MV	0	0, 2, 4, 6, 8, 10	12	
62	1/24/2012	4 MV	3	0, 2, 4, 6, 8, 10		13
63	2/2/2012	25 keV	1	0, 2, 4, 5, 7, 8, 9, 10		15
64	2/3/2012	30 keV	0	0, 2, 4, 6, 7, 8, 9, 10	19	
065**	2/9/2012	4 MV	3	0, 2, 4, 6, 8, 10	13	
66	2/15/2012	25 keV	3	0, 5, 7, 8, 10	14	
67	2/16/2012	30 keV	0	0, 2, 4, 6, 7, 9	19	
68	2/23/2012	30 keV	0	0, 2, 4, 6, 8, 10	18	
69	2/24/2012	30 keV	0	0, 2, 4, 6, 8, 10	18	
70	2/29/2012	30 keV	3	0, 2, 4, 6, 8, 10	18	
71	3/1/2012	30 keV	3	0, 2, 4, 6, 8, 9, 10	17	1
072**	7/19/2012	4 MV	0	0, 2, 6, 10	9	
			3	0, 2, 6, 10	9	
SUMMARY Total					**906**	**217**

* %IUdR vs. IUdR concentration in the medium was 0 μM → 0% IUdR, 1 μM → 9% IUdR, and 3 μM → 18% IUdR.

** QA experiment.

† Doses were rounded off to the nearest whole number for the purpose of this table.

‡ Data were unused if: contaminated, low PE, no zero dose flasks available, irradiation source down, or if it was an outlier.

irradiation of one flask at a time. Coupling this limitation with a 35 keV dose rate of about 0.2 $Gy*min^{-1}$ per 100 mA, resulted in, at best, the ability to irradiate 6 cell culture test tubes in one day. Because of small effects seen when using 9% IUdR at 25 keV, 9% IUdR data was not collected subsequently at 30 keV.

Table 3.13 shows the mean ± standard error of the mean of the survival of unirradiated cells containing the %IUdR levels studied. The mean plating efficiencies ± standard deviation for all experiments within each drug level were 46 ± 14%, 47 ± 15%, and 42 ± 16% for 0, 9, and 18% IUdR. IUdR had little impact on the mean plating efficiency at each IUdR level; however, the plating efficiency could vary considerably from one individual data set to another.

Table 3.12: Summary of number of useful data points (cell cultures) categorized by energy and %IUdR. QA data points were included.

Energy	# of Data Points				
	0% IUdR	9% IUdR	18% IUdR	# QA data pts	Total
4 MV	148	62	93	64	**367**
35 keV	47	83	62	16	**208**
30 keV	97	--	62	--	**159**
25 keV	53	50	69	--	**172**
# QA data pts	51	--	29	80	
Total	**396**	**195**	**315**		**906**

Table 3.13: Mean plating efficiency for each level of %IUdR.

% IUdR	# Data Sets	Mean Survival ± SEM	σ
0%	34	46% ± 2%	14%
9%	15	47% ± 4%	15%
18%	24	42% ± 3%	16%

CHAPTER 4: AIM 3, DATA ANALYSIS OF CELL SURVIVAL CURVES

Aim 3: A survival curve will be fit to data for each combination of percent thymidine replacement and photon beam energy using a linear quadratic model for surviving fraction, from which SER_{10} values will be determined.

4.1 Goal

The goal for this aim was to analyze surviving fraction versus dose data using a common radiobiological model. Such analysis assesses the behavior of rat 9L glioma cells when subjected to various combinations of photon beam energy and percent thymidine replacement by IUdR. Because data for each combination was the result of multiple measured data sets (see Table 3.11), a method of analysis was utilized to minimize the propagation of large systematic errors in the plating efficiency from biasing the errors in individual data points from a single measured data set. Also, a method was employed to isolate the effects of linear energy transfer, radiosensitization, and Auger electrons on the survival fraction versus dose curve.

4.2 Methods & Materials

4.2.1 Plotting the Cell Survival Curve & Chi-Squared Fit

The measured data points of $SF \pm \sigma$ versus D were plotted on a semi-log grid (linear in dose, logarithmic in surviving fraction), where each data point represented survival fraction from a single cell culture flask. Although plotted using a semi-log grid, the SF versus D curves were fit in linear space to the linear quadratic model: $SF = A * e^{-\alpha*D-\beta*D^2}$, where A, α and β were fitting parameters.

A weighted curve-fit was done by minimizing chi-squared, χ^2, using the Sigma Plot®12 (v 12.0) nonlinear curve-fitting algorithm. The Sigma Plot®12 nonlinear curve-fitting algorithm used the Marquardt-Levenberg algorithm (Marquardt 1963) to find the A, α, β parameters of the

linear quadratic model that gave the best fit of the equation to the data. This algorithm seeks the values of the parameters that minimize χ^2, the weighted sum of the squared differences between the values of the measured and calculated (or predicted) data; the weighting factor is σ^{-2}, derived from the uncertainty σ for each data point. This process is iterative, repeating until the differences between the residual sum of squares decreases by less than a predetermined amount. This condition is known as convergence.

4.2.2 Combining Data from Multiple Measured Data Sets for a Single Experimental Condition (E, %IUdR)

To achieve sufficient statistics to meaningfully quantify differences in the survival curves for differing experimental conditions (E, %IUdR), multiple sets of measured data (accrued on different dates) were required. In all cases, the plating efficiencies (average of "zero" dose points) varied amongst measured data sets as evident by large standard deviations (see Table 3.13), and had large error bars ranging from 0.041 to 0.210. Therefore, normalizing each data point to the plating efficiency for its respective data set and then fitting all data sets together would propagate large systematic and random errors from the "zero" dose points to all other data points in the data set; furthermore, the data points would no longer be statistically independent. Additionally, some data sets had a small number of data points versus dose, hindering the fitting of that data to an individual survival curve.

Consequently, the following fitting scheme, illustrated in Figure 4.1, was utilized. First, the surviving fractions for all data points in a single data set *j* were normalized temporarily to the plating efficiency (average of "zero" dose points) for that data set. The plating efficiency's uncertainty was ignored and not propagated into the error of the remaining survival fraction data points. Then the data points from all data sets comprising a single experimental condition (E,

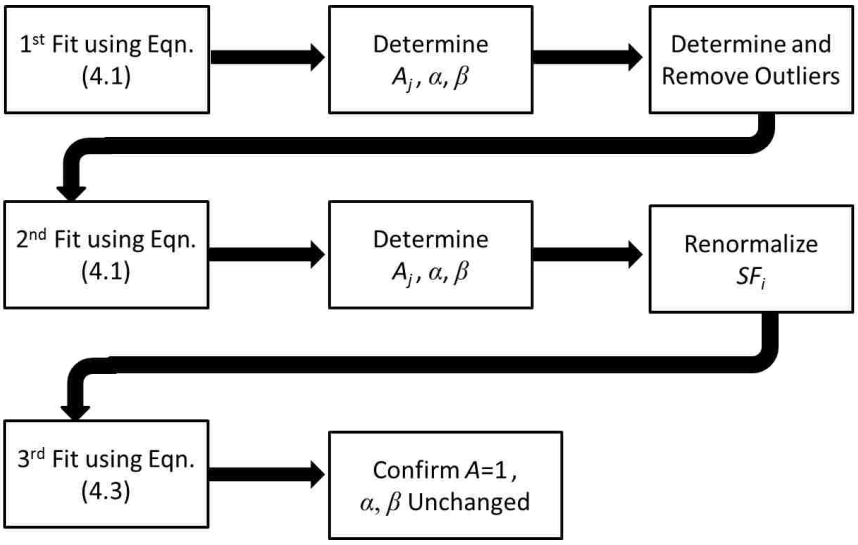

Figure 4.1: Flow chart of the overall data analysis process.

%IUdR), including the "zero" dose points, were fit to the mathematical form of the survival curve by minimizing chi-squared for points in all multiple data sets simultaneously (see Equation (4.1)). Data points for each data set were then renormalized and re-fit to a final survival curve (see Equation (4.2)) that had a (SF, D = 0) = 1.

4.2.2.1 First Curve Fit Routine

The purpose of the first curve fit routine was to identify outliers. The data for a single experimental condition (E, %IUdR), comprised of a total of R independent data sets, were fit to the linear quadratic model having a single value for α and β, but different normalizations (plating efficiencies), A_j, for each of the j data sets. This was accomplished within Sigma Plot®12 by doing a weighted least-squares fit of the data points (D_i, $SF_i \pm \sigma_i$) with i = 1, N to the objective function:

$$SF_c(D_i) = \sum_{j=1}^{R} (A_j * \delta_{i,j}) * e^{-\alpha * D_i - \beta * D_i^2}, \qquad \text{for } i = 1, N, \tag{4.1}$$

where: $SF_c(D_i)$ = Calculated SF for the i^{th} data point,

D_i = Dose of the i^{th} data point,

$\delta_{i,j}$ = 1 if the i^{th} data point is part of the j^{th} measured data set,

A_j = Normalization parameter for the j^{th} measured data set,

α, β = Fit parameters for the survival curve for all N data points.

Note that N is the total number of data points in R data sets with the same (E, %IUdR), i.e., $N = \sum_{j=1}^{R} N_j$, where N_j is the total number of data points in the j^{th} measured data set.

After the first curve fit routine, outliers were identified (see Section 4.2.3) and removed from the data in preparation for the second curve fit.

4.2.2.2 Second & Third Curve Fit Routines

The second curve fit routine, using the data set with outliers removed, determined new values for α, β and new normalization parameters (A_j). Then, the data points and error bars ($SF_i \pm \sigma_i$) within the j^{th} data set were renormalized by the factor $(A_j)^{-1}$. Last, the renormalized composite data set was fit a third time to the function:

$$SF(D_i) = A * e^{-\alpha * D_i - \beta * D_i^2}, \tag{4.2}$$

If the renormalization procedure was done correctly, then A equaled unity and α, β remained the same as that resulting from the second curve fit routine. The purpose of the third curve fit routine was to check that renormalizations were done properly and to calculate the reduced chi-squared, minimized by the Sigma Plot®12 fit and given by χ_ν^2:

$$\chi_\nu^2 = \frac{1}{\nu} \sum_{i=1}^{N} \frac{[SF_i(D_i) - SF_c(D_i)]^2}{\sigma_i^2}, \tag{4.3}$$

where ν = Number of degrees of freedom calculated by $N - 3$,

$SF_i(D_i)$ = Measured SF for the i^{th} data point at dose D_i,

σ_i = Uncertainty in $SF_i(D_i)$,

$SF_c(D_i)$ = SF calculated by the curve-fit at D_i.

To demonstrate this procedure, consider the data set listed in Table 4.1 for (25 keV, 0% IUdR), which contained 53 data points with no outliers for $R = 3$ measured data sets (40A, 40B, and 49 from Table 4.1). The data sets were fit simultaneously to Equation (4.1) using the weighted curve-fit algorithm in Sigma Plot®12. Figure 4.2(a)-(b) shows the results of this first fit with the colored lines representing the χ^2 fit to the corresponding data points. The "zero" dose points (for each color) denote the fitted normalization constants (A_j); A_j values for data sets 40A, 40B, and 49 were 0.8992, 0.7957, and 1.0773, respectively. The measured data sets, which contained no outliers, were then normalized by these constants and re-fitted using Equation (4.2). The final fit (Table 4.2(c)) yielded a normalization factor of unity ($A = 1.000$), as expected, and the values for α and β remained unchanged.

Table 4.1: Curve-fitting information for experimental condition (25 keV, 0% IUdR). Table shows data (columns 2−4), fitting parameters (columns 5−8), theoretical "zero" dose point (column 9), and renormalized surviving fraction data and weighting factor (columns 10−12) for final fit to the $R = 3$ data sets.

Data Set j	D_i (Gy)	SF_i	σ_{SFi}	σ_{SFi}^{-2}	$\delta_{i,j}$ 40A	$\delta_{i,j}$ 40B	$\delta_{i,j}$ 49	A_j	$SF_i * A_j^{-1}$	$\sigma_{SFi} * A_j^{-1}$	$\sigma_{SFi}^{-2} * A_j^{-1}$
9/8/2011	0.0	0.877	0.238	17.59	1	0	0	0.8992	0.975	0.265	14.23
(040A)	0.0	1.108	0.278	12.95	1	0	0	0.8992	1.232	0.309	10.47
	0.0	1.015	0.262	14.53	1	0	0	0.8992	1.129	0.292	11.75
	2.1	0.877	0.238	17.59	1	0	0	0.8992	0.975	0.265	14.23
	2.1	0.600	0.188	28.29	1	0	0	0.8992	0.667	0.209	22.88
	2.1	0.739	0.214	21.89	1	0	0	0.8992	0.821	0.238	17.71
	4.3	0.417	0.144	48.20	1	0	0	0.8992	0.464	0.160	38.99
	4.3	0.584	0.176	32.34	1	0	0	0.8992	0.649	0.196	26.16
	4.2	0.292	0.118	72.35	1	0	0	0.8992	0.325	0.131	58.46
	5.6	0.334	0.090	124.51	1	0	0	0.8992	0.371	0.100	100.71
	5.6	0.375	0.096	108.86	1	0	0	0.8992	0.417	0.107	88.10
	5.5	0.313	0.086	133.92	1	0	0	0.8992	0.348	0.096	108.31
	8.2	0.042	0.021	2255.19	1	0	0	0.8992	0.046	0.023	1816.12
	8.1	0.073	0.028	1270.70	1	0	0	0.8992	0.081	0.031	1023.99
	8.0	0.125	0.037	724.39	1	0	0	0.8992	0.139	0.041	584.28
	9.9	0.042	0.017	3382.78	1	0	0	0.8992	0.046	0.019	2733.08
	9.7	0.028	0.014	5106.29	1	0	0	0.8992	0.031	0.016	4125.28
	9.5	0.049	0.019	2890.44	1	0	0	0.8992	0.054	0.021	2337.13

Table 4.1 (continued)

Data Set j	D_i (Gy)	SF_i	σ_{SFi}	σ_{SFi}^{-2}	$\delta_{i,j}$ 40A	$\delta_{i,j}$ 40B	$\delta_{i,j}$ 49	A_j	$SF_i * A_j^{-1}$	$\sigma_{SFi} * A_j^{-1}$	$\sigma_{SFi}^{-2} * A_j^{-1}$
9/9/2011	0.0	0.857	0.245	16.63	0	1	0	0.7957	1.077	0.308	10.52
(040B)	0.0	1.095	0.289	11.94	0	1	0	0.7957	1.376	0.364	7.56
	0.0	1.048	0.281	12.70	0	1	0	0.7957	1.317	0.353	8.03
	2.0	0.524	0.179	31.09	0	1	0	0.7957	0.658	0.225	19.69
	2.0	0.714	0.218	21.08	0	1	0	0.7957	0.898	0.274	13.35
	2.0	0.667	0.208	23.02	0	1	0	0.7957	0.838	0.262	14.58
	4.2	0.474	0.161	38.81	0	1	0	0.7957	0.596	0.202	24.58
	4.2	0.238	0.113	77.94	0	1	0	0.7957	0.299	0.142	49.32
	4.1	0.172	0.090	122.97	0	1	0	0.7957	0.217	0.113	77.81
	5.6	0.474	0.114	77.62	0	1	0	0.7957	0.596	0.143	49.14
	5.5	0.237	0.076	173.22	0	1	0	0.7957	0.298	0.096	109.60
	6.4	0.259	0.080	157.13	0	1	0	0.7957	0.325	0.100	99.41
	8.2	0.087	0.031	1016.00	0	1	0	0.7957	0.109	0.039	642.08
	8.0	0.098	0.033	897.98	0	1	0	0.7957	0.123	0.042	567.48
	7.9	0.054	0.025	1653.95	0	1	0	0.7957	0.068	0.031	1046.11
	10.0	0.029	0.015	4734.70	0	1	0	0.7957	0.036	0.018	3010.99
	9.8	0.043	0.018	3131.90	0	1	0	0.7957	0.054	0.022	1975.78
	9.6	0.051	0.019	2674.08	0	1	0	0.7957	0.063	0.024	1699.54
10/21/2011	0.0	0.869	0.188	28.19	0	0	1	1.0773	0.807	0.175	32.70
(049)	0.0	1.178	0.231	18.72	0	0	1	1.0773	1.093	0.215	21.73
	0.0	0.953	0.200	24.94	0	0	1	1.0773	0.885	0.186	28.95
	10.1	0.060	0.014	5121.25	0	0	1	1.0773	0.056	0.013	5920.92
	9.8	0.041	0.012	7557.70	0	0	1	1.0773	0.038	0.011	8775.05
	9.6	0.057	0.014	5414.46	0	0	1	1.0773	0.053	0.013	6274.33
	7.7	0.165	0.029	1217.16	0	0	1	1.0773	0.153	0.027	1408.90
	7.6	0.170	0.029	1181.65	0	0	1	1.0773	0.157	0.027	1370.44
	7.4	0.124	0.025	1655.85	0	0	1	1.0773	0.115	0.023	1917.68
	5.7	0.294	0.053	350.93	0	0	1	1.0773	0.273	0.050	406.97
	5.5	0.361	0.060	277.17	0	0	1	1.0773	0.335	0.056	321.29
	3.9	0.712	0.150	44.51	0	0	1	1.0773	0.661	0.139	51.65
	3.8	0.597	0.134	55.51	0	0	1	1.0773	0.554	0.125	64.44
	3.8	0.643	0.141	50.61	0	0	1	1.0773	0.597	0.131	58.70
	2.3	0.757	0.172	33.72	0	0	1	1.0773	0.703	0.160	39.14
	2.2	0.617	0.151	43.69	0	0	1	1.0773	0.573	0.140	50.70
	2.2	0.729	0.168	35.39	0	0	1	1.0773	0.677	0.156	41.07

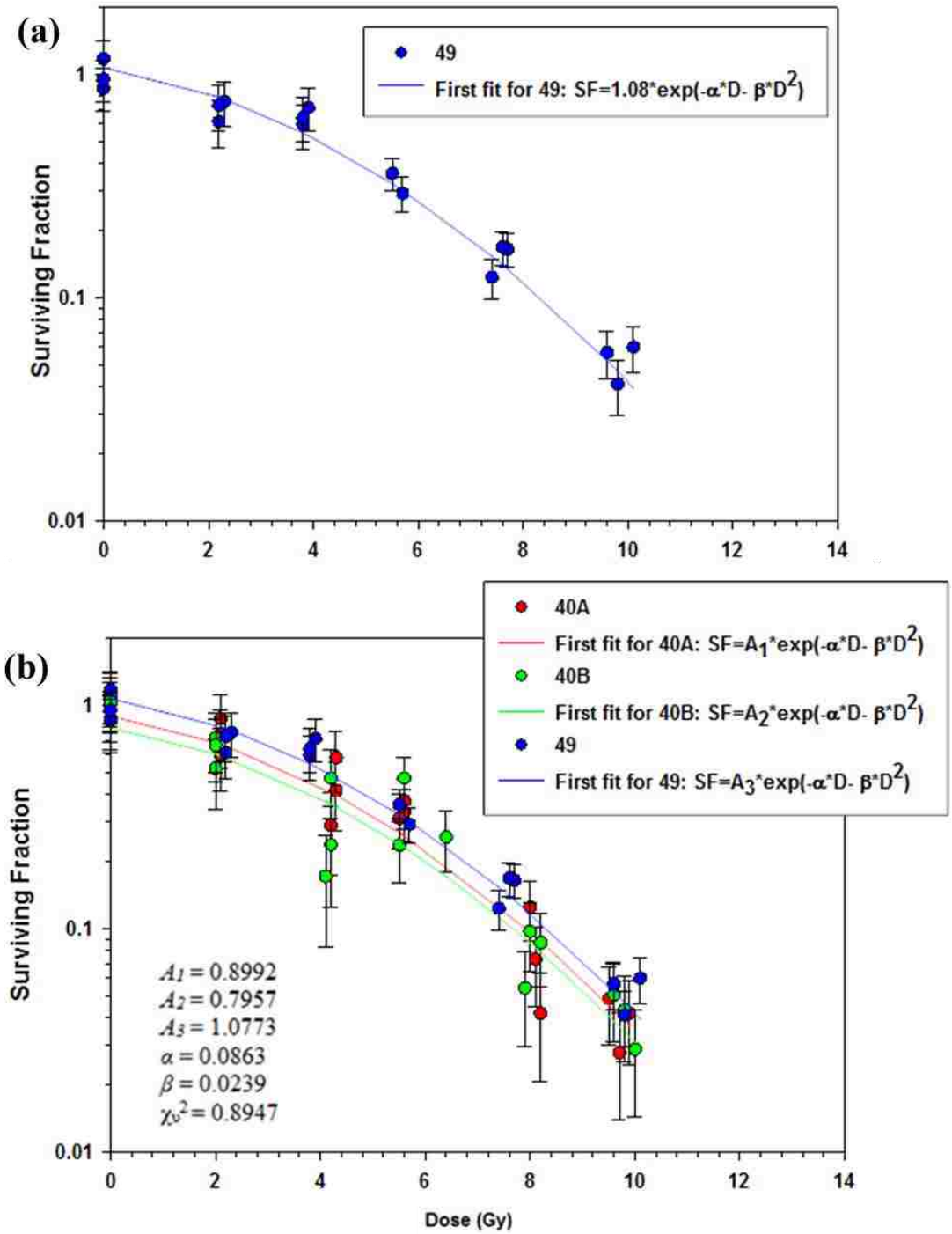

Figure 4.2: Example of fitting the measured data (R = 3) for (25 keV, 0% IUdR). (a) Fit for a single data set. (b) Individual simultaneously-fitted curves for the three data sets; the fitted values were α = 0.0863, β = 0.0239, A_1 = 0.8992, A_2 = 0.7957, A_3 = 1.0773, and χ_v^2 = 0.8947. (c) Final fitted curve for all renormalized data points; the final fit parameters were α = 0.0863, β = 0.0239, A = 1.000, and χ_v^2 = 0.8584.

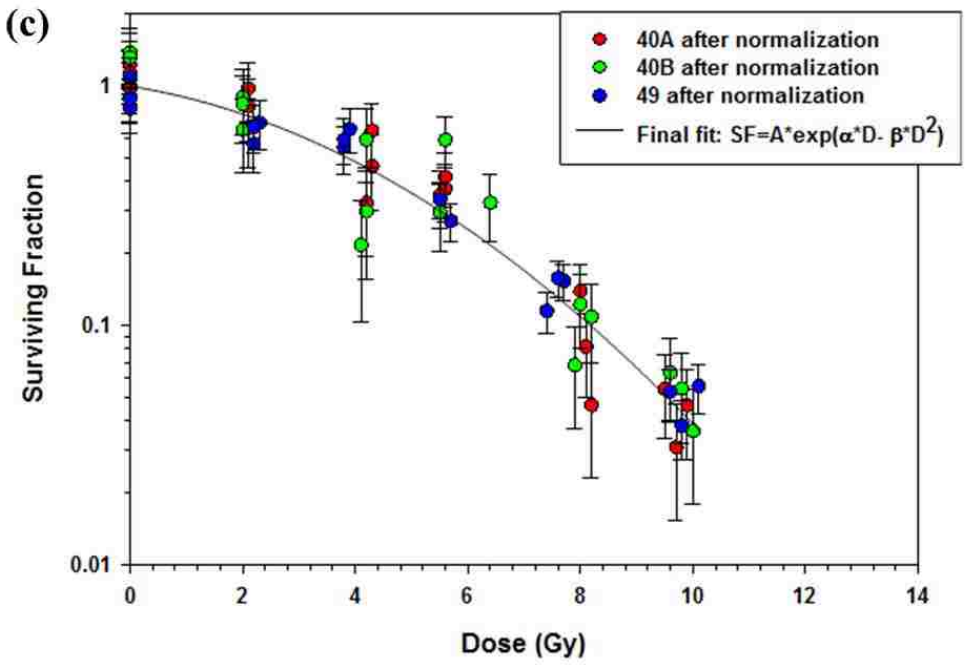

Figure 4.2 (continued)

4.2.3 Removing Outliers

After data points of an experimental condition (E, %IUdR) underwent the first curve fit routine (Section 4.2.2.1), a threshold of 2.5 standard deviations (2.5σ), based on Chauvenet's criterion (Bevington 1992), was imposed to determine whether a data point was an outlier, and thus eliminated from the data set before re-fitting the data to Equation (4.1). Sigma Plot®12 generated the residuals:

$$Residual = \frac{SF_i(D_i) - SF_P(D_i)}{\sigma_i}, \tag{4.4}$$

for each data point as part of the fit routine, making it convenient to determine how many standard deviations away a data point was from the fit. If the absolute value of the residual was larger than 2.5, then the data point was considered an outlier and was removed from the set of data points (see a subset of (25 keV, 9% IUdR) data points evaluated for outliers in Table 4.2).

4.2.4 Determination of Sensitization Enhancement Ratios at 10% Survival

The sensitization enhancement ratio at 10% surviving fraction (SER_{10}) was calculated for each experimental condition as the ratio of dose required to achieve 10% survival (D_{10}) for cells under one (E, %IUdR) experimental condition to another, i.e., for cells without IUdR irradiated at 4 MV to that of cells with DNA-incorporated IUdR irradiated at photon energy E. $SER_{10,T}$(E, %IUdR) is the combined or total SER, which includes (1) the effect of enhanced cell killing caused by the linear energy transfer (LET) effect of keV photons, (2) the radiosensitization (RS) effect of IUdR, and (3) the Auger effect (AE) from IUdR. Assuming that the LET, RS, and AE effects are independent of each other, it has been assumed that the $SER_{10,T}$(E, %IUdR) is the product of $SER_{10,LET}$(E, %IUdR), $SER_{10,RS}$(E, %IUdR), and $SER_{10,AE}$(E, %IUdR).

Table 4.2: Outlying data in experimental data set (25 keV, 9% IUdR). Column "*Res* > 2.5" evaluated the residuals (*res*) of each data point. If the absolute value of the residual was > 2.5, it was flagged with a "1". Flagged data points (highlighted in red) were removed from data set *j* for that experimental condition, which was re-fit with Equation (4.1) to determine the final normalization constants, A_j.

Data Set *j*	D_i (Gy)	SF_i	σSF_i	*SFp*	*Res*	*Res > 2.5*
(039)	0	1.129	0.236	0.7771	1.4925	0
	0	0.802	0.187	0.7771	0.1330	0
	0	1.069	0.227	0.7771	1.2878	0
	2.2	0.763	0.165	0.6195	0.8717	0
	2.2	0.689	0.154	0.6195	0.4519	0
	2.1	0.664	0.151	0.6307	0.2247	0
	3.4	0.633	0.113	0.4722	1.4253	0
	3.4	0.383	0.083	0.4722	-1.0768	0
	3.3	0.633	0.113	0.4849	1.3126	0
	5.9	0.221	0.055	0.1919	0.5335	0
	5.8	0.258	0.060	0.2007	0.9547	0
	5.7	0.185	0.050	0.2097	-0.5010	0
	7.3	0.052	0.020	0.0951	-2.2044	0
	7.2	0.074	0.024	0.1005	-1.1295	0
	9.4	0.021	0.011	0.0254	-0.4110	0

Table 4.2 (continued)

Data Set *j*	D_i (Gy)	SF_i	σSF_i	*SFp*	*Res*	*Res > 2.5*
	9.2	0.011	0.007	0.0292	-2.5019	1
	9	0.042	0.015	0.0335	0.5726	0
(041)	0	1.075	0.235	1.2306	-0.6612	0
	0	0.991	0.221	1.2306	-1.0853	0
	0	0.934	0.212	1.2306	-1.3985	0
	1.7	1.189	0.252	1.0651	0.4896	0
	1.7	0.934	0.212	1.0651	-0.6183	0
	1.7	1.160	0.248	1.0651	0.3842	0
	4.5	0.767	0.176	0.5320	1.3379	0
	4.4	0.665	0.160	0.5507	0.7159	0
	4.4	0.767	0.176	0.5507	1.2316	0
	6.1	0.269	0.064	0.2773	-0.1354	0
	6.1	0.345	0.075	0.2773	0.9122	0
	6	0.230	0.059	0.2904	-1.0238	0
	8.2	0.096	0.026	0.0890	0.2706	0
	8	0.077	0.023	0.1005	-1.0443	0
	7.9	0.134	0.031	0.1067	0.8961	0
	9.9	0.055	0.016	0.0281	1.7439	0
	9.7	0.060	0.016	0.0325	1.6676	0
	10.4	0.064	0.017	0.0192	2.6469	1
(051)	0	1.255	0.319	0.8837	1.1615	0
	0	0.982	0.272	0.8837	0.3604	0
	0	0.764	0.233	0.8837	-0.5165	0
	2	0.495	0.163	0.7296	-1.4416	0
	2	0.630	0.188	0.7296	-0.5322	0
	2	0.810	0.219	0.7296	0.3653	0
	4.1	0.675	0.170	0.4368	1.4027	0
	4.1	0.472	0.137	0.4368	0.2580	0
	4	0.540	0.148	0.4509	0.5985	0
	6.5	0.054	0.039	0.1644	-2.8628	1
	6.4	0.243	0.085	0.1726	0.8292	0
	6.3	0.297	0.095	0.1812	1.2234	0
	8	0.095	0.037	0.0722	0.6329	0
	7.8	0.082	0.034	0.0813	0.0144	0
	8.8	0.068	0.031	0.0436	0.7971	0
	9.7	0.110	0.031	0.0233	2.7815	1

Each SER_{10} value results from the comparison of specific conditions for D_{10}. $SER_{10,T}$ is given by reference to (4 MV, 0% IUdR):

$$SER_{10,T}(E, \%IUdR) = \frac{D_{10}(4\ MV, 0\%\ IUdR)}{D_{10}(E, \%\ IUdR)}. \tag{4.5}$$

The values for D_{10} and their uncertainty were determined from the fitted survival curves and corresponding 95% confidence intervals. The uncertainties in D_{10} (±σ) were estimated as one-quarter of the dose range spanned by the 95% confidence interval for the fits of the measured data to the linear quadratic model, which were calculated by SigmaPlot®12. The total dose range spanned by the 95% confidence interval represents 4σ (i.e., ± 2σ), so one-fourth of the 95% confidence interval equals one σ.

Separate SER_{10} values can be written for each effect: LET, RS, and AE. The $SER_{10,LET}$ compares D_{10} without IUdR for 4 MV to energy E:

$$SER_{10,LET}(E, \%IUdR) = \frac{D_{10}(4\ MV, 0\%\ IUdR)}{D_{10}(E, 0\%\ IUdR)}. \tag{4.6}$$

The $SER_{10,RS}$ compares D_{10} at 4 MV with and without IUdR:

$$SER_{10,RS}(E, \%IUdR) = \frac{D_{10}(4\ MV, 0\%\ IUdR)}{D_{10}(4\ MV, \%\ IUdR)}. \tag{4.7}$$

Finally, the $SER_{10,AE}$ can be calculated from the other SER_{10} values by:

$$SER_{10,AE}(E, \%IUdR) = \frac{SER_{10,T}(E, \%IUdR)}{SER_{10,LET}(E, \%IUdR) * SER_{10,RS}(E, \%IUdR)}$$

$$= \frac{D_{10}(4\ MV, \%IUdR)}{D_{10}(4\ MV,\ 0\%\ IUdR)} * \frac{D_{10}(E,\ 0\%\ IUdR)}{D_{10}(E, \%IUdR)}. \tag{4.8}$$

To calculate $SER_{10,AE}$(E, %IUdR), certain assumptions were made. Because $SER_{10,LET}$(E, %IUdR) describes the impact that the quality of the radiation has on cell killing while $SER_{10,RS}$(E, %IUdR) describes the biological effect that IUdR has on cell repair, $SER_{10,LET}$ and

$SER_{10,RS}$ for the experimental condition (4 MV, 0%IUdR) were defined as unity because these were the chosen reference conditions. Because there is no significant Auger effect elicited at 4 MV since most interactions are governed by the Compton effect, $SER_{10,AE}$(4 MV, %IUdR) was also considered to be unity. $SER_{10,LET}$ value is a result of the energy used for irradiation compared to 4 MV, so $SER_{10,LET}$ is the same for each energy, regardless of the concentration of IUdR present in the cells, i.e., $SER_{10,LET}$(E, %IUdR) = $SER_{10,LET}$(E, 0% IUdR). $SER_{10,RS}$ is a result of the %IUdR in the cells, independent of the energy used to irradiate them, i.e., $SER_{10,RS}$(E, %IUdR) = $SER_{10,RS}$(4 MV, %IUdR).

The uncertainties in Equations (4.5)–(4.8) were determined by propagating independent errors. For $SER_{10,T}$(E, %IUdR):

$$\sigma_{SER_{10,T}} = SER_{10,T}\sqrt{\left[\frac{\sigma_{D_{10}}(4\,MV, 0\%\,IUdR)}{D_{10}(4\,MV, 0\%\,IUdR)}\right]^2 + \left[\frac{\sigma_{D_{10}}(E, \%IUdR)}{D_{10}(E, \%IUdR)}\right]^2}. \tag{4.9}$$

For $SER_{10,LET}$(E, % IUdR):

$$\sigma_{SER_{10,LET}} = SER_{10,LET}\sqrt{\left[\frac{\sigma_{D10}(4\,MV, 0\%\,IUdR)}{D_{10}(4\,MV, 0\%\,IUdR)}\right]^2 + \left[\frac{\sigma_{D10}(E, 0\%\,IUdR)}{D_{10}(E, 0\%\,IUdR)}\right]^2} \tag{4.10}$$

For $SER_{10,RS}$(E, % IUdR):

$$\sigma_{SER_{10,RS}} = SER_{10,RS}\sqrt{\left[\frac{\sigma_{D10}(4\,MV, 0\%\,IUdR)}{D_{10}(4\,MV, 0\%\,IUdR)}\right]^2 + \left[\frac{\sigma_{D10}(4\,MV, \%\,IUdR)}{D_{10}(4\,MV, \%\,IUdR)}\right]^2} \tag{4.11}$$

Finally, for $SER_{10,AE}$(E, % IUdR):

$$\sigma_{SER_{10,AE}} = SER_{10,AE}\sqrt{\begin{aligned}&\left[\frac{\sigma_{D10}(4\,MV, 0\%\,IUdR)}{D_{10}(4\,MV, 0\%\,IUdR)}\right]^2 + \left[\frac{\sigma_{D10}(4\,MV, \%\,IUdR)}{D_{10}(4\,MV, \%\,IUdR)}\right]^2 + \\ &+\left[\frac{\sigma_{D10}(E,\ 0\%\,IUdR)}{D_{10}(E, 0\%\,IUdR)}\right]^2 + \left[\frac{\sigma_{D10}(E, \%\,IUdR)}{D_{10}(E, \%\,IUdR)}\right]^2\end{aligned}} \tag{4.12}$$

4.3 Results

4.3.1 Analysis of 4 MV Data

The 4MV irradiations comprised the largest number of data sets. The (4 MV, 0% IUdR) data served as the reference for all other experimental conditions. Figure 4.3(a)-(c) show the curve-fits for each level of %IUdR and Figure 4.3(d) compares the three curve-fits. The shoulders of the curves increasingly bend as the %IUdR increases, thus, decreasing the D_{10} values.

Table 4.3 and Table 4.4 report the survival curve results, including fit parameters, reduced chi-squared values, D_{10} values and SER_{10} values for the 4 MV irradiations at 0%, 9%, and 18% IUdR. Since (4 MV, 0% IUdR) is the reference experimental condition, by definition $SER_{10,T}$(4 MV, 0% IUdR) = 1.00. Note that $SER_{10,RS}$(E, 9% IUdR) = $SER_{10,T}$(4 MV, 9% IUdR) = 1.28 ± 0.02 and $SER_{10,RS}$(E, 18% IUdR) = $SER_{10,T}$(4 MV, 18% IUdR) = 1.40 ± 0.02, as a result of the radiosensitizing properties of IUdR.

4.3.2 Analysis of 35 keV Data

Experimental conditions (35 keV, %IUdR) were the most significant data sets in that these showed the greatest Auger effect, 35 keV being just above the K-edge of iodine. Figure 4.4(a)-(c) show the curve-fits for each level of %IUdR and Figure 4.4(d) compares the three curve-fits. The shoulders of the curves disappear as the %IUdR increases, thus, decreasing the D_{10} values.

Table 4.3 and Table 4.4 report the survival curve results, including fit parameters, reduced chi-squared values, D_{10} values and SER_{10} values for the 35 keV irradiations at 0%, 9%, and 18% IUdR. The value $SER_{10,T}$(35 keV, 0% IUdR) = $SER_{10,LET}$(35 keV, % IUdR) = 1.08 ±

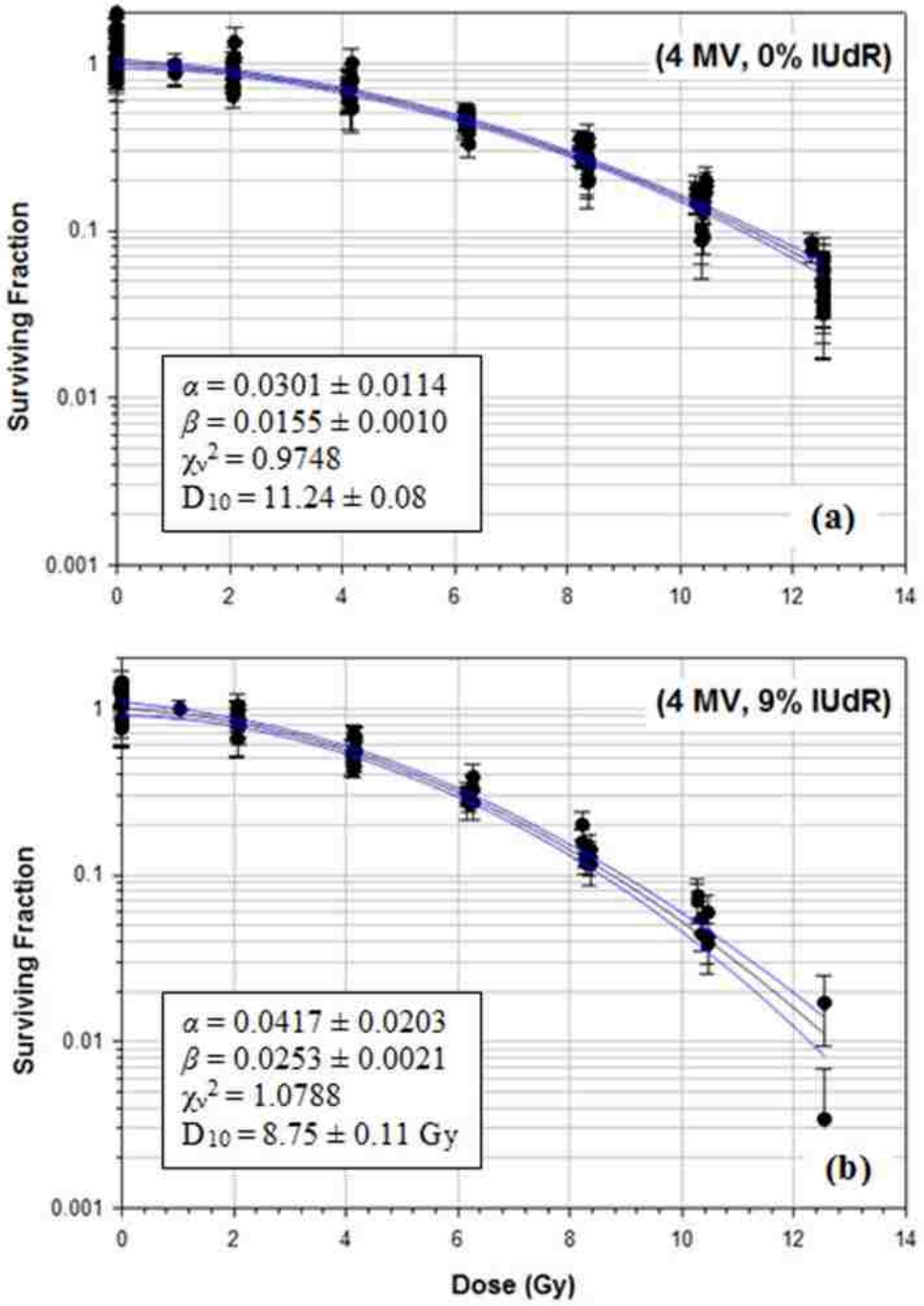

Figure 4.3: Fits to cell survival data at 4 MV for 0%, 9%, and 18% IUdR. The black line represents the curve fit; blue lines represent the 95% confidence interval. Plot of (a) (4 MV, 0% IUdR) data from 148 data points, (b) (4 MV, 9% IUdR) data from 62 data points, and (c) (4 MV, 18% IUdR) data from 93 data points. (d) Comparison of resulting curve-fits for 4MV x-rays and 0%, 9%, and 18% IUdR.

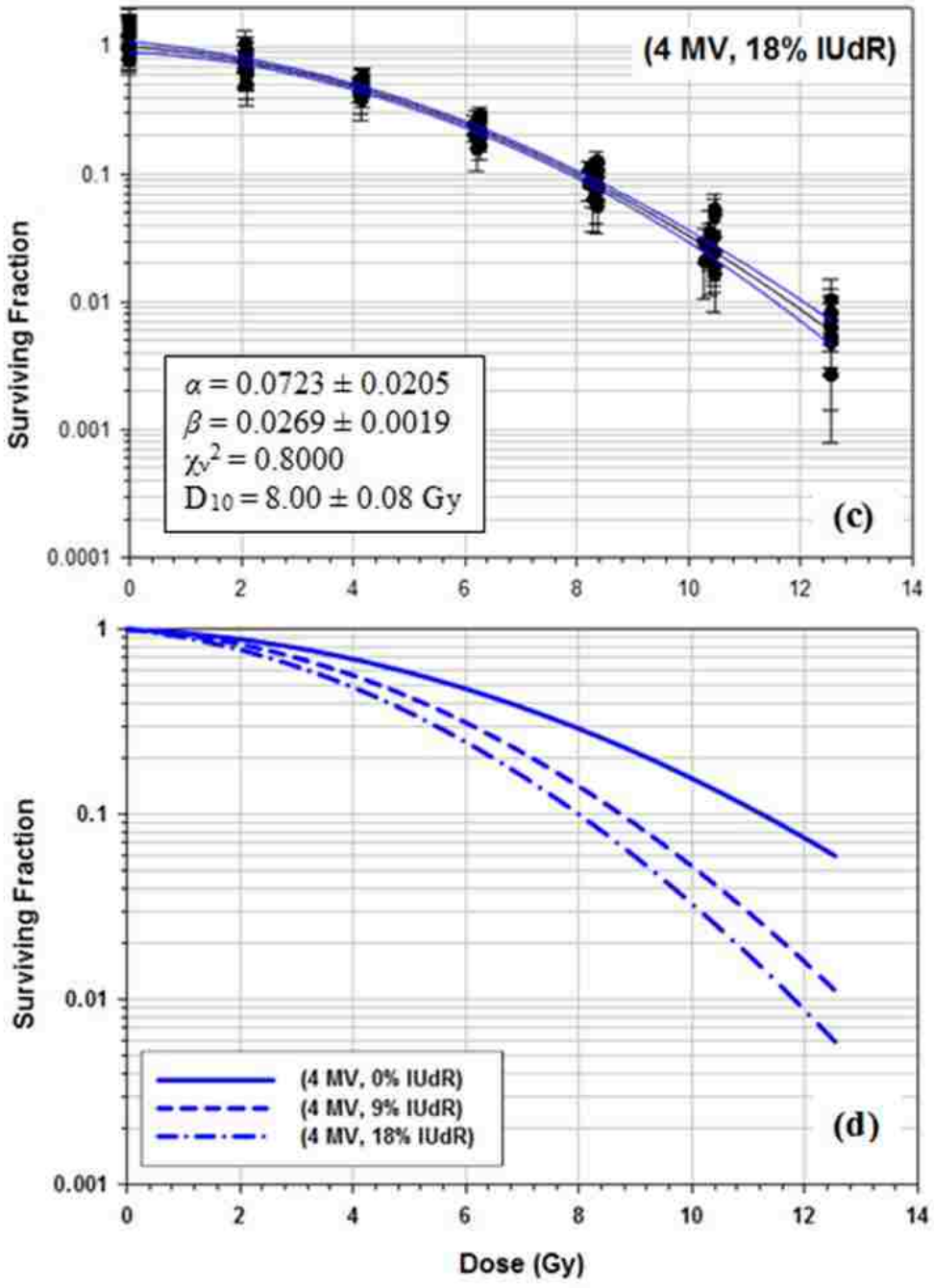

Figure 4.3 (continued)

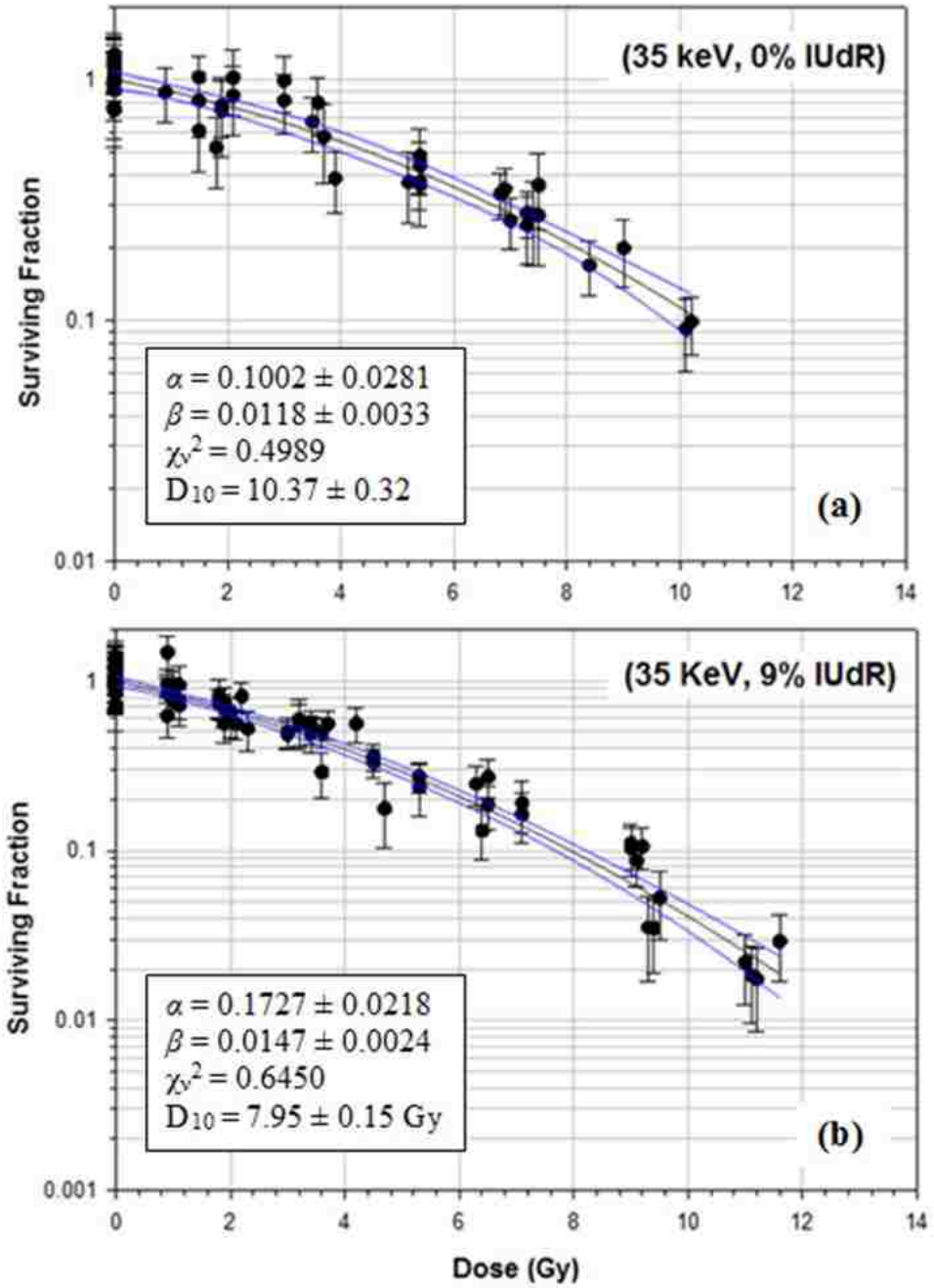

Figure 4.4: Fits to cell survival data at 35 keV for 0%, 9%, and 18% IUdR. The black line represents the curve fit; blue lines represent the 95% confidence interval. Plot of (a) (35 keV, 0% IUdR) data from 47 data points, (b) (35 keV, 9% IUdR) data from 83 data points, and (c) (35 keV, 18% IUdR) data from 62 data points. (d) Comparison of resulting curve-fits for 35 keV x-rays and 0%, 9%, and 18% IUdR.

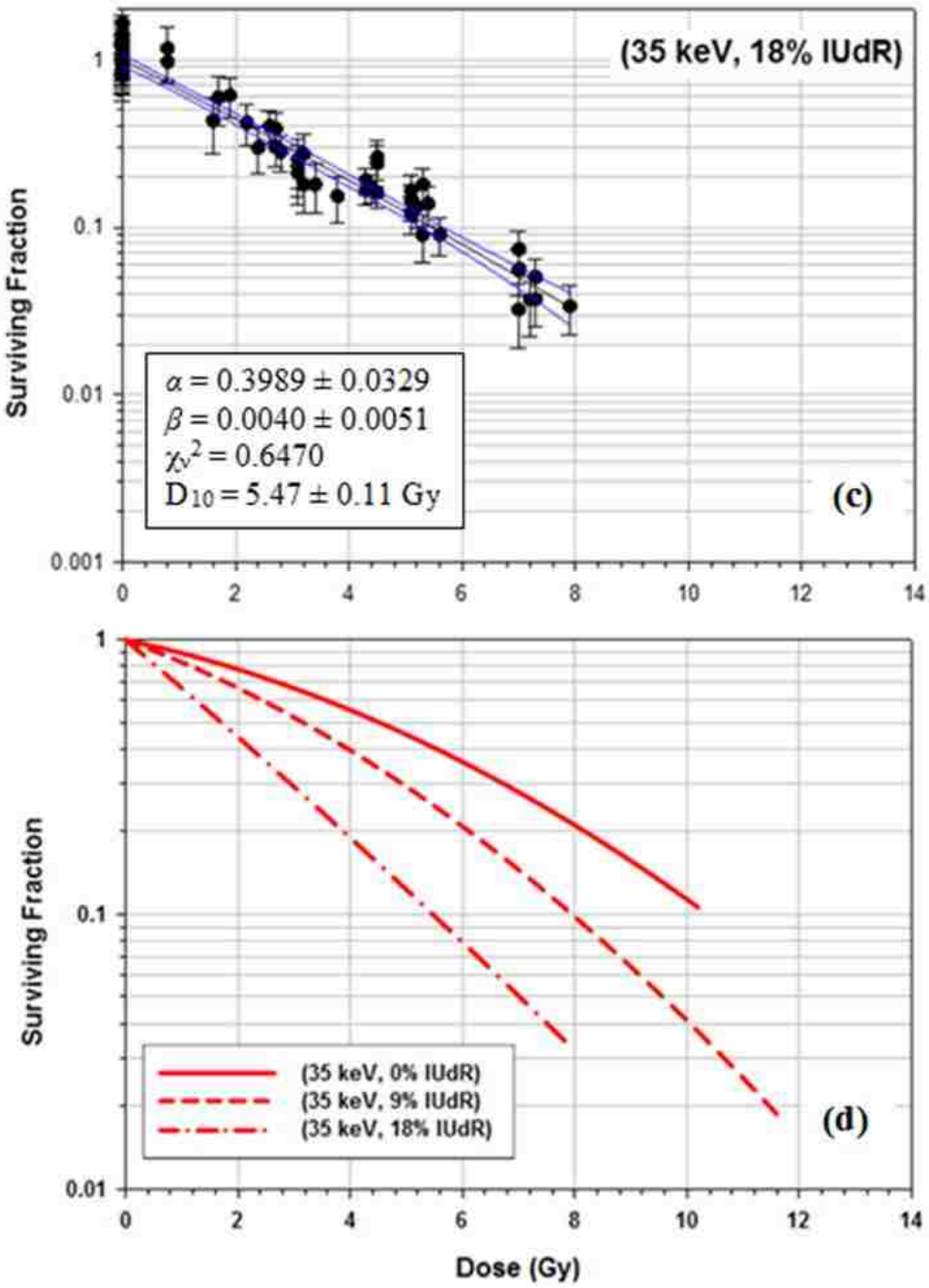

Figure 4.4 (continued)

0.03, reflects the therapeutic gain completely attributed to the higher relative biological effect (RBE) of the higher LET, lower energy electrons created by 35 keV photons as opposed to those of 4 MV x-rays. The values $SER_{10,T}$(35 keV, 9% IUdR) = 1.41 ± 0.03 and $SER_{10,T}$(35 keV, 18%

IUdR) = 2.05 ± 0.04 are attributed to a combination of the LET effect, radiosensitization of IUdR, and the Auger effect. The Auger contributions to the sensitization enhancement ratio were calculated to be $SER_{10,AE}$(35 keV, 9% IUdR) = 1.01 ± 0.04 and $SER_{10,AE}$(35 keV, 18% IUdR) = 1.35 ± 0.05.

4.3.3 Analysis of 30 keV Data

Experimental conditions (30 keV, %IUdR) were data that was designed to detect any Auger effect due to L-edge photoelectric interactions, as 30 keV is below the K-edge of iodine. Figure 4.5(a)-(b) show the curve-fits for each level of %IUdR and Figure 4.5(c) compares the two curve-fits. The shoulder of the 18% IUdR curve bent compared to the 0% IUdR curve, thus, decreasing its D_{10} value.

Table 4.3 and Table 4.4 report the survival curve results, including fit parameters, reduced chi-squared values, D_{10} values and SER_{10} values for the 30 keV irradiations at 0% and 18% IUdR. The value $SER_{10\%,T}$(30 keV, 0% IUdR) = $SER_{10\%,LET}$(30 keV, % IUdR) = 1.22 ± 0.02, reflects the therapeutic gain completely attributed to the higher RBE of the lower energy, higher LET electrons created by 30 keV photons as opposed to those of 4 MV x-rays. The value $SER_{10\%,T}$(30 keV, 18% IUdR) = 1.82 ± 0.04 is attributed to a combination of the LET effect, radiosensitization of IUdR, and the Auger effect. The Auger contribution to the sensitization enhancement ratio was $SER_{10,AE}$(30 keV, 18% IUdR) = 1.06 ± 0.03.

4.3.4 Analysis of 25 keV Data

Experimental conditions (25 keV, %IUdR) provided data that were designed to detect any Auger effect as a result of L-edge photoelectric interactions, as again 25 keV is below the K-edge of iodine. Figure 4.6(a)-(c) show the curve-fits for each level of %IUdR and Figure 4.6(d)

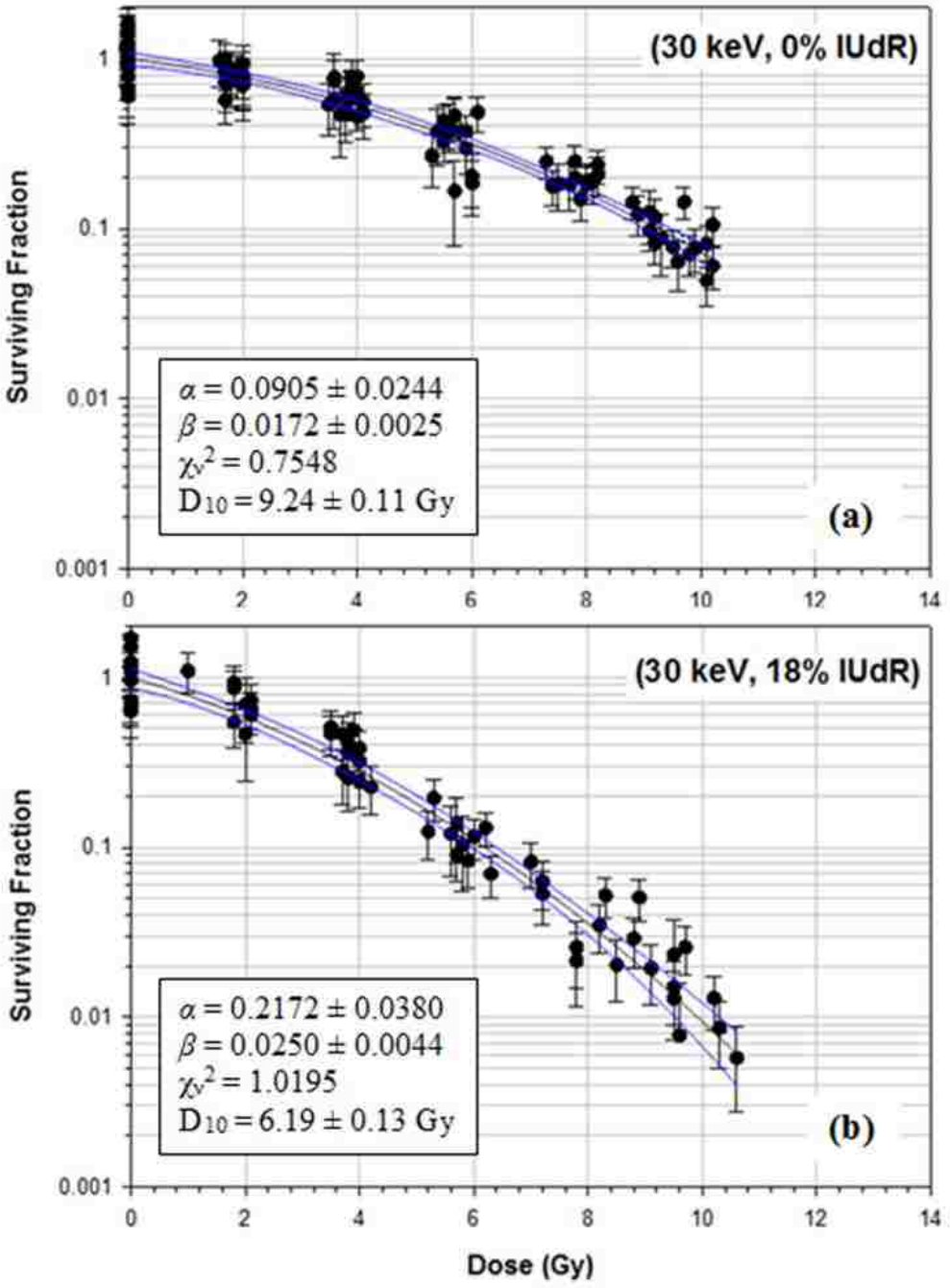

Figure 4.5: Fits to cell survival data at 30 keV for 0% and 18% IUdR. The black line represents the curve fit; blue lines represent the 95% confidence interval. Plot of (a) (30 keV, 0% IUdR) data from 97 data points and (b) (30 keV, 18% IUdR) data from 62 data points. (c) Comparison of resulting curve-fits for 30 keV x-rays and 0% and 18% IUdR.

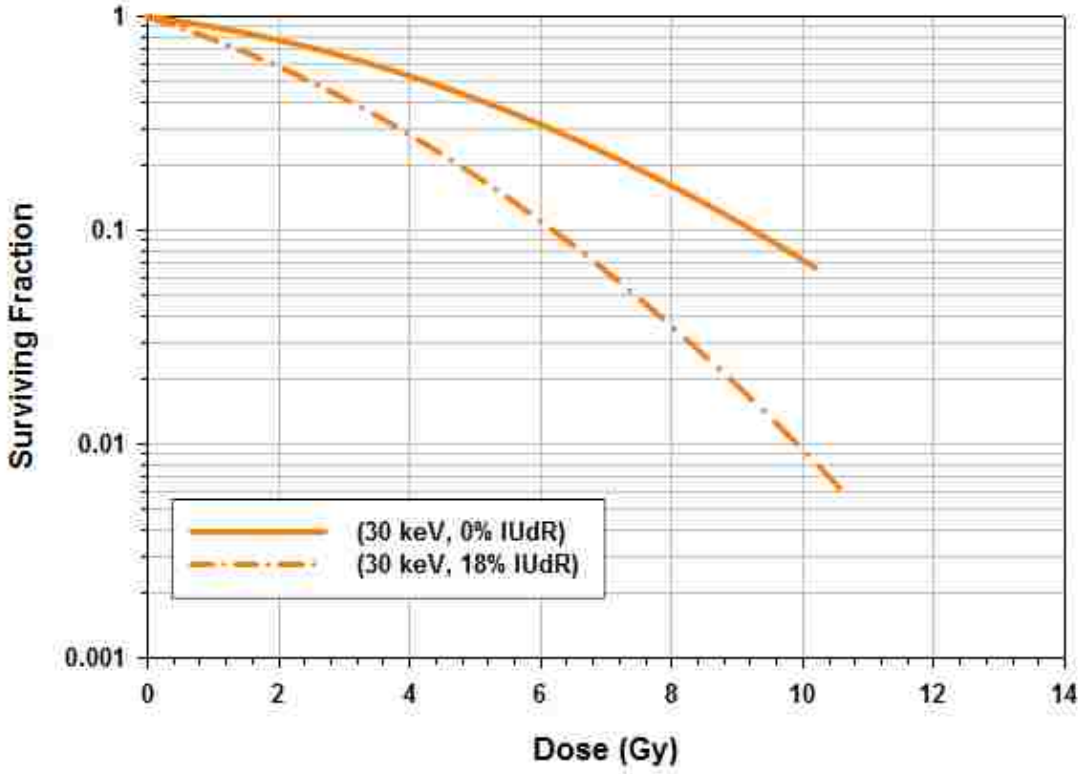

Figure 4.5 (continued)

compares the three curve-fits. The curves for 0 and 9% IUdR somewhat overlap each other between 0 and ~7 Gy, hinting that 9% IUdR did not elicit a radiosensitizing effect in this dose range. At doses > 7 Gy, a small decrease in the curvature of the 9% IUdR curve was present. Comparing these two curves to that of 18% IUdR, the familiar bending in the shoulder of the curve is present with the increase of %IUdR, thus, decreasing the D_{10} value for 18% IUdR.

Table 4.3 and Table 4.4 report the survival curve results, including fit parameters, reduced chi-squared, D_{10} values and SER_{10} values for the 25 keV irradiations at 0%, 9%, and 18% IUdR. The value $SER_{10\%,T}$(25 keV, 0% IUdR) = $SER_{10\%,LET}$(25 keV, 0% IUdR) = 1.37 ± 0.02, reflects the therapeutic gain completely attributed to the higher RBE of the lower energy, higher LET electrons created by 25 keV as opposed to those of 4 MV x-rays. The values $SER_{10\%,T}$(25 keV, 9% IUdR) = 1.44 ± 0.03 and $SER_{10,T}$(25 keV, 18% IUdR) = 1.90 ± 0.04 were

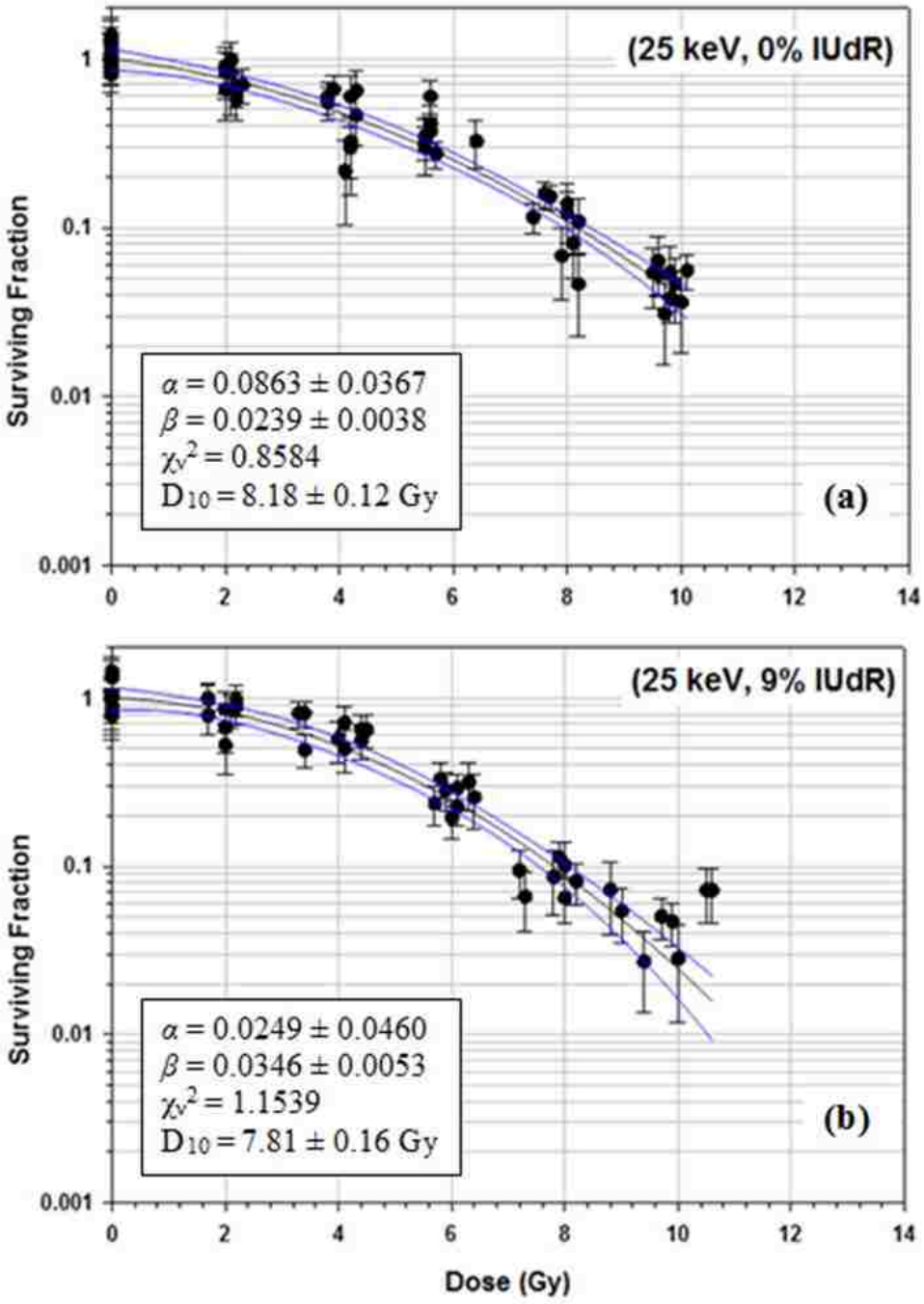

Figure 4.6: Fits to cell survival data at 25 keV for 0%, 9%, and 18% IUdR. The black line represents the curve fit; blue lines represent the 95% confidence interval. Plot of (a) (25 keV, 0% IUdR) data from 53 data points, (b) (25 keV, 9% IUdR) data from 50 data points, and (c) (25 keV, 18% IUdR) data from 69 data points. (d) Comparison of resulting curve-fits for 25 keV x-rays and 0%, 9%, and 18% IUdR.

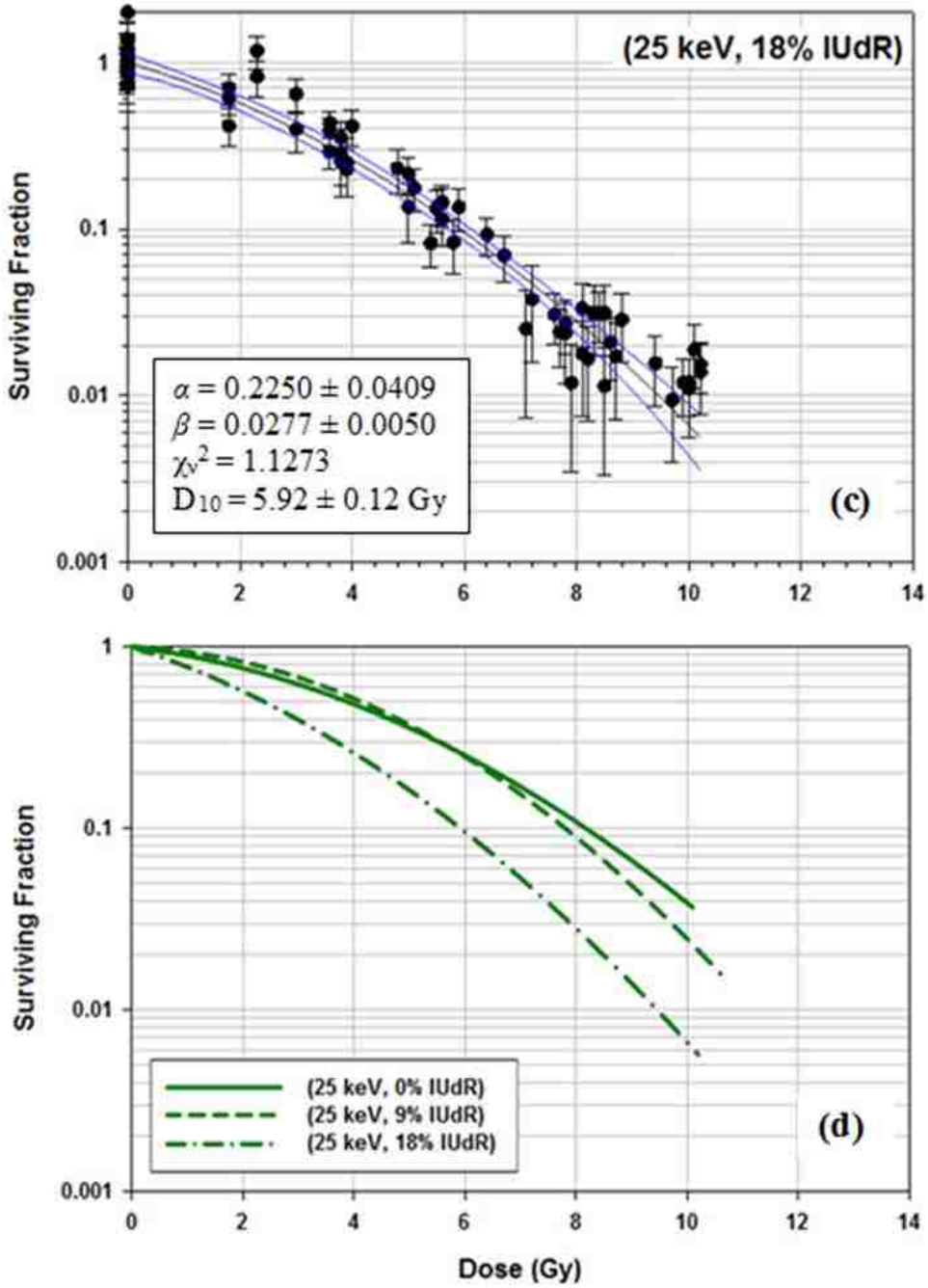

Figure 4.6 (continued)

attributed to a combination of the LET effect and radiosensitization of IUdR. The Auger effect was $SER_{10,AE}$(25 keV, 9% IUdR) = 0.82 ± 0.02 and $SER_{10,AE}$(25 keV, 18% IUdR) = 0.98 ± 0.03.

4.3.5 Summary of Results

Table 4.3 summarizes values for the $\alpha \pm \sigma_\alpha$ and $\beta \pm \sigma_\beta$ parameters, where σ_α and σ_β are standard errors, reduced chi-squared values, and $D_{10} \pm \sigma_{D10}$ for all experimental conditions (E, %IUdR) resulting from chi-squared fitting the *SF* versus *D* data to $A * e^{-\alpha * D - \beta * D^2}$ for all combinations of energies (4 MV, 25 keV, 30 keV, 35 keV) and %IUdR (0%, 9%, 18%).

Table 4.4 shows values for SER_{10}(E, %IUdR) $\pm$ σ resulting from the calculated D_{10} values, broken down into its LET, RS, and AE contributions.

4.4 Discussion

4.4.1 4 MV Survival Curves

The (4 MV, 0% IUdR) survival curve (D_{10} = 11.2 $\pm$ 0.08 Gy) is comparable to the radiation survival curve ($D_{10} \approx$ 10.8 Gy) of rat 9L glioma cells reported by Franko *et al.* (1992). This result builds confidence in the (4 MV, 0% IUdR) data as a reference for comparison to other experimental conditions tested in this project.

4.4.2 The LET Effect of 25-35 keV Monochromatic X-Rays

Figure 4.7 plots the dose-survival curves and lists the $SER_{10,LET}$ values for cells without IUdR irradiated using 4 MV x-rays, and 35 keV, 30 keV and 25 keV. The RBE for rat 9L glioma cells increased as photon energy decreased (from 1.08 at 35 keV to 1.37 at 25 keV) due to the increased LET of electrons produced by low energy x-rays. Lower energy x-rays required less dose to achieve 90% cell killing than higher energy x-rays. Dugas *et al.* (2011) reported no LET effect for CHO cells. However, it is possible that their utilization of a less sophisticated curve fitting method than used in this work might have hidden the LET effect observed in this study.

Table 4.3: Summary of results for all experimental conditions (E, %IUdR). The number of data sets and data points, α and β parameters and their associated standard errors, D_{10} values and their associated standard errors, and reduced chi-squared values (χ_v^2) are shown for each (E, %IUdR).

Energy	% IUdR	*R* Data Sets	*N* Data Points	Number of Outliers	$\alpha \pm \sigma_\alpha$	$\beta \pm \sigma_\beta$	χ_v^2	$D_{10} \pm \sigma_{D10}$ (Gy)
4 MV	0%	13	148	2	0.0301 ± 0.0114	0.0155 ± 0.0010	0.9748	11.24 ± 0.08
	9%	4	62	1	0.0417 ± 0.0203	0.0253 ± 0.0021	1.0788	8.75 ± 0.11
	18%	5	93	2	0.0723 ± 0.0205	0.0269 ± 0.0019	0.8000	8.00 ± 0.08
35 keV	0%	6	47	1	0.1002 ± 0.0281	0.0118 ± 0.0033	0.4989	10.37 ± 0.32
	9%	9	83	0	0.1727 ± 0.0218	0.0147 ± 0.0024	0.6450	7.95 ± 0.15
	18%	7	62	0	0.3989 ± 0.0329	0.0040 ± 0.0051	0.6470	5.47 ± 0.11
30 keV	0%	6	97	1	0.0905 ± 0.0244	0.0172 ± 0.0025	0.7548	9.24 ± 0.11
	18%	4	62	1	0.2172 ± 0.0380	0.0250 ± 0.0044	1.0195	6.19 ± 0.13
25 keV	0%	3	53	0	0.0863 ± 0.0367	0.0239 ± 0.0038	0.8584	8.18 ± 0.12
	9%	4	50	4	0.0249 ± 0.0460	0.0346 ± 0.0053	1.1539	7.81 ± 0.16
	18%	5	69	3	0.2250 ± 0.0409	0.0277 ± 0.0050	1.1273	5.92 ± 0.12

Table 4.4: Summary of calculated SER_{10} values for all experimental conditions (E, %IUdR). The components of $SER_{10,T}$ (LET, RS, and AE contributions) are listed.

Energy/ % IUdR	$D_{10} \pm \sigma_{D10}$ (Gy)	$SER_{10,T}$	$SER_{10,LET}$	$SER_{10,RS}$	$SER_{10,AE}$
4 MV					
0	11.2 ± 0.08	1.00	1.00	1.00	1.00
9	8.7 ± 0.11	1.28 ± 0.02	1.00	1.28 ± 0.02	1.00 ± 0.02
18	8.0 ± 0.08	1.40 ± 0.02	1.00	1.40 ± 0.02	1.00 ± 0.02
35 keV					
0	10.4 ± 0.32	1.08 ± 0.03	1.08 ± 0.03	1.00	1.00 ± 0.04
9	8.0 ± 0.15	1.41 ± 0.03	1.08 ± 0.03	1.28 ± 0.02	1.01 ± 0.04
18	5.5 ± 0.11	2.05 ± 0.04	1.08 ± 0.03	1.40 ± 0.02	1.35 ± 0.05
30 keV					
0	9.2 ± 0.11	1.22 ± 0.02	1.22 ± 0.02	1.00	1.00 ± 0.02
18	6.2 ± 0.13	1.82 ± 0.04	1.22 ± 0.02	1.40 ± 0.02	1.06 ± 0.03
25 keV					
0	8.2 ± 0.12	1.37 ± 0.02	1.37 ± 0.02	1.00	1.00 ± 0.02
9	7.8 ± 0.16	1.44 ± 0.03	1.37 ± 0.02	1.28 ± 0.02	0.82 ± 0.02
18	5.9 ± 0.12	1.90 ± 0.04	1.37 ± 0.02	1.40 ± 0.02	0.98 ± 0.03

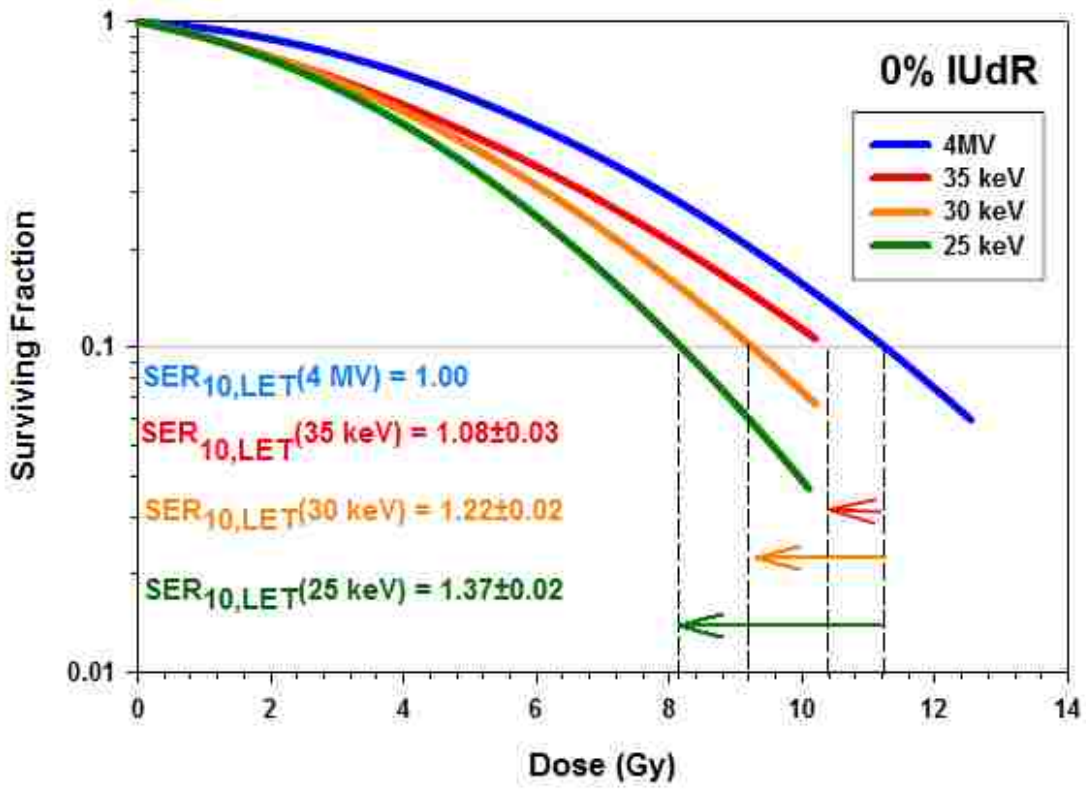

Figure 4.7: Survival curves for rat 9L glioma cells with 0% IUdR. Irradiation energies were 4 MV, 35 keV, 30 keV, and 25 keV. $SER_{10,LET}$ increased as the energy decreased.

The RBE values listed in Table 4.5 and plotted in Figure 4.8 (Spadinger & Palcic 1992, Hoshi *et al.* 1988, Nath *et al.* 1987, Bistrovic *et al.* 1986) were measured in different cell lines, such as Chinese hamster ovary (CHO), Chinese hamster fibroblast (V79), and Chinese hamster (CH) lung cells. Nonetheless, the trend of RBE values, which are influenced by many factors, including the radiosensitivity of the various cell lines, in general decreased with increasing effective energy (decreasing LET). The authors either reported an effective energy or a half-value layer for their x-ray beams; for the half-value layers, effective energies were determined by interpolation using a table of attenuation coefficients (Hubbell & Seltzer 2004) for the attenuating material.

Table 4.5: Comparison of RBE values as a function of effective energy for previously published cell irradiation data. Values highlighted are from the present study.

Beam Energy/Quality	E_{eff} (keV)	RBE	Reference Radiation	Cell Line	Reference
250 kVp (0.35 mm Cu + 0.40 mm Sn filter)	122†	1.1 ± 0.05	Co-60	V79	Spadinger & Palcic 1992
		1.1 ± 0.04	Co-60	CHO	Spadinger & Palcic 1992
180 kVp (0.5 mm Al filter)	90	1.29	Co-60	V79	Hoshi et al. 1988
250 kVp (0.3 mm Cu HVL)	48†	1.15	4 MV	CH Lung	Nath et al. 1987
35 keV (3.00 cm Al HVL)	35	1.08 ± 0.03	4 MV	9L glioma	Present work
30 keV (2.34 cm Al HVL)	30	1.22 ± 0.02	4 MV	9L glioma	Present work
70 kVp (1.5 mm Al HVL)	26†	1.19 ± 0.06	Co-60	V79	Bistrovic et al. 1986
25 keV (1.76 cm Al HVL)	25	1.37 ± 0.02	4 MV	9L glioma	Present work
55 kVp (1 mm Be + 0.78 mm Al filter)	25†	1.0 ± 0.07	Co-60	V79	Spadinger & Palcic 1992
		1.2 ± 0.05	Co-60	CHO	Spadinger & Palcic 1992
50 kVp (0.65 mm Al HVL)	19	1.56	Co-60	V79	Hoshi et al. 1988
20 kVp (0.15 mm Al HVL)	12†	1.40 ± 0.07	Co-60	V79	Bistrovic et al. 1986
40 kVp (0.16 mm Al HVL)	12	1.62	Co-60	V79	Hoshi et al. 1988
40 kVp (no filter)	8	1.50	Co-60	V79	Hoshi et al. 1988

† Effective energy determined by interpolation from tables of attenuation coefficients (Hubbell & Seltzer 2004).

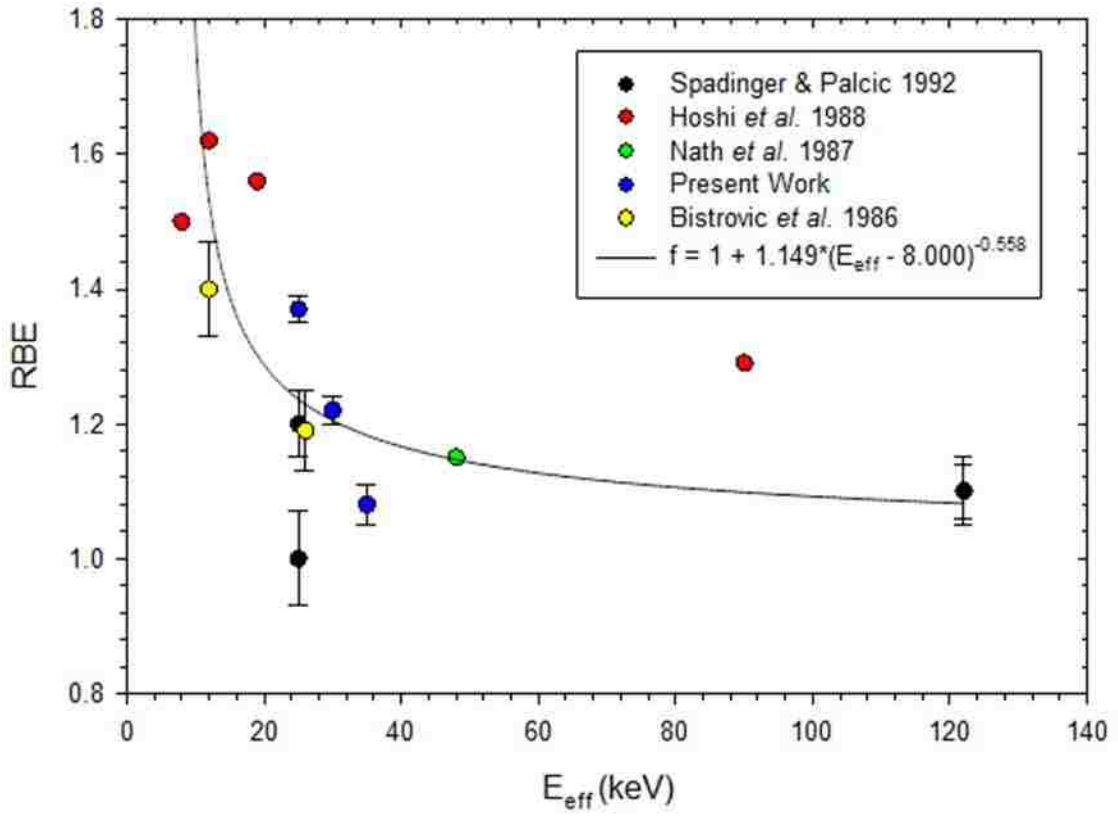

Figure 4.8: Plot of RBE values as a function of effective energy (keV). Data were measured in previously published data (see Table 4.5), except the blue circles (this work's data). The curve-fit ($f = 1 + 1.149*(E_{eff} - 8.000)^{0.558}$) is for guiding the eye to follow the trend of the data.

4.4.3 IUdR as a Radiosensitizer

Figure 4.9 shows the survival curves for 4 MV irradiated 9L cells containing 0%, 9%, and 18% IUdR. 9L cells experienced 28% and 40% increases in cell killing when they contained 9% and 18% IUdR, respectively.

The $SER_{10,RS}$ for (4 MV, 9% IUdR) and (4MV, 18% IUdR) were 1.28 ± 0.02 and 1.40 ± 0.02, respectively, compared to 1.5 ± 0.1 and 2.6 ± 0.1 for CHO cells with 9% and 17% IUdR, as reported in Dugas *et al.* (2011). The radiosensitization effect of IUdR was less in 9L cells than in CHO cells, possibly because 9L cells have superior capabilities to repair. Bencokova *et al.* (2008) observed via immunofluorescence that the DSB repair rate of 9L cells was fast and complete with all DSBs repaired in 15 hours after receiving a 2 Gy dose.

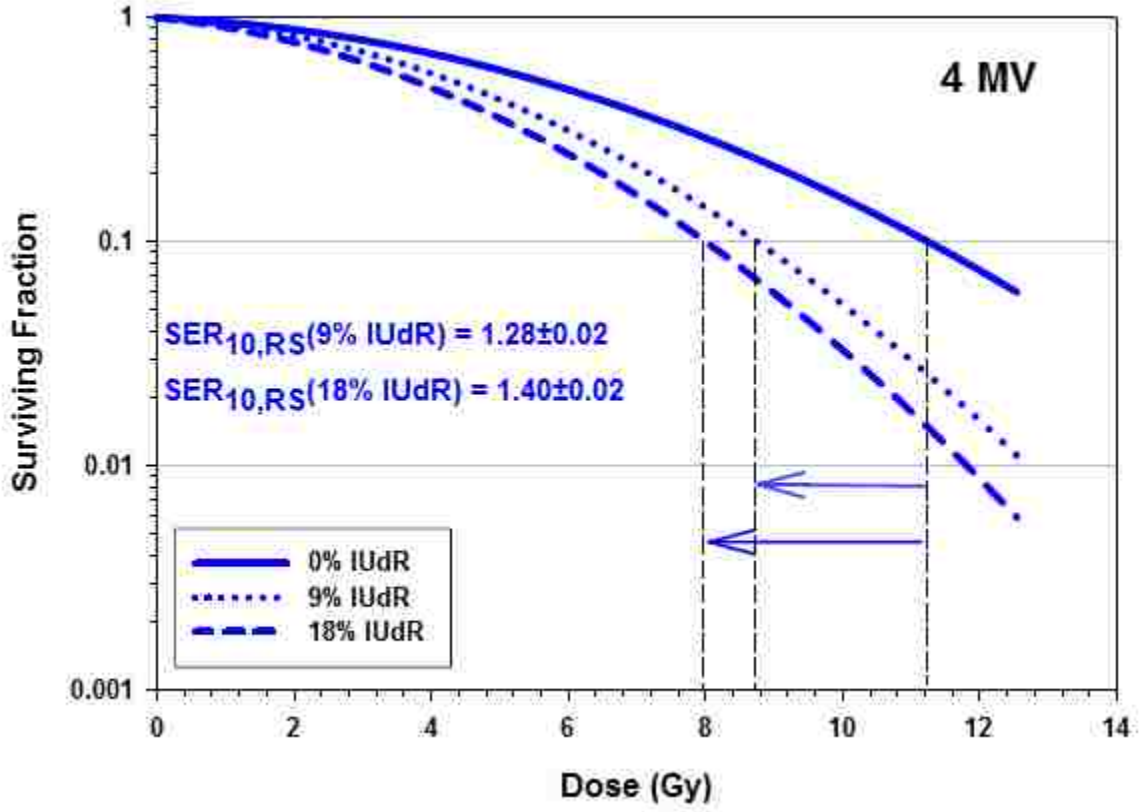

Figure 4.9: Survival curves for 4 MV and 0%, 9%, and 18% IUdR. $SER_{10,RS}$(4 MV, %IUdR) increased as %IUdR increased.

4.4.4 The Auger Effect

Table 4.6 lists $SER_{10,T}$, $SER_{10,LET}$, $SER_{10,RS}$, and $SER_{10,AE}$ values for 35 keV irradiations for this work and extracted from Dugas *et al.* (2011). The $SER_{10,T}$ for 9L cells irradiated under the experimental conditions (35 keV, 9% IUdR) and (35 keV, 18% IUdR) were 1.41 ± 0.03 and 2.05 ± 0.04, respectively, compared to 2.0 ± 0.1 and 4.1 ± 0.2 for CHO cells under the experimental conditions (35 keV, 9% IUdR) and (35 keV, 17% IUdR), respectively.

Table 4.6: Comparison of SER_{10} values for rat 9L glioma and CHO cells, irradiated at 35 keV energy. CHO data is from Dugas *et al.* (2011).

SER_{10}(E, %IUdR)	Rat 9L Glioma Cells		CHO cells	
	9% IUdR	18% IUdR	9% IUdR	17% IUdR
$SER_{10,T}$ (35 keV, %IUdR)	1.40±0.03	2.03±0.04	2.0±0.1	4.1±0.2
$SER_{10,LET}$(35 keV, %IUdR)	1.07±0.03	1.07±0.03	1.0	1.0
$SER_{10,RS}$(35 keV, %IUdR)	1.28±0.02	1.40±0.02	1.5±0.1	2.6±0.1
$SER_{10,AE}$(35 keV, %IUdR)	1.01±0.04	1.35±0.05	1.3±0.1	1.6±0.1

9L cells are more radioresistant at 35 keV compared to CHO cells, as demonstrated by smaller $SER_{10,RS}$ values. 9L cells did not experience a significant Auger effect at the 9% IUdR level, while CHO cells exhibited a therapeutic gain of 30% due to the Auger effect alone. At the 18% IUdR level, 9L cells had therapeutic gain of 35% while at the 17% IUdR level, CHO cells had a 60% therapeutic gain due to Auger electrons. Clearly, the magnitude of the Auger effect depends on both cell line and amount of IUdR uptake. It is possible that the initial number of DSBs and repair mechanisms may be different between the two cells lines, a potential area for further investigation.

At 18% IUdR for 30 keV and 25 keV, respectively, approximately 3.9 and 4.5 photoelectric events per 2 Gy dose were expected as compared to 20.1 at 35 keV according to Karnas *et al.* (2001) (see Table 1.4). To first order, assume that the expected $SER_{10,AE} = 1 + x$, where x is proportional to the number of photoelectric events at the D_{10} dose level, i.e.,:

$$x = (SER^{m}_{10,AE} - 1) * \frac{\left[\frac{\#PE\ events}{2\ Gy} * D^{m}_{10}\right]_{E,18\%\ IUdR}}{\left[\frac{\#PE\ events}{2\ Gy} * D^{m}_{10}\right]_{35\ keV,18\%\ IUdR}}, \tag{4.13}$$

(*m* stands for "measured"). Hence, the expected $SER_{10,AE}$ were estimated to be approximately 1.08 for either 30 keV or 25 keV. Data showed $SER_{10,AE}$(30 keV, 18%) = 1.06 ± 0.03 and $SER_{10,AE}$(25 keV, 18% IUdR) = 0.98. The result at 30 keV is consistent, however, the result at 25 keV is somewhat inconsistent with expectations for which there is no apparent explanation. Systematic errors in the dosimetry cannot be the cause for this inconsistency since they would divide out in Equation (4.8).

Using a similar analysis as in Equation (4.13) for 9% IUdR, $SER_{10,AE}$ values of 1.26 and 1.06 would be expected at 35 keV and 25 keV, respectively. However, values of 1.01 ± 0.04 and 0.82 ± 0.02, respectively, were observed. Although significantly different, their ratios of 1.19 (1.26/1.06) and 1.23 (1.01/0.82) are similar.

At 35 keV, an $SER_{10,AE}$(18% IUdR) value of 1.35 ± 0.05 was observed. Although lower than what was observed for CHO by Dugas *et al.* (2011), it is equally important since the radiosensitization effect is less in 9L cells compared to CHO cells. At the 9% IUdR level, the expected $SER_{10,AE}$ for 35 keV was estimated to first order to be 1.18:

$$\begin{aligned} &1 + 0.5 * \left[SER_{10,AE}(35\ keV, 18\%\ IUdR) - 1\right] \\ &= 1 + 0.5 * (1.35 - 1) = 1.18. \end{aligned} \tag{4.14}$$

Hence, the measured $SER_{10,AE}$(35 keV, 9% IUdR) value of 1.01 ± 0.04 is less than what was expected. Of question is whether the value of $SER_{10,RS}$ (35 keV, 9% IUdR) = 1.28 ± 0.02 is too high, masking the Auger effect.

The results of 0% and 18% IUdR in 9L cells at 30 keV and 35 keV can be compared with those of Corde *et al.* (2004) (10−20% IUdR in SQ20B cells) at 32.8 and 33.5 keV, i.e., a

comparison slightly below and above the K-edge of iodine (33.2 keV). The SER_{10} values, computed as:

$$SER_{10} = \frac{D_{10}(E, 0\%\ IUdR)}{D_{10}(E, \%IUdR)}, \tag{4.15}$$

for energies 30 keV and 35 keV are 1.48 ± 0.04 and 1.89 ± 0.07, respectively. The SER_{10} ratio of 35 keV: 30keV is 1.28 ± 0.06, which compares well with Corde's *et al.* SER_{10} ratio of 1.31 (SER_{10} values of 1.25 and 1.64 for 32.8 keV and 33.5 keV, respectively).

Corde's *et al.* survival curves with 0% IUdR have a shoulder at 50 keV and 70 keV, as expected, however, show no shoulder at 32.8 keV and 33.5 keV where expected, nor for 10-20% IUdR at 32.8 keV where expected (see Figure 1.10). Contrastingly, this work's survival curves at (35 keV, 0% IUdR), (30 keV, 0% IUdR), and (30 keV, 18% IUdR) all show shoulders. Furthermore, there is no reason to expect the SER_{10} values at 50 keV (2.62) to be greater than that at 33.5 keV (1.64) as reported in Corde *et al.*, because Karnas *et al.* (2001) calculated fewer photoelectric events at 50 keV (13.3) than at 33.2 keV (20.8). Therein lies the need to either confirm or refute Corde's *et al.* data from 40-70 keV.

An alternative to the $SER_{10,AE}$ calculation shown in Equation (4.8) is to calculate the ratio of D_{10} values for an energy slightly above and below the K-edge, which is the more common method of calculating $SER_{10,AE}$ values (Laster *et al.* 1993). This method can be applied to the present results provided the difference in the LET effect between 35 keV and 30 keV photons is incorporated. Using this alternate method, at (35 keV, 18% IUdR):

$$SER_{10,AE}(35\ keV, 18\%\ IUdR) = \frac{D_{10}(30\ keV, 18\%\ IUdR)}{D_{10}(35\ keV, 18\%\ IUdR)} * \frac{SER_{10,LET}(30\ keV)}{SER_{10,LET}(35\ keV)}$$

$$= \frac{D_{10}(30\ keV, 18\%\ IUdR)}{D_{10}(35\ keV, 18\%\ IUdR)} * \frac{D_{10}(35\ keV, 0\%\ IUdR)}{D_{10}(30\ keV, 0\%\ IUdR)}$$

$$= \left(\frac{6.19}{5.47}\right) * \left(\frac{10.37}{9.24}\right) = 1.27 \pm 0.06. \quad (4.16)$$

Similarly, at (35 keV, 9% IUdR):

$$SER_{10,AE}(35\ keV, 9\%\ IUdR) = \frac{D_{10}(25\ keV, 9\%\ IUdR)}{D_{10}(35\ keV, 9\%\ IUdR)} * \frac{SER_{10,LET}(25\ keV)}{SER_{10,LET}(35\ keV)}$$

$$= \frac{D_{10}(25\ keV, 9\%\ IUdR)}{D_{10}(35\ keV, 9\%\ IUdR)} * \frac{D_{10}(35\ keV, 0\%\ IUdR)}{D_{10}(25\ keV, 0\%\ IUdR)}$$

$$= \left(\frac{7.81}{7.95}\right) * \left(\frac{10.37}{8.18}\right) = 1.25 \pm 0.06. \quad (4.17)$$

As previously, any systematic dosimetric error in the 30 keV or 35 keV dosimetry divide out in Equations (4.16) and (4.17). It is not clear why these values for 18% and 9% IUdR are so close; however, it could be a statistical variation, i.e., values of 1.33 and 1.19 (one sigma larger and smaller for Equations (4.16) and (4.17), respectively) would not be unreasonable.

The 1.27 ± 0.06 value for (35 keV, 18% IUdR) is slightly different than the 1.35 ± 0.05 value determined using Equation (4.8), but the 1.25 ± 0.06 value for (35 keV, 9% IUdR) is significantly different from the 1.01 ± 0.04 value determined using Equation (4.8). The smaller Auger effect at the 18% IUdR level calculated by Equation (4.16) might be partially explained due to the fact that contributions from L-edge Auger electrons by 30 keV photons are not being considered whereas in the thesis method, i.e., Equation (4.8), the effect from Auger electrons from all shells (K-, L-, M-,...) are considered. The large discrepancy at the 9% IUdR level might be explained by some systematic error in measuring the radiosensitization effect in this work. A $SER_{10,AE}$(35 keV, 9% IUdR) value larger than 1.01 was expected to be measured, e.g., approximately 1.18 or half of the enhancement for 18% IUdR. Results using Equation (4.17) give further reason to suspect a systematic error was made in measuring $SER_{10,RS}$(E, 9% IUdR), hence masking the Auger effect.

CHAPTER 5: CONCLUSIONS & RECOMMENDATIONS

5.1 Summary of Results

- Rat 9L Glioma Cell Survival: The survival curve for rat 9L glioma cells for the experimental condition (4 MV, 0% IUdR) resulted in a D_{10} value of 11.2 Gy, which compared well to previously reported data (Franko *et al.* 1992). This provided confidence in the measurements of dose and cell survival.
- LET Effect: The $SER_{10,LET}$ of monochromatic x-ray beams (25-35 keV) increased from 1.08 ± 0.03 at 35 keV to 1.37 ± 0.02 at 25 keV. This was due to decreasing x-ray energy, resulting in lower-energy secondary electrons whose LET increased, hence increasing $SER_{10,LET}$ (i.e., RBE). These results were consistent with the trend of previously reported RBEs.
- Radiosensitization Effect: The radiosensitivity of rat 9L glioma cells for 4 MV x-rays increased as %IUdR content in the DNA increased, being 1.28 ± 0.02 for 9% and 1.40 ± 0.02 for 18%. The effect, however, was less than that reported in CHO cells (Dugas *et al.* 2011), i.e., about one-third the increase in SER_{10} per %IUdR.
- Auger Effect (18% IUdR): At 35 keV, $SER_{10,AE}$ = 1.35 ± 0.05 was extracted; however, an alternative, more traditional analysis yielded 1.27 ± 0.06. Although lower than $SER_{10,AE}$ values extracted from Dugas *et al.* (2011) for CHO cells, it was equally significant since the radiosensitization effect was less in rat 9L glioma cells compared to CHO cells.

  Based on the number of photoelectric events per 2 Gy calculated by Karnas *et al.* (2001), the resulting $SER_{10,AE}$ value for 18% IUdR at 30 keV (1.06 ± 0.03) was consistent and at 25 keV (0.98 ± 0.03) was somewhat inconsistent with what might be expected. It was not clear why 25 keV results were not as close to agreeing. Systematic errors in 4 MV or

monochromatic x-ray dosimetry could not be the cause, as such errors divide out in Equation (4.8).

- Auger Effect (9%): At 35 keV the extracted effect ($SER_{10,AE}$ = 1.01 ± 0.04) was less than what was expected (1.18); however, an alternative, more traditional analysis yielded 1.25 ± 0.06. Of question was whether the value of $SER_{10,RS}$ (35 keV, 9% IUdR) = 1.28 ± 0.02 was too high, masking extraction of the Auger effect in the first method of analysis. No significant effect was expected or observed for 25 keV. In fact, the value of $SER_{10,RS}$ (25 keV, 9% IUdR) = 0.82 ± 0.02 also indicated possible systematic errors in $SER_{10,RS}$.
- Dosimetry: Although random errors were less significant, there is the potential for systematic errors in the dosimetry. At 4 MV, dose values determined using calculated dose according to a clinical paradigm overestimated measured film dose by approximately 6%; if film doses were utilized, $SER_{10,LET}$ values would have decreased, but had no effect on $SER_{10,RS}$ or $SER_{10,AE}$.

  For 25-35 keV, the dosimetry was based on film that was calibrated to ion chamber dosimetry based on TG-61, which was slightly outside its intended scope. Also, the ion chamber was not calibrated at energies sufficiently low as to bracket the energies used in this study. Therefore, chamber factors had to be extrapolated. When compared with fluence measurements (converted to dose using MCNP5 Monte Carlo calculations) the ion chamber dose overestimated fluence-based dose by 2-7% at 25 keV and underestimated fluence-based dose by 1-2.5% at 35 keV. Again, systematic dose errors only impact $SER_{10,LET}$, having no effect on $SER_{10,AE}$.
- Comparison with Corde's *et al.* (2004) Data: With respect to the ratio of SER_{10} values (D_{10}(E, 0% IUdR)/D_{10}(E, 18% IUdR)) at 35 keV and 30 keV, this work's value (1.28 ± 0.06)

was comparable to that of Corde *et al.* (2004) for SQ20B cells with ~10−20% IUdR irradiated at 33.5 keV and 32.8 keV (1.31). However, our survival curves for (35 keV, 0% IUdR), (30 keV, 0% IUdR), and (30 keV, 18% IUdR) all had shoulders as expected, whereas the corresponding curves of Corde's *et al.* did not. Based on this comparison and this work's accurate measurement of %IUdR in 9L cells, it is believed that this work's data is of higher quality. Also, it is believed that this work's method of combining multiple data sets for data analysis to be superior.

5.2 Conclusions

The hypothesis of this thesis was that the SER_{10} for 9% and 18% IUdR-laden rat 9L glioma cells irradiated by 25-35 keV photons will be greatest at 35 keV due to the Auger effect. Results of this research proved the hypothesis to be correct; in fact, 35 keV was the only energy to exhibit any significant Auger effect. The effect, however, was only evident for cells containing 18% IUdR and marginal for cells containing 9% IUdR. Based on these results, the energy dependence of photo-activated Auger electron therapy from 40-70 keV remains of possible clinical relevance and is worth further investigation.

5.3 Recommendations for Improved Technology & Methodology in Future Cell Survival Measurements

Future monochromatic x-ray measurements should be of higher quality on the new medical radiobiological beamline at CAMD, which will have several enhancements to the present study. A comparison of some of the properties of the new beamline expected to be operational in late 2013 is summarized in Table 5.1.

- Beam monitor: The x-ray beam intensity should be monitored using the current measured from a transmission ion chamber to provide monitor units in lieu of the electron storage ring

Table 5.1: CAMD radiobiological beamline improvements that will be operational in late 2013.

CAMD Beamline Improvements	Old Beam Properties	New Beam Properties	Impact of New Beam Properties
Higher Beam Energies	Up to 35 keV	Up to 75 keV	Investigate Auger effect at higher energies (35-75 keV)
Increased Monochromatic Photon Flux	D' << 0.1 Gy*min^{-1} at E > 35 keV	D' > 0.1 Gy*min^{-1} at E < 75 keV	Reduced radiation times at E > 35 keV
Increased Beam Width	3 cm	10 cm	More cell cultures irradiated at the same time; small animal irradiation studies possible
Beam Monitor	Ring current * duration of irradiation	Transmission ion chamber	Increase efficiency and accuracy of delivered dose

current as a function of irradiation time that was used in this study. It should be able to automatically integrate and record the ion chamber current (proportional to photon fluence and dose rate) readings so that the user no longer needs to manually record the ring current every five minutes and keep time of the irradiation. This is particularly important because previous data from Brown *et al.* (2012b) showed the ratio of dose rate to ring current varied for at least one hour after electron injection.

- 4 MV Irradiations: The objective is to make the 4 MV dose received by the cells less subjective to errors with respect to depth and to achieve agreement between calculated and film measured dose given to the cells. Irradiations at 4 MV should be done at a depth of at least 2 cm to provide sufficient build-up of secondary electrons and to maintain full scatter conditions. This can be accomplished by using a 30 x 30 cm^2 field, milling the shapes of four cell culture flasks into a 5 cm thick plastic water slab, and placing a 1 cm thick plastic water slab to cover the cell culture flasks. The air gap in the cell culture flask should also be eliminated by completely filling it with medium. To prevent medium spillage from the cell

culture flasks, the phantom can be positioned vertically such that the flasks are pointed upward and the gantry of the linac can be rotated 90° to maintain the same geometry as in this project.

- Monochromatic keV Photon Irradiations: Monochromatic irradiations should also be done at a deeper depth. The objective is to make the cell dose less sensitive to variations in dose in the first 1 cm depth as observed by Oves (2008). The shape of a cell culture tube flask could be milled into a PMMA block such that the flask could be inserted into the phantom and the distance from the surface of the phantom to the cells be approximately 1.2 cm. Also, it should be possible to use film as an *in vitro* dosimeter to periodically measure the dose rate throughout an electron injection cycle as well as at the beginning and/or at the end of a cell irradiation experiment. As a minimum, the dose to the cells should be measured with film at the beginning, middle, and end of each re-injection cycle to document no change.

5.4 Recommendations for Future Cell Survival Studies to Elucidate the Role of the Auger Effect in keV Irradiations

The present study was part of a larger study to understand the dependence of cell survival versus dose on the quality of the beam (i.e., energy of monochromatic x-rays). This requires additional data and radiobiological modeling.

- Cell Irradiations (40−70 keV): Cell irradiations should be done at energies higher than 35 keV (40−70 keV) to observe whether there is an optimal irradiation energy above the K-edge of iodine, as Corde *et al.* (2004) reported. An initial measurement of the cell survival curve at 35 keV should be made to demonstrate no changes following the technological upgrades in Section 5.3.

- Radiobiological modeling: Create a radiobiological model that includes the effects of (1) RBE of beam as a function of energy; (2) the number of photoelectric (i.e. Auger) events as a function of dose, %IUdR, and energy; and (3) radiosensitivity as a function of dose, %IUdR, and energy. Then, all sets from all experimental conditions (E, %IUdR) should be fit at once.
- % IUdR: 9L glioma cells should be allowed to uptake a concentration of IUdR that have additional values between 0% and 18% IUdR to evaluate the possibility of a threshold amount existing. It should also be investigated why there are such unusual results at 9% IUdR at 25 keV.

REFERENCES

Aird E G A, Burns J E, Day M J, Duane S, Jordan T J, Kacperek A, Klevenhagen S C, Harrison R M, Lillicrap S C, McKenzie A L, Pitchford W G, Shaw J E, and Smith C W 1996 Central axis depth dose data for use in radiotherapy: A survey of depth doses and related data measured in water or equivalent media *Brit. J. Radiol.* (suppl. 25) 86

Almond P R, Biggs P J, Coursey B M, Hanson W F, Saiful Hug M, Nath R, and Rogers D O W 1999 AAPM's TG-51 protocol for clinical reference dosimetry of high-energy photon and electron beams *Med. Phys.* **26** 1847-70

Annunziato A 2008 DNA packaging: Nucleosomes and Chromatin *Nature Education* **1** 1 http://www.nature.com/scitable/topicpage/dna-packaging-nucleosomes-and-chromatin-310

Bencokova Z, Laurianne P, Devic C, Joubert A, Gastaldo J, Massart C, Balosso J, and Foray N 2008 Molecular and cellular response of the most extensively used rodent glioma models to radiation and/or cisplatin *J. Neurooncol*. **86** 13-21

Berry S E, Garces C, Hwang H S, Kunugi K, Meyers M, Davis T W, Boothman D A, and Kinsella T J 1999 The mismatch repair protein, hMLH1, mediates 5-substituted halogenated thymidine analogue cytotoxicity, DNA incorporation, and radiosensitization in human colon cancer cells *Cancer Res.* **59** 1840-5

Bevington P R 1992 *Data Reduction and Error Analysis for the Physical Sciences* (New York, NY: McGraw-Hill)

Bistrovic M, Biscan M, and Viculin T 1986 RBE of 20 kV and 70 kV X-rays determined for survival of V79 cells *Radiother. Oncol.* **7** 175-80

Brown T A D, Hogstrom K R, Alvarez D, Matthews II K L, and Dugas J P 2012a Dose-response curve of EBT, EBT2, and EBT3 radiochromic films to synchrotron-produced monochromatic x-ray beams *Med. Phy.* **39** 7412-7

Brown T A D, Hogstrom K R, Alvarez D, Matthews II K L, and Ham K 2012b Verification of TG-61 dose for synchrotron-produced monochromatic x-ray beams using fluence-normalized MCNP5 calculations *Med. Phys*. **39** 7462-9

Buchegger F, Perillo-Adamer F, Dupertuis Y M, and Delaloye A B 2006 Auger radiation targeted into DNA: a therapy perspective *Eur. J. Nucl. Med. Mol. Imaging* **33** 1352-63

Chang C N, Doong S L and Cheng Y C 1992 Conversion of 5-iodo-2-pyrimidinone-2'-deoxyribose to 5-iodo-deoxyuridine by aldehyde oxidase *Biochem. Pharmacol.* **43** 2269-73

Coleman M T, Allred L E, Hart R W, and Yates A J 1980 Relationship between gangliosides and doubling times in cultured human brain and brain tumor cells *Cancer Lett.* **8** 255-62

Corde S, Biston M C, Elleaume H, Estève F, Charvet A M, Joubert A, Ducros V, Bohic S, Simionovici A, Brochard T, Nemoz C, Renier M, Troprès, I, Fiedler S, Bravin A, Thomlinson W, Le Bas J and Balosso J 2002 Lack of cell death enhancement after irradiation with monochromatic synchrotron x-rays at the K-shell edge of platinum incorporated in living SQ20B human cells as cis-diamminedichloroplatinum (II) *Radiat. Res.* **158** 763-70

Corde S, Joubert A, Adam J F, Charvet A M, Le Bas J F, Estève F, Elleaume H, and Balosso J 2004 Synchrotron radiation-based experimental determination of the optimal energy for cell radiotoxicity enhancement following photoelectric effect on stable iodinated compounds *Brit. J. Cancer* **91** 544-51

Deutsch M, Rewers A B, Redgate E S, Fisher E R, and Boggs S S 1990 Intra-cerebral ventricular infusion of 5-iodo-2-deoxyuridine (IUdR) as a radiosensitizer in the treatment of a rat glioma *Int. J. Radiat. Oncol. Biol. Phys.* **19** 85-7

Djordjevic B and Szybalski W 1960 Genetics of human cells III. Incorporation of 5-bromo- and 5-iododeoxyuridine into the deoxyribonucleic acid of human cells and its effect on radiation sensitivity *J. Exp. Med.* **112** 509-53

Dugas J P, Oves S D, Sajo E, Matthews K L, Ham K, and Hogstrom K R 2008 Monochromatic beam characterization for Auger electron dosimetry and radiotherapy *Eur. J. Radiol.* (suppl 68) 137-41

Dugas J P, Varnes M E, Sajo E, Welch C E, Ham K, and Hogstrom K R 2011 Dependence of Cell Survival on IUdR Concentration in 35-keV Photon-activated Auger Electron Radiotherapy *Int. J. Radiat. Oncol. Biol. Phys*. **79** 255-61

Epstein A H, Cook J A, Goffman T, and Glatstein E 1992 Tumour radiosensitization with the halogenated pyrimidines 5'-bromo- and 5'-iododeoxyuridine *Br. J. Radiol.* (Suppl 24) 209-14

Erikson R L and Szybalski W 1963 Molecular radiobiology of human cell lines V. Comparative radiosensitizing properties of 5-halodeoxycytidines and 5-halodeoxyuridines *Radiat. Res.* **20** 252-62

Evans S M, Joiner B, Jenkins W T, Laughlin K M, Lord E M, and Koch C J 1995 Identification of hypoxia in cells and tissue of epigastric 9L rat glioma using EF5 [2-(2-nitro-1H-imidazol-1-yl)-N-(2,2,3,3,3-pentafluoropropyl)acetamide. *Br. J. Cancer* **72** 875-82

Fairchild R G, and Bond V P 1984 Photon activation therapy *Strahlentherapie* **160** 758-63

Fairchild R G, Brill A B, and Ettinger K V 1982 Radiation Enhancement with Iodinated Deoxyuridine. *Invest. Radiol.* **17** 407-16

Fairchild R G, Laster B H, Commerford S L, Furcinitti P S, Sylvester B, Gabel D, Popenoe E, and Foster S 1985 Photon-activated therapy with ^{127}I-deoxyuridine: Measurement of dose enhancement in cultured mammalian cells. In: *Proceedings of a Workshop on Photon Activation Therapy*. Report No. BNL 51997 (Upton, NY: Brookhaven National Laboratory)

Ferri N, Cazzaniga S, Mazzarella L, Curigliano G, Lucchini G, Zerla D, Gandolfi R, Facchetti G, Pellizzoni M, and Rimoldi I 2013 Cytotoxic effect of (1-methyl-1H-imidazol-2-yl) methanamine and its derivatives in Pt(II) complexes on human carcinoma cell lines: A comparative study with cisplatin *Bioorg. Med. Chem.* **21** 2379-86

Franko A J, Koch C J, and Boisvert D P J 1992 Distribution of misonidazole adducts in 9L gliosarcoma tumors and spheroids: Implications for oxygen distribution *Cancer Res*. **52** 3831-7

Gibco® Life Technologies *Technical Resources—Media Formulations for 21700 Ham's F-12, powder* http://www.invitrogen.com/site/us/en/home/support/Product-Technical Resources /media_formulation.66.html

Guizzetti M, Kavanagh T J, and Costa L G 2011 Measurements of astrocyte proliferation, In *In Vitro Neurotoxicology: Methods and Protocols* **758** 349-59 (Totowa, NJ: Springer Science)

Hall E J and Giaccia A J 2006 *Radiobiology for the Radiologist* 6th edn (Philadelphia, PA: Lippincott)

Harrington K J, Syrigos K N, Uster P S, Zetter A, Lewanski C R, Gullick W J, Vile R G, and Stewart J S W 2004 Targeted radiosensitization by pegylated liposome-encapsulated 3', 5'-O-dipalmitoyl 5-iodo-2'-deoxyuridine in a head and neck cancer xenograft model *Brit. J. Cancer* **91** 366-73

Heilmann J, Taucher-Scholz G, and Kraft G 1995 Induction of DNA double-strand breaks in CHO-K1 cells by carbon ions *Int. J. Radiat. Biol.* **68** 153-62

Hong W K, Bast Jr. R C, Hait W N, Kufe D W, Pollock R E, Weichselbaum R R, Holland J F, and Frei III E 2009 *Holland-Frei Cancer Medicine* 8th edn (Shelton, CT: PMPH-USA)

Hoshi M, Antoku S, Nakamura N, Russell W J, Miller R C, Sawada S, Mizuno M, and Nishio S 1988 Soft X-ray dosimetry and RBE for survival of Chinese hamster V7 cells *Int. J. Radiat. Biol*. **54** 577-91

Hubbell J H and Seltzer S M 2004 Tables of x-ray mass attenuation coefficients and mass energy-absorption coefficients 1 keV to 20 MeV for elements Z = 1 to 92 and 48 additional substances of dosimetric interest *National Institute of Standards and Technology* (Gaithersburg, MD) http://www.nist.gov/pml/data/xraycoef/index.cfm

Humm J L and Charlton D E 1989 A new calculational method to assess the therapeutic potential of Auger electron emission *Int. J. Radiat. Oncol. Biol. Phys.* **17** 351-60

Iliakis G and Kurtzman S 1989 Keynote address: Application of non-hypoxic cell sensitizers in radiobiology and radiotherapy: Rationale and future prospects *Int. J. Radiat. Oncol. Biol. Phys*. **16** 1235-41

Jensen A D, Münter M W, and Debus J 2011 Review of clinical experience with ion beam radiotherapy *Brit. J. Radiol.* **84** S35-S47

Karnas S J, Moiseenko V V, Yu E, Truong P, and Battista J J 2001 Monte Carlo simulations and measurement of DNA damage from x-ray-triggered Auger cascades in iododeoxyuridine (IUdR) *Radiat. Environ. Biophys.* **40** 199-206.

Karnas S J, Yu E, McGarry R C, and Battista J J 1999 Optimal photon energies for IUdR k-edge radiosensitization with filtered x-ray and radioisotope sources *Phys. Med. Biol.* **44** 2537-49

Kassis A I 2004 The Amazing world of Auger electrons *Int. J. Radiat. Biol.* **80** 789-803

Kassis A I, and Adelstein S J 2005 Radiobiologic Principles in Radionuclide Therapy *J. Nucl. Med.* (suppl 46) 4-12

Kaye G W C, and Laby T H 1995 *Table of Physical & Chemical Constants* 16th edn http://www.kayelaby.npl.co.uk/atomic_and_nuclear_physics/4_2/4_2_1.html

Keall P J, Kini V R, Vedam S S and Mohan R 2001 Motion adaptive x-ray therapy: a feasibility study *Phys. Med. Biol.* **46** 1-10

Keall P J, Kini V R, Vedam S S and Mohan R 2002 Potential radiotherapy improvements with respiratory gating *Australas Phys Eng Sci Med* **25** 1-6

Kereiakes J G, Rao D V, Sastry K S R, and Howell R W 1993 Auger Electron Dosimetry: Report of Task Group No. 6 AAPM Nuclear Medicine Committee *Med. Phys.* **19** 1359-83

Khan F M 2010 *The Physics of Radiation Therapy* 4th edn (Philadelphia, PA: Lippincott)

Kinsella T J, Kunugi K A, Vielhuber K A, McCulloch W, Liu S H, and Cheng Y C 1994 An *in vivo* comparison of oral 5-iodo-2'-deoxyuridine and 5-iodo-2-pyrimidinone-2'-deoxyribose toxicity, pharmacokinetics, and DNA incorporation in athymic mouse tissues and human colon cancer xenograft, HCT-116 *Cancer Res.* **54** 2695-2700

Kinsella T J 1996 An approach to the radiosensitization of human tumors *Can. J. Sci. Am.* **2** 184-93

Kinsella T J, Kunugi K A, Vielhuber K A, Potter D M, Fitzsimmons M E, and Collins J M 1998 Priclinical evaluation of 5-iodo-2-pyrimidinone-2'-deoxyribose as a prodrug for 5-iodo-2'-

deoxyuridine-mediated radiosensitization in mouse and human tissues *Clin. Cancer Res.* **4** 99-109

Kinsella T J, Vielhuber K A, Kunugi K A, Schupp J, Davis T W, and Sands H 2000a Preclinical toxicity and efficacy study of a 14-day schedule of oral 5-iodo-2-pyrimidinone-2'-deoxyribose as a prodrug for 5-iodo-2'-deoxyuridine radiosensitization in U251 human glioblastoma xenografts *Clin. Cancer Res.* **6** 1468-75

Kinsella T J, Schupp J E, Davis T W, Berry S E, Hwang H S, Warren K, Balis F, Barnett J, and Sands H 2000b Preclinical study of the systemic toxicity and pharmacokinetics of 5-iodo-2-deoxypyrimidinone-2'-deoxyribose as a radiosensitizing prodrug in two, non-rodent animal species: Implications for phase I study design *Clin. Cancer Res.* **6** 3670-9

Kinsella T J, Kinsella M T, Seo Y, and Berk G 2007 5-iodo-2-pyrimidinone-2'-deoxyribose-mediated cytotoxicity and radiosensitization in U87 human glioblastoma xenografts *Int. J. Radiat. Oncol. Biol. Phys*. **69** 1254-61

Kinsella T J 2008 Update on radiosensitization by halogenated thymidine analogs-molecular mechanisms of drug processing and cell death signaling: Implications for future clinical trials *Cancer Biol. Ther.* **7** 1567-9

Kinsella T J, Kinsella M T, Hong S, Johnson J P, Burback B, and Tosca P J 2008 Toxicity and pharmacokinetic study of orally administered 5-iodo-2-pyrimidinone-2'-deoxyribose (IPdR) x 28 days in Fischer-344 rats: Impact on the initial clinical phase I trial design of IPdR-mediated radiosensitization *Cancer Chemother. Pharmacol.* **61** 323-34

Kummar S, Anderson L, Hill K, Majerova E, Allen D, Homeffer Y, Ivy S P, Rubinstein L, Harris P, Doroshow J H, and Collins J M 2013 First-in-human phase 0 trial of oral 5-iodo-2-pyrimidinone-2'-deoxyribose in patients with advanced malignancies *Clin. Cancer Res.* **19** 1852-7

Kutcher G J, Coia L, Gillin M, Hanson W F, Leibel S, Morton R J, Palta J R, Purdy J A, Reinstein L E, Svensson G K, Weller M, and Wingfield L 1994 Comprehensive QA for radiation oncology: Report of AAPM Radiation Therapy Committee Task Group 40 *Med. Phys*. **21** 581-618

Laster B H, Thomlison W C, and Fairchild R G 1993 Photon activation of iododeoxyuridine: biological efficacy of Auger electrons *Radiat. Res.* **133** 219-24

Lawrence T S, Davis M A, Maybaum J, Stetson P L, and Ensminger W D 1990 The dependence of halogenated pyrimidine incorporation and radiosensitization on the duration of drug exposure *Int. J. Radiat. Oncol. Biol. Phys.* **18** 1393-8

Leith J T, Schilling W A and Wheeler K T 1975 Cellular radiosensitivity of a rat brain tumor *Cancer* **35** 1545-50

Lilley, J S 2001 *Nuclear Physics: Principles and Applications* 1st edn (Hoboken, NJ: Wiley)

Lodish H, Baltimore D, Berk A, Zipursky S L, Matsudaira P, and Darnell J 1995 *Molecular Cell Biology* 3rd edn (New York, NY: W H Freeman)

Ma C M, Coffey C W, DeWerd L A, Liu C, Nath R, Seltzer S M, and Seuntjens J P 2001 AAPM protocol for 40-300 kV x-ray beam dosimetry in radiotherapy and radiobiology *Med. Phys.* **28** 868-93

Marquardt, D W 1963 An algorithm for least squares estimation of parameters *J. Soc. Ind. Appl. Math.* **11** 431-41

McGinn C J and Kinsella T J 1993 The clinical rationale for S-phase radiosensitization in human tumors *Curr. Prob. Cancer* **17** 277-321

Miller R W, DeGraff W, Kinsella T J, and Mitchell J B 1987 Evaluation of incorporated iododeoxyuridine cellular radiosensitization by photon activation therapy *Int. J. Radiat. Oncol. Biol. Phys.* **13** 1193-7

Nath R, Bongiorni P, and Rockwell S 1987 Enhancement of IUdR radiosensitization by low energy photons *Int. J. Radiat. Oncol. Biol. Phys*. **13** 1071-9

NCRP (National Council on Radiation Protection and Measurements) 2005 Structural Shielding Design and Evaluation for Megavoltage X- and Gamma-Ray Radiotherapy Facilities *Report 151* (Bethesda, MD: NCRP)

Niroomand-Rad A, Blackwell C R, Coursey B M, Galvin J M, McLaughlin W L, Meigooni A S, Nath R, Rodger J E, and Soares C G 1998 Radiochromic film dosimetry: Recommendations of AAPM Radiation Therapy Committee Task Group 55 *Med. Phys.* **25** 2093-115

Oves, S D 2008 Dosimetry Intercomparison using a 35-keV x-ray synchrotron beam MS thesis Louisiana State University http://etd.lsu.edu/docs/available/etd-01182008-133454/

Oves S D, Hogstrom K R, Ham K, Sajo E, and Dugas J P 2008 Dosimetry intercomparison using a 35-keV x-ray synchrotron beam *Eur. J. Radiol.* (suppl 68) 121-5

Prusoff W H, Chen W S, and Fischer P H 1979 Antiviral iodinated pyrimidines deoxyribonnucleosides: 5-iodo-2'-deoxyuridine; 5-iodo-2'-deoxycytidine; 5-ido-5'-amino-2', 5' deoxyuridine *Pharmacol. Therapeut.* **7** 1-34

Reed E 1992 Cisplatin *Cancer Chemother. Biol. Response Modif.* **13** 83-90

Rosseau J, Boudou C, Barth R F, Balosso J, Estève F, and Elleaume H 2007 Enhanced survival and cure of F98 glioma-bearing rats following intracerebral delivery of carboplatin in combination with photon irradiation *Clin. Cancer Res.* **3** 5195-201

Rousseau J, Adam J F, Deman P, Wu T D, Guerquin-Kern J L, Gouget B, Barth R F, Estève F, and Elleaume H 2009 Intracerebral delivery of 5-iodo-2'-deoxyuridine in combination with synchrotron stereotactic radiation for the therapy of the F98 glioma *J. Synchrotron Radiat.* **16** 573-81

Saif M W, Berk G, Cheng Y C, and Kinsella T J 2007 IPdR: A novel oral radiosensitizer *Expert Opin. Investig. Drugs* **16** 1415-24

Schulz C, Mehta M P, Badie B, McGinn C J, Robins H I, Hayes L, Chappell R, Volkman J, Binger K, Arzoomanian R, Simon K, Alberti D, Feierabend C, Tutsch K D, Kunugi K A, Wilding G, and Kinsella T J 2004 Continuous 28-day iododeoxyuridine infusion and hyperfractionated accelerated radiotherapy for malignant glioma: a phase I clinical study *Int. J. Radiat. Oncol. Biol. Phys.* **59** 1107-15

Seo Y, Yan T, Schupp J E, Colussi V, Taylor K L, and Kinsella T J 2004 Differential radiosensitization in DNA mismatch repair-proficient and –deficient human colon cancer xenografts with 5-iodo-2-pyrimidinone-2'-deoxyribose *Clin. Cancer Res.* **10** 7520-8

Seo Y, Yan T, Schupp J E, Radivoyevitch T, and Kinsella T J 2005 Schedule-dependent drug effects of oral 5-iodo-pyrimidinone-2'-deoxyribose as an *in vivo* radiosensitizer in U251 human glioblastoma xenografts *Clin. Cancer Res.* **11** 7499-7507

Shinohara K, Nakano H, and Ohara H 1996 Detection of Auger enhancement induced in HeLa cells labeled with iododeoxyuridine and irradiated with 150 kV x-rays *Acta Oncol.* **35** 869-75

Spadinger I and Palcic B 1992 The relative biological effectiveness of Co-60 γ-rays, 55 kVp X-rays, 250 kVp X-rays, and 11 MeV electrons at low doses *Int. J. Radiat. Biol.* **61** 345-53

Verellen D, De Ridder M, Linthout N, Tournel K, Soete G and Storme G 2007 Innovations in image-guided radiotherapy *Nat Rev Cancer* **7** 949-960

Wang Y and Iliakis G 1992 Effects of 5'-iododeoxyuridine on the repair of radiation induced potentially lethal damage interphase chromatin breaks and DNA double strand breaks in Chinese hamster ovary cells **23** *Int. J. Radiat. Oncol. Biol. Phys*. 353-60

Weizsaecker M, Deen D F, Rosenblum M L, Hoshino T, Gutin P H, and Barker M 1981 The 9L Rat Brain Tumor: Description and Application of an Animal Model *J. Neurol.* **224** 183-92

Zelefsky M J, Fuks Z, Happersett L, Lee H J, Ling C C, Burman C M, Hunt M, Wolfe T, Venkatraman E S, Jackson A, Skwarchuk M, and Leibel S A 2000 Clinical experience with intensity modulated radiation therapy (IMRT) in prostate cancer *Radiother. Oncol.* **55** 241-9

APPENDIX A: CALCULATIONS

A.1 Calculation of Photoelectric Interactions per 2 Gy Dose

A.1.1 Calculation for the Number of Auger Events per 2 Gy Dose to Water for Iodine Atoms

Step 1: Calculating photoelectric cross section, σ, for iodine at 33.2 keV:

$\sigma = \left(\frac{\mu}{\rho}\right) * \frac{M_I}{N_A}$,

$\left(\frac{\mu}{\rho}\right)$ = mass attenuation coefficient = 35 cm^2/g, assuming all photoelectric absorption at 33.2 keV for iodine (Hubbell & Seltzer 2004).

M_I = molar mass of iodine = 126.9 g/mol.

N_A = Avogadro's number = 6.023 x 10^{23} iodine atoms/mole.

σ = 7.3742 x 10^{-21} cm^2/atom = 7374 barns/atom[†].

Step 2: Calculating photon fluence per Gy dose in water:

Fluence, $\varphi = \frac{\text{Number of particles}}{\text{area}}$.

Energy fluence, $\Psi = \varphi * E$, where E = energy per photon = 33.2 keV.

$D_w = \Psi * \left(\frac{\mu_{en}}{\rho}\right) = \varphi * E * \left(\frac{\mu_{en}}{\rho}\right)$,

D_w is dose to water.

$\left(\frac{\mu_{en}}{\rho}\right)$ = mass energy absorption coefficient for medium, i.e. water = 0.128 cm^2/g for 33.2 keV for iodine; interpolated using data available from Hubbell & Seltzer (2004).

$$\frac{\varphi}{D_w} = \frac{1}{E * \left(\frac{\mu_{en}}{\rho}\right)} = \frac{1}{\left(33.2 * 10^3 \ {}^{eV}/_{\gamma}\right) * \left(0.128 \ {}^{cm^2}/_{g}\right) * \left(\frac{1.602 * 10^{-19} J}{eV}\right) * \left(\frac{1000 \ g}{1 \ kg}\right)}$$

[†] Agrees well with Humm & Charlton (1989).

$= 1.469 \text{ x } 10^{12} \frac{\gamma}{\text{cm}^2 * \text{Gy}}$ ‡.

Step 3: Calculating number of photoelectric interactions per atom per Gy:

$\frac{\varphi}{D_w} * \sigma = 1.469 \text{ x } 10^{12} \frac{\gamma}{\text{cm}^2 * \text{Gy}} * 7.374 \text{ x } 10^{-21} \frac{\text{cm}^2}{\text{atom}} = 1.0833 \text{ x } 10^{-8} \frac{\text{interactions}}{\text{atom} * \text{Gy}}$.

Step 4: Calculating number of photoelectric interactions in iodine per cell per 2 Gy (with 20% IUdR):

There are $6 \text{ x } 10^9$ base pairs (bps) of DNA per cell (Annunziato 2008).

$$\left(\frac{6 * 10^9 \text{ bps}}{\text{cell}}\right) * \left(\frac{1 \text{ thymidine}}{2 \text{ bps}}\right) * \left(\frac{20 \text{ iodine atoms}}{100 \text{ thymidine}}\right) = 6 * 10^8 \frac{\text{I atoms}}{\text{cell}}.$$

$$\left(6 * 10^8 \frac{\text{I atoms}}{cell}\right) * \frac{\varphi}{\text{D}_\text{w}} * \sigma = \left(6 * 10^8 \frac{\text{I atoms}}{cell}\right) * 1.469 \text{ x } 10^{12} \frac{\gamma}{\text{cm}^2 * \text{Gy}} * 7.374 \text{ x } 10^{-21} \frac{\text{cm}^2}{\text{atom}}$$

$= 6.5 \frac{\text{interactions}}{\text{cell} * \text{Gy}}$ § = $\mathbf{13.0} \frac{\textbf{interactions}}{\textbf{cell}}$ for 2 Gy.

A.1.2 Number of Auger Events per 2 Gy Dose to Water for Platinum

This calculation follows the same steps 1−4 as in Section A.1.1:

Step 1: Calculating photoelectric cross section for platinum at 78.4 keV:

$\sigma = \left(\frac{\mu}{\rho}\right) * \frac{M_{Pt}}{N_A}$,

$\left(\frac{\mu}{\rho}\right)$ = mass attenuation coefficient = 8.981 cm^2/g, assuming all photoelectric absorption at 78.4 keV for platinum (Hubbell & Seltzer 2004).

M_{Pt} = molar mass of platinum = 195.084 g/mol.

N_A = Avogadro's number = $6.023 \text{ x } 10^{23}$ platinum atoms/mole.

‡ Agrees well with Humm & Charlton (1989).
§ Agrees well with Humm & Charlton (1989).

$\sigma = 2.9089 \times 10^{-21}$ cm^2/atom = 2909 barns/atom.

Step 2: Calculating photon fluence per Gy dose in water:

Fluence, $\varphi = \frac{\text{Number of particles}}{\text{area}}$.

Energy fluence, $\Psi = \varphi * E$, where E = energy per photon = 78.4 keV.

$D_w = \Psi * \left(\frac{\mu_{en}}{\rho}\right) = \varphi * E * \left(\frac{\mu_{en}}{\rho}\right)$,

D_w is dose to water.

$\left(\frac{\mu_{en}}{\rho}\right)$ = mass energy absorption coefficient for medium, i.e. water = 0.02644 cm^2/g for 78.4 keV for platinum. Interpolated using data available from Hubbell & Seltzer (2004).

$$\frac{\varphi}{D_w} = \frac{1}{E * \left(\frac{\mu_{en}}{\rho}\right)} = \frac{1}{(78.4 * 10^3\ {}^{eV}/_{\gamma}) * \left(0.02644\ {}^{cm^2}/_{g}\right) * \left(\frac{1.602 * 10^{-19} J}{eV}\right) * \left(\frac{1000\ g}{1\ kg}\right)}$$

$= 3.011 \times 10^{12} \frac{\gamma}{\text{cm}^2 * \text{Gy}}$.

Step 3: Calculating number of photoelectric interactions per atom per Gy:

$\frac{\varphi}{D_w} * \sigma = 8.7587 \times 10^{-9} \frac{\text{interactions}}{\text{atom} * \text{Gy}}$.

Step 4: Calculating number of photoelectric interactions in platinum per cell per 2 Gy:

According to Corde *et al*. (2002) they achieved a platinum content of 4.5 x 10^6 atoms/cell for cells exposed to 1 μM CDDP for 12 h (17% cell survival), so:

$$\left(4.5 * 10^6 \frac{\text{Pt atoms}}{cell}\right) * \frac{\varphi}{\text{D}_\text{w}} * \sigma = \left(4.5 * 10^6 \frac{\text{Pt atoms}}{cell}\right) * 8.7587 \times 10^{-9} \frac{\text{interactions}}{\text{atom} * \text{Gy}}$$

$= 0.04 \frac{\text{interactions}}{\text{cell} * \text{Gy}} = \mathbf{0.08} \frac{\textbf{interactions}}{\textbf{cell}}$ per 2 Gy.

A.2 Steps to Calculate the Dose Rate from Calibration Geometry to Cell Irradiation Geometry for 4 MV X-Rays

(1) Professional medical physicists at MBPCC have calibrated the Clinac 21EX to deliver a dose rate at calibration point (FS = 10 x 10 cm^2 (isocenter), SSD = 90 cm, d_o = 10 cm, SPD_o = SSD + d_o = 100 cm) of 0.758 cGy*MU^{-1} to water at isocenter for 4 MV beam ($D'_o = D'^{iso}_w(10, 10)$ = 0.758 cGy*MU^{-1}). This dose rate can be used to calculate the dose rate for the cell irradiation geometry illustrated in Figure 3.1 (FS = 44.96 x 44.96 cm^2, SPD = 149.88 cm, d = 0.62 cm). Figure A.1 demonstrates step by step the geometry of the calculations required.

Step #	Media	FS (cm^2) (at SSD)	FS (cm^2) (at SPD)	SSD (cm)	SPD (cm)	depth (cm)
(1)	H_2O	-	10 x 10	90	100	10
(2)	H_2O	-	30 x 30	90	100	10
(3)	H_2O	-	30 x 30	98.8	100	1.2
(4)	Air	29.64 x 29.64	-	98.8	100	-
(5)	Air	-	44.96 x 44.96	-	149.88	-
(6)	H_2O	-	44.96 x 44.96	-	149.88	1.2
(7)	H_2O	-	44.96 x 44.96	-	149.88	0.62

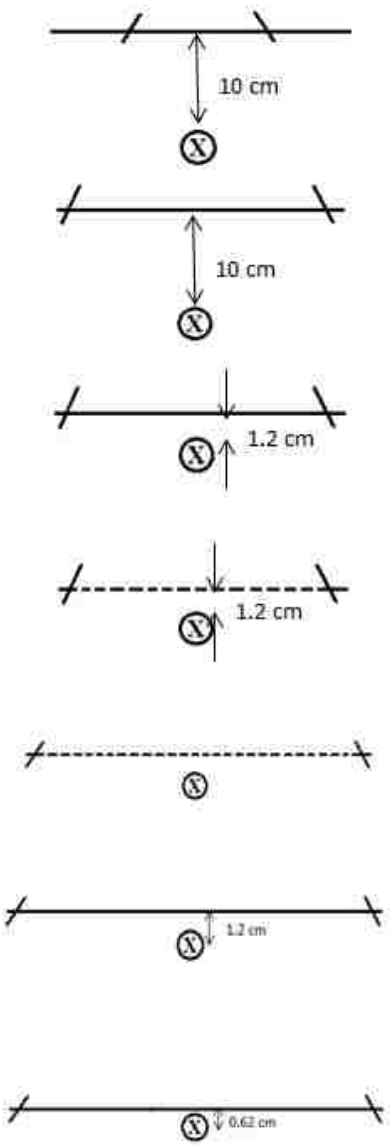

Figure A.1: Diagram demonstrating steps to calculate the dose rate from calibration geometry to cell irradiation geometry for 4 MV x-rays.

(2) Using Table 3.1(b) (Section 3.2.1.1), the in-air output factors at depth = 10 cm due to both collimator and phantom scatter (S_c*S_p) can be looked up for a FS = 30 x 30 cm^2 (let r_c = 30 cm) at calibration point (field size at isocenter, i.e., SPD_o = 100 cm, for cell geometry is FS = 30 x 30 cm^2):

$$S_c * S_p(30) = 1.195. \tag{A.1}$$

To calculate the dose rate to water using FS = 30 x 30 cm^2 (isocenter) at calibration point (d = 10 cm), $D'^{iso}_w(30, 10)$, S_c*S_p for the different field size must be considered and be multiplied to $D'^{iso}_w(10, 10)$:

$$\begin{aligned} D'^{iso}_w(30,10) &= D'^{iso}_w(10,10) * S_c * S_p(30) \\ &= 0.758\ \text{cGy} * \text{MU}^{-1} * 1.195 = 0.9058\ \text{cGy} * \text{MU}^{-1}. \end{aligned} \tag{A.2}$$

(3) Now the depth in phantom is changed to a reference depth of d_m = 1.2 cm (the depth of maximum dose), while maintaining the same source to point distance of 100 cm, so SSD = 100 cm - 1.2 cm = 98.8 cm. The dose rate to water at a depth of 1.2 cm can be calculated using Equation (A.2), the tissue phantom ratio (TPR) for FS = 30 x 30 cm^2 (isocenter) and d_m = 1.2 cm, which can be interpolated using data from Table 3.1(a):

$$\text{TPR}(30, 1.2) = 1.248, \tag{A.3}$$

$$\begin{aligned} D'^{iso}_w(30, 1.2) &= D'^{iso}_w(30, 10) * \text{TPR}(30, 1.2) \\ &= 0.9058\ \text{cGy} * \text{MU}^{-1} * 1.248 = 1.1305\ \text{cGy} * \text{MU}^{-1}. \end{aligned} \tag{A.4}$$

(4) To convert $D'^{iso}_w(30, 1.2) \rightarrow D'^{iso}_a(30, 1.2)$ (dose rate in water to dose rate in air), the total scatter caused by the phantom must be removed from the value. This is accomplished by dividing out the peak scatter factor, PSF, from $D'^{iso}_w(30, 1.2)$. Since FS = 30 x 30 cm^2 at isocenter (100 cm), and d_m = 1.2 cm, the top of the phantom is located at SSD = 98.8 cm. The field size at SSD = 98.8 cm is FS = 29.6 x 29.6 cm^2 (let r_{dm} = 29.6 cm). The true PSF is not known, but the normalized PSF was measured by Aird *et al.* (1996) and for a certain energy it varies by field size. The NPSF can be interpolated using a table found in Aird *et al.* (1996):

$$\text{NPSF}(29.6) = 1.0327. \tag{A.5}$$

The NPSF for a different field size will be required in step 7 and the ratio of the two NPSF will cancel the normalization constant, leaving the ratio of the true PSFs:

$$\frac{\text{NPSF}(\text{FS}_1)}{\text{NPSF}(\text{FS}_2)} = \frac{\text{PSF}(\text{FS}_1)}{\text{PSF}(\text{FS}_2)}. \tag{A.6}$$

For the moment, however, the NPSF will be used instead of PSF to calculate $D'^{iso}_a(30, 1.2)$:

$$D'^{iso}_a(30, 1.2) = \frac{D'^{iso}_w(30, 1.2)}{NPSF(29.6)} = \frac{1.1305\ cGy * MU^{-1}}{1.0327} = 1.0947\ cGy * MU^{-1}. \quad (A.7)$$

(5) Because the cell irradiation geometry has a SPD = 149.88 cm (150 cm from source to Solid Water® phantom surface where the cell flasks rest minus 0.12 cm thickness of the bottom of the cell flask) and FS = 45 cm at 150 cm, the field size at SPD = 149.88 cm is FS = 44.96 x 44.96 cm^2 (let r = 44.96 cm). To calculate the dose rate to air for FS = 44.96 x 44.96 cm^2, the inverse square law must be taken into account for intensity lost at a larger SPD compared to intensity that occurs at isocenter (SPD_o = 100 cm). The inverse square factor, ISF, is:

$$ISF = \left(\frac{SPD_o}{SPD}\right)^2 = \left(\frac{100\ cm}{149.88\ cm}\right)^2 = 0.4452. \quad (A.8)$$

Therefore,

$$D'_a(44.96, 1.2) = D'^{iso}_a(30, 1.2) * ISF = 1.0947\ cGy * MU^{-1} * 0.4452 = 0.4874\ cGy * MU^{-1}. \quad (A.9)$$

(6) To convert the dose rate to air in Equation (A.9) to dose rate to water, the PSF needs to be factored back in, but for the larger field size (FS = 44.96 x 44.96 cm^2). Extrapolating using the data found in Aird *et al.* (1996):

$$NPSF(44.96) = 1.043, \quad (A.10)$$

$$D'_w(44.96, 1.2) = D'_a(44.96, 1.2) * NPSF(44.96) = 0.4874\ cGy * MU^{-1} * 1.043 = 0.5084\ cGy * MU^{-1}. \quad (A.11)$$

(7) Next, the depth of measurement for cell irradiations must be considered. The depth of the medium is 0.5 cm. The thickness of the top of the cell flask is 0.12 cm. Consider that as the top of cell flask extends outward and approaches infinity, where there would be electron and photon side scatter equilibrium, the total depth of measurement is approximated to be (0.5 + 0.12) cm = 0.62 cm (let d = 0.62 cm), assuming the small air gap (≈ 0.5 cm) in between the top of the flask and the surface of the medium is ignored. The approximation still holds true if the width of the flask is much larger than the air gap in the flask (w>>ag). Because w = 5 cm >> ag = 1.75 cm, the approximation is valid (see Figure A.2)).

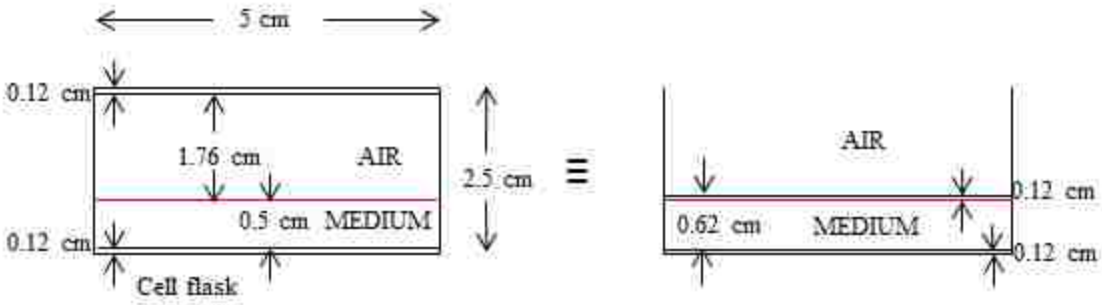

Figure A.2: Cell flask dimension approximation. When w >> ag ɜ w → ∞, the small air gap between the top of the cell flask and the surface of the medium can be ignored so that the total depth the 4 MV x-ray beam penetrates is 0.62 cm. This approximation still holds true in the present case because the width of the flask (5 cm) is much larger than the air gap (1.76 cm).

With this in mind, the dose rate to water for a field size FS = 44.96 x 44.96 cm^2 and d = 0.62 cm can be calculated using Equation (A.11) and TPR values from Table 3.1 (a). To know the fraction of the beam that contributes to dose at d = 0.62 cm, the TPRs for the desired depth, d, and d_m are used:

$$\frac{\mathrm{TPR}(44.96, 0.62)}{\mathrm{TPR}(44.96, 1.2)} = \frac{1.1523}{1.205} = 0.9563. \tag{A.12}$$

Therefore,

$$\mathrm{D'_w}(44.96, 0.62) = \mathrm{D'_w}(44.96, 1.2) * \frac{\mathrm{TPR}(44.96, 0.62)}{\mathrm{TPR}(44.96, 1.2)} = 0.5084\ \mathrm{cGy} * \mathrm{MU^{-1}} * 0.9563 = \mathbf{0.486\ cGy * MU^{-1}}. \tag{A.13}$$

Finally, by combining steps 1-7 into a single equation, the dose rate value calculated in Equation (A.13) could be calculated using:

$$\mathrm{D'} = \mathrm{D'_o} * \mathrm{S_c}(\mathrm{r_c}) * \mathrm{S_p}(\mathrm{r_c}) * \mathrm{TPR}(\mathrm{r_c}, \mathrm{d_m}) * \frac{\mathrm{NPSF(r)}}{\mathrm{NPSF}(\mathrm{r_{dm}})} * \mathrm{ISF} * \frac{\mathrm{TPR(r,\ d)}}{\mathrm{TPR}(\mathrm{r}, \mathrm{d_m})}. \tag{A.14}$$

Applying Equation (A.6):

$$\mathrm{D'} = \mathrm{D'_o} * \mathrm{S_c}(\mathrm{r_c}) * \mathrm{S_p}(\mathrm{r_c}) * \mathrm{TPR}(\mathrm{r_c}, \mathrm{d_m}) * \frac{\mathrm{PSF(r)}}{\mathrm{PSF}(\mathrm{r_{dm}})} * \mathrm{ISF} * \frac{\mathrm{TPR(r,\ d)}}{\mathrm{TPR}(\mathrm{r}, \mathrm{d_m})}. \tag{A.15}$$

APPENDIX B: DNA ISOLATION PROTOCOL

Details for DNA isolation using Promega Wizard kit Cat # A1120.

Day 1 – Process I

1. Pour a small amount of all reagents to be used into clean tubes to prevent contamination of reagents.

2. Remove the medium from T25 flasks by decanting and using pipetor to get the last drops, three flasks at a time. Can use the same tip; keep caps on the flasks as much as possible, at all times.

3. Pour PBS (1x strength) into a clean glass beaker and pour into flasks, three at a time (about 5 mL). Turn flasks growth-side-up to avoid directly pouring on cells. Wash 2x with PBS. Pipet out last drops out each flask each time, especially before adding lysis solution.

4. Add 600 μL of Nuclei Lysis Solution, three flasks at time and swirl it around gently. Place flasks flat as for growth for 5-10 minutes, then lie on its side on tilted angle for a few minutes so that the lysis solution pools at a corner of the flask. Remove solution using pipetor and transfer to microfuge tube (1.5-2 mL capacity; preferably clear-colored tubes). Pipet solution up and down before transferring to avoid mucus-like strings.

5. Add 5 μL of RNAse Solution to the nuclear lysates and mix the samples by inverting the tube 2-5 times.

6. Incubate for 15-30 minutes in water bath at 37^{o}C (optimally, 20 minutes).

7. Remove samples from water bath and allow cooling to room temperature for 5-10 minutes before proceeding to step 8. Prepare ice water bath.

8. To the room temp samples add 200 μL Protein Precipitation Solution. Vortex vigorously at high speed for 20 sec (to vortex correctly, watch to insure that there is a vortex within each tube; results should look like milk shake). Chill on ice bath for 5-15 minutes.

9. Place tubes in same orientation each time to localize pellet. Centrifuge for 2 minutes at 13000-16000x g. Place in ice bath for 5 minutes and centrifuge again for another 3 minutes. (In the meantime, prep for step 10; if large experiment, do samples in batches, with replacement on ice between runs. The precipitated protein will form a tight white pellet). Let sit in incubator for 1 min then place back in ice bath for ~ 2-3 minutes.

10. Label new set of microfuge tubes and add 600 μL of isopropanol at room temperature. Carefully remove 600 μL of the supernatant containing the DNA and transfer to the new tubes (careful not to disturb the protein pellet).

11. Gently mix the solution by inversion for about 14 times or until white thread-like strands of DNA form. Stop at this point. Place samples in the fridge overnight without centrifuging.

Day 2 – Process II

12. Next day, centrifuge samples for 2 minutes, place on ice bath for 5 minutes, centrifuge for 2 more minutes. The DNA will be visible as a small white pellet.

13. Carefully decant the supernatant.

14. Add 600 μL of room temperature 70 % ethanol and gently invert the tube several times to wash the DNA. Centrifuge for 2 minutes at room temperature. (To prepare EtOH, add 15 mL of DD H20 to 35 mL absolute ethanol). Place back in ice bath, 5 minutes; then centrifuge for 2 minutes.

15. Carefully aspirate ethanol using the 100 μL pipetor. The DNA pellet is very loose and care must be taken to avoid aspirating it.

16. Invert tubes on clean absorbent paper and air-dry the pellets for at least 10-15 minutes.

17. Add 250 μL Rehydration Solution and rehydrate the DNA at room temperature (on the bench) overnight.

APPENDIX C: DOSIMETRY

C.1 Radiochromic Film Dosimetry

C.1.1 Film Calibration at 4 MV

The method for calibrating film at 4 MV is described in Brown *et al.* (2012a). Briefly, a total of twelve 5 x 5 cm^2 pieces of EBT film were irradiated individually on two separate occasions with doses between 0.5−7 Gy to create a calibration curve (NOD vs. dose) that was fitted with a logarithmic function of the form recommended by the manufacturer:

$$NOD = -ln\left(\frac{a + b * D}{a + D}\right), \tag{C.1}$$

where D is dose and a and b are constants, and fitted to the data using a nonlinear least squares algorithm in Gnuplot v4.4. Each piece of film was positioned at the center axis at 90 SSD with a 30 x 30 cm^2 field (defined at isocenter) and under a 10 cm thick slab of Solid Water® phantom. The MUs to be delivered to the film were determined using standard monitor unit calculations based on dose output calibrated at 100 cm SSD following TG-51 protocol (Almond *et al.* 1999), as described in Section 3.2.1.3. X-ray dose output constancy from the linear accelerator was checked by professional medical physicists in accordance with TG-40 protocol (Kutcher *et al.* 1994). Film readout and analysis will be discussed in Section C.1.3.

C.1.2 Film Calibration for Monochromatic X-Rays

The method for calibrating film at 25, 30, and 35 keV are described in Brown *et al.* (2012a). For each calibration, 5 x 5 cm^2 pieces of film were cut from a single sheet with a small line drawn on each piece to indicate the orientation of the original sheet. This was done to ensure consistent film orientation on the flatbed scanner, as discussed in Section C.1.3. Two pieces of film were used to provide a background measurement of the optical density for each sheet of film.

Ion chamber measurements were used to determine the dose delivered by the monochromatic beams at different depths in the PMMA phantom. To verify these ion chamber measurements, dose-response measurements were performed by irradiating eight pieces of film within the phantom at depths from 0.58 to 8.5 cm. The PMMA phantom was composed of 0.63 and 1.27 cm thick 10 x 10 cm^2 slabs, and the film pieces were sandwiched between theses slabs for irradiation. Each film piece was centered laterally and taped to an adjacent slab. The slabs were then aligned and taped together to minimize the effect of air gaps in the phantom. EBT film pieces were irradiated at each depth individually, while each set of EBT2 films were irradiated at all depths simultaneously. The front surface of each piece of film was used as the effective point of measurement (film thickness < 0.3 mm), and the depth values were determined accordingly. Small depth corrections (< 0.2 mm) to the EBT2 film depths were made to account for the presence of film pieces at shallower depths in the phantom by calculating the increased beam attenuation. These depth corrections are included in the range of depths given above. The duration of each irradiation was chosen so that a dose of approximately 2 Gy was delivered at a depth of 0.6 cm. The time and average ring current for each film irradiation were used to renormalize the measured ion chamber dose output. For each energy, Equation C.1 was fitted to the data. The reproducibility of this calibration method was tested by repeating the calibrations of EBT and EBT2 films. The dose-response curve was measured three times at 35 keV for EBT film and twice at 25 and 35 keV for EBT2 film. A new set of ion chamber measurements was made for each calibration. Film readout and analysis will be discussed in the next section.

C.1.3 Film Readout and Analysis

Film analyses were done in the manner described in Brown *et al.* (2012a). All irradiated films were digitized using an Epson 1680 Professional flatbed scanner (Seiko Epson

Corporation, Nagano, Japan) at least 24 hours after irradiation as recommended in the TG-55 protocol (Niroomand-Rad *et al.* 1998). To avoid systematic errors arising from film handling, each piece of film was cleaned with a 70% ethanol solution prior to scanning to remove any finger prints, remaining felt pen marks used to divide up the original sheet of film (other than the orientation line), and tape or Super Flab® residue. The film, centered on the scanner bed using a cardboard template to ensure film placement reproducibility, was aligned so that the long axis of the scanner was parallel to the long axis of the film (see Figure C.1). Due to the asymmetric structure of EBT2 film, care was taken to ensure that the film was always scanned with the 50 μm thick polyester layer facing the glass window on the bed of the scanner. To avoid any large change in light intensity as the scanner lamp warmed up, five scans were initially performed in the absence of film to ensure a stable light output (Oves 2008). The film was scanned in transmission mode using the software Image Acquisition (International Specialty Products, Wayne, NJ) and was stored as a 300 dpi, 16-bit, TIFF image.

The TIFF images were analyzed using the software ImageJ v1.42p (National Institutes of Health, Bethesda, MD). For the monochromatic irradiations, the exposed region of each piece of

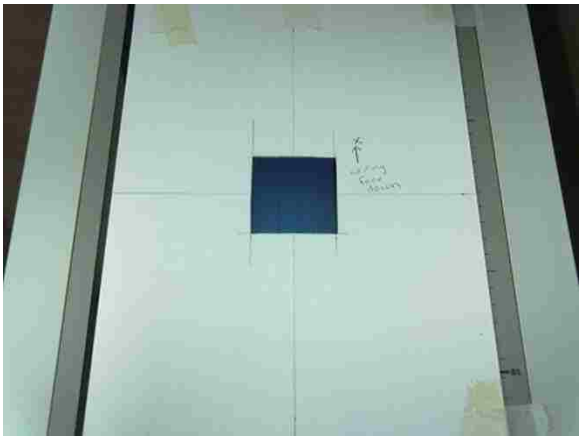

Figure C.1: Epson 1680 Professional flatbed scanner. The cardboard template was used to ensure film placement reproducibility.

film consisted of a 3.0 x 2.5 cm^2 area centered on the film. For the 4 MV irradiations, the entire area of the film was uniformly irradiated and, therefore, a larger ROI (approximately 1.0 x 1.0 cm^2) was selected. The mean pixel value for the red channel was obtained for a region of interest (ROI) measuring 0.5 x 0.5 cm^2 centered on the film image. The center of the film corresponded to the effective point of measurement for the ion chamber. The red channel pixel values were converted into optical density using a logarithmic calibration curve obtained from a NIST calibrated TIFFEN Transmission Photographic Step Tablet #2 (see Figure C.2; The Tiffen Company, Rochester, NY). For each film, the NOD was calculated by taking the difference between the optical density of the exposed film and the average optical density determined from the two unexposed pieces of film. The unexposed pieces of film were analyzed in the same way as exposed films.

Figure C.2: NIST calibrated TIFFEN Transmission Photographic Step Tablet #2 (The Tiffen Company, Rochester, NY).

C.1.4 Film Calibration Curves

The results of each calibration curve were consistent with one another at the same energy. This indicates an ability of achieving a high level of consistency for each calibration setup. Figure C.3(a) shows the NOD versus dose plots for EBT film calibrated at 35 keV and 4 MV. Figure C.3(b) shows the NOD versus dose plots for EBT2 film calibrated at 25, 30, and 35 keV and 4 MV. The uncertainty in the dose consists of two components: (1) beam output variations independent of the storage ring current, and (2) the systematic error associated with the TG-61 calibration factors. The uncertainty in the measured dose was determined to be within ±5%.

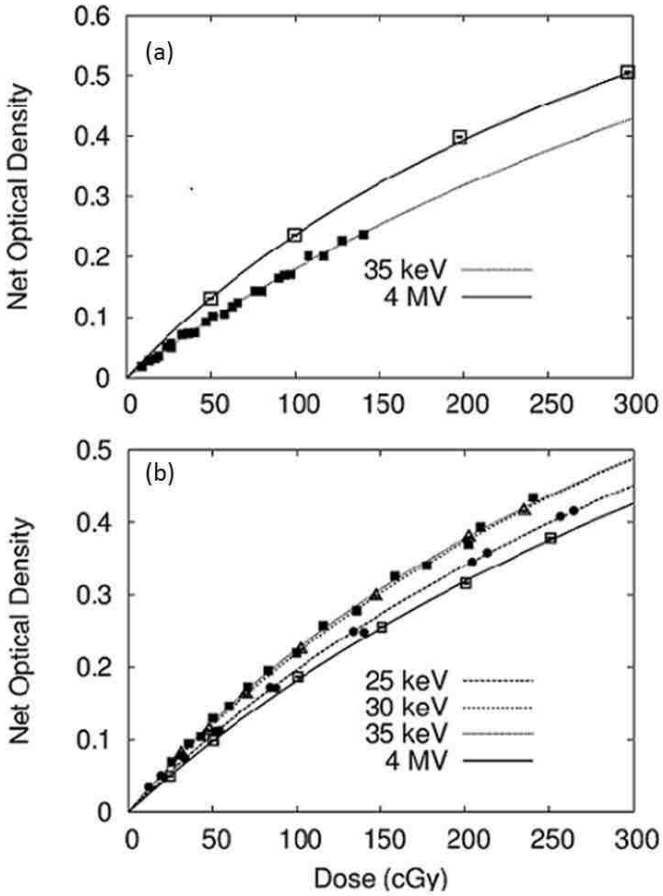

Figure C.3: Calibration curves for EBT and EBT2 films. (a) NOD versus dose for EBT film. The film was calibrated at 35 keV (filled squares) and 4 MV (hollow squares); (b) NOD versus dose for EBT2 film. The film was calibrated at 25 keV (circles), 30 keV (triangles), 35 keV (filled squares), and 4 MV (hollow squares). All sets of data were fitted with the function shown in Equation (C.1) (Brown *et al.* 2012a).

C.2 Validation of Ion Chamber Dosimetry

To validate the use of TG-61 ion chamber dosimetry to estimate the dose rate for cell irradiations, dose to water in a PMMA phantom was measured using (1) an ion chamber where ionization was converted to dose using TG-61 protocol and (2) incident beam fluence ($e^{-}*cm^{-2}$), which was used in MCNP5 Monte Carlo simulations of the irradiation geometry that provided

the dose deposition per photon fluence as a function of depth in the phantom. Refer to Brown *et al.* (2012b) for details.

Briefly, a cylindrical, air-equivalent ion chamber was used to measure the ionization created in a 10 x 10 x 10 cm^3 PMMA phantom for depths of 0.58 to 7.7 cm and converted to dose using TG-61, as discussed in Section 3.2.2.7. The beam fluence was determined using a NaI(Tl) scintillation detector (Alpha Spectra, Grand Junction, CO) to make x-ray scattering measurements of the beam from a thin polyethylene target at angles ranging from 30-60^o at 15^o increments (see Figure C.4). The calculated fluence was used to normalize a MCNP5-calculated depth-dose profile for a PMMA phantom, which was compared with the ion chamber measured dose.

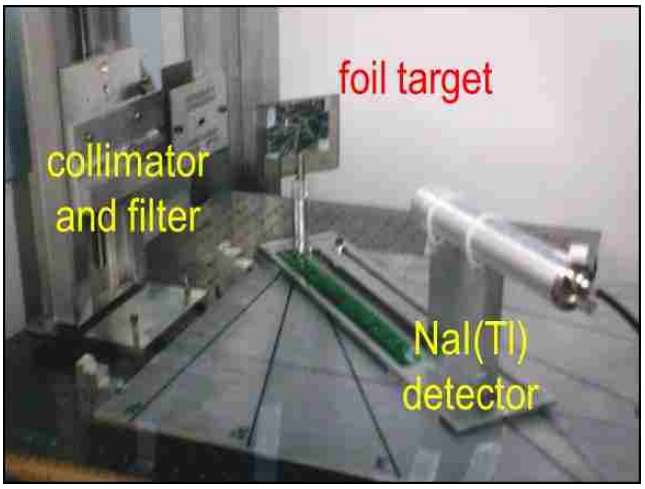

Figure C.4: Geometry of Compton scattering measurements for beam fluence calculations.

Figure C.5 shows plots of dose to water versus PMMA depth at 35 keV and 25 keV. Dose values per 100 mA from ion chamber measurements were compared with the fluence normalized-MCNP5 dose calculations (Brown *et al.* 2012b). The plots show good agreement with the intercomparison within approximately 7% and 3% at 25 and 35 keV, respectively, validating the use of TG-61 protocol to determine cell dose.

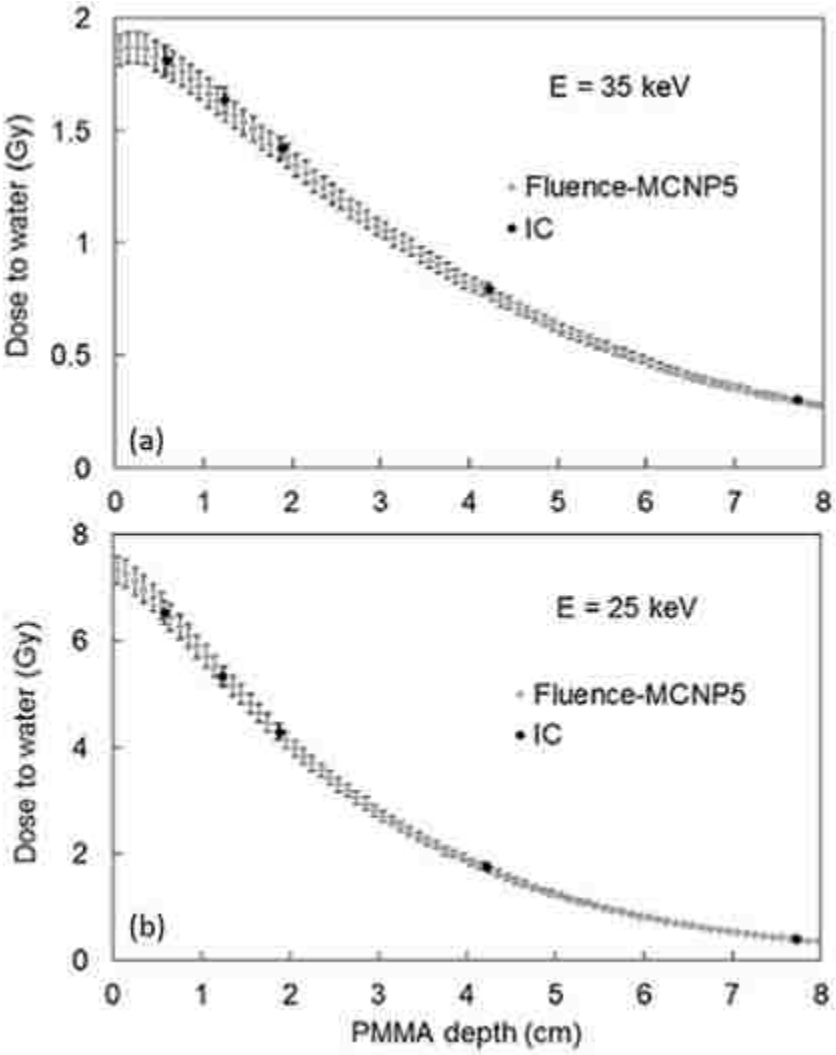

Figure C.5: Dose to water versus PMMA depth. Irradiation energies were (a) 35 keV and (b) 25 keV. Ion chamber measurements are compared with the product of a MCNP5 calculation and measured beam fluence (Brown *et al.* 2012b).

VITA

Diane Alvarez was born and raised in Miami, Florida. She attended high school in the School for Advanced Studies and graduated eighth in her class in 2002, earning her the Florida Bright Futures Scholarship to attend college. The following August, she entered Florida International University and received a Bachelor of Science degree in physics in 2007. Also that year, she was inducted into the Phi Beta Kappa Honor Society and was the recipient of the Arts & Sciences Outstanding Academic Achievement Award. In 2009, she enrolled in the Graduate School at Louisiana State University, receiving numerous scholarships, including the prestigious NSF Graduate Research Fellowship Program award in 2011. She is a candidate for the master's degree in medical physics.